INFORMATION TO USERS

This manuscript has been reproduced from the microfilm master. UMI films the text directly from the original or copy submitted. Thus, some thesis and dissertation copies are in typewriter face, while others may be from any type of computer printer.

The quality of this reproduction is dependent upon the quality of the copy submitted. Broken or indistinct print, colored or poor quality illustrations and photographs, print bleedthrough, substandard margins, and improper alignment can adversely affect reproduction.

In the unlikely event that the author did not send UMI a complete manuscript and there are missing pages, these will be noted. Also, if unauthorized copyright material had to be removed, a note will indicate the deletion.

Oversize materials (e.g., maps, drawings, charts) are reproduced by sectioning the original, beginning at the upper left-hand corner and continuing from left to right in equal sections with small overlaps.

Photographs included in the original manuscript have been reproduced xerographically in this copy. Higher quality 6" x 9" black and white photographic prints are available for any photographs or illustrations appearing in this copy for an additional charge. Contact UMI directly to order.

ProQuest Information and Learning
300 North Zeeb Road, Ann Arbor, MI 48106-1346 USA
800-521-0600

UMI®

IN VIVO ELECTRICAL STIMULATION OF MOTOR NERVES

By

ROBERT BRUCE SZLAVIK, B.ENG. (SUMMA CUM LAUDE), M.ENG.

A Thesis

Submitted to the School of Graduate Studies

in Partial Fulfillment of the Requirements

for the Degree

Doctor of Philosophy

McMaster University

IN VIVO ELECTRICAL STIMULATION OF MOTOR NERVES

DOCTOR OF PHILOSOPHY (1999)
(Electrical and Computer Engineering)

McMASTER UNIVERSITY
Hamilton, Ontario

TITLE: *In Vivo* Electrical Stimulation of Motor Nerves

AUTHOR: Robert Bruce Szlavik, B.Eng., M.Eng. (McMaster University)

SUPERVISOR: Dr. H. de Bruin

NUMBER OF PAGES: 160, xix

ABSTRACT

Stimulus waveform parameters and stimulation protocols are fundamental to the use of electrical stimulation in medical applications. This thesis presents new simulation and experimental procedures that for the first time can quantify the effects on nerve fiber recruitment patterns of variable stimulus waveform parameters, such as pulse width and changes in the stimulation protocol with respect to electrode orientation.

The study of the effect of variable electrical stimulus waveform parameters and stimulation protocols is important from the perspective of therapeutic and diagnostic medicine. Variations in the stimulus waveform such as stimulus pulse width have been shown to offer some promise in allowing for selective recruitment of nerve fibers and motor units based on nerve fiber diameter. The degree of selectivity achievable has not however been quantified under any stimulus electrode protocol. Standardization of electrodiagnostic techniques such as motor unit number estimation would also benefit from a quantified study of nerve fiber recruitment patterns under different stimulus pulse width conditions. Changes in the stimulus electrode orientation result in marked changes in the muscle response during conduction velocity tests. This phenomenon has not been investigated in any systematic fashion. In order to quantitatively study these effects, both theoretically and experimentally, a number of tools and techniques had to first be selected or developed that include: (i) a sufficiently realistic model of the myelinated nerve fiber and nerve trunk that, for the first time in electrical nerve excitation studies, incorporates information associated with anatomically consistent fiber diameter distributions; (ii) a more realistic model of the tissue surrounding this nerve trunk that includes electrical anisotropy; (iii) a field simulation technique used to determine the potential fields at the nerve fiber surfaces (with different diameters and electrode distances) resulting from stimulus pulses with different pulse widths; (iv) two novel sets of experiments, the first of which is used to stimulate a nerve trunk in vivo and from the resulting electrical response, determine the diameters of the nerve fibers that have "fired" under conditions of variable stimulus pulse width, the second of which is used to study the effect of electrode orientation on the stimulus response. The techniques outlined above facilitate a quantitative comparison between experimental and simulation results for the stimulus current pulse width studies as opposed to purely qualitative comparisons that have been reported in the literature. A novel instrument design prototype is presented based on the electrode orientation experiment, that can be used to standardize stimulus electrode orientation for multiple EMG (Electromyography) tests performed on a single subject at different times.

This Thesis is Dedicated to my Parents

Mary and Paul Szlavik

Acknowledgments

I would like to thank my supervisor, Dr. H. de Bruin, for his encouragement and support in all areas of my Ph.D. studies at McMaster University. I would also like to thank my parents Mary and Paul Szlavik, without whose support this work would not have been possible.

The other members of my supervisory committee were instrumental in guiding the development of this thesis and I would like to thank each of them specifically Dr. S.H. Chisholm, Dr. D.R. Conn and Dr. L.D. Pengelly. I greatly appreciated the assistance of Mr. E. Padgett of the Hamilton Health Sciences Corporation (HHSC) whose practical knowledge of electronics is second to none. Mrs. Marie Fennell, also of the HHSC, deserves my thanks for her assistance and friendship. In addition, I would like to thank several past and present members of the staff of the HHSC, McMaster Medical Center Campus, for their friendship specifically Mr. J. Ashton, Mr. J. Gossifidou, Mr. H. Keown, Mr. J. Kettle, Mr. M. Leng, Mr. G. Shine and Mr. A. Suchecki. Additionally, I would like to acknowledge and thank the volunteers who participated in my experimental studies.

In conclusion, I would like to acknowledge the support of the Natural Sciences and Engineering Research Council of Canada (NSERC) and the Ontario Graduate Scholarship Program.

Table of Contents

List of Figures

Chapter 1

Chapter 2

Chapter 3

Chapter 4

Chapter 5

Appendix A

Appendix B

Appendix C

List of Symbols

a	Fiber Radius (m)
a_{LS}	Least Squares Coefficient Vector
b	Relative Membrane Permeability of Sodium Ions to Potassium Ions
C_A	Capacitive Admittance Matrix (F)
C_m	Membrane Capacitance (F)
C_{MP}	Capacitance of a Section of Muscle Fiber Membrane Used in the Parallel Equivalent Circuit Model (F)
C_{MT}	Capacitance of the Cell Membrane in Transverse Muscle Fiber Equivalent Circuit Model (F)
c	Relative Membrane Permeability of Chloride Ions to Potassium Ions or Angle Associated with Idealized Hexagonal Geometry of Muscle Fiber Cross Section as per Figure 2.10 (°)
c_m	Membrane Capacitance Per Unit Area (F/m^2)
D	Fiber Diameter (m)
d	Half Width of the Extracellular Tissue Medium (m) or Distance Between Finite Difference Mesh Nodes (m)
E	Electric Field (V/m)
E_m	Transmembrane Equilibrium Potential (V)
F	Faraday's Constant (C/mol)
F_e	Force Exerted (N)
G_A	Conductive Admittance Matrix (S)
G_c	Cytoplasm Conductance $1/R_c$ (S)
G_m	Membrane Conductance $1/R_m$ (S)
G_{MP}	Conductance of a Segment of Muscle Fiber Membrane Used in the Parallel Equivalent Circuit Model (S)
G_{MT}	Conductance of the Cell Membrane in Transverse Muscle Fiber Equivalent Circuit Model (S)
g_m	Membrane Conductance Per Unit Area (S/m^2)
h	Transient Simulation Time Step (s)
$h_i(t)$	Conceptual Motor Unit Action Potential System Impulse Response
I_i	Intracellular Current Source (A)
I_c	Conductivity Measurement Injected Current (A)
I_{ext}	Magnitude of Stimulus Current (A)

I_s	Finite Difference Current Source Density (A/m^3)
J	Current Density (A/m^2)
K	Spacing Between Successive Nodes of Ranvier (m)
k_v	Ratio of Nerve Fiber Conduction Velocity to Diameter (s^{-1})
L	Stimulus Electrode Length (m) or Center to Center Length Between Adjacent Nodes of Ranvier (m)
L_c	Conductivity Measurement Material Length (m)
L_m	Length of Muscle Fiber in the Conductivity Simulation Used in the Parallel Equivalent Circuit Model (m)
l	Length of Node of Ranvier (m)
l_M	Estimated Straight Line Distance Between the Stimulus and the Recording Electrodes (m)
$M(t)$	Functional Representation of M-Wave (V)
m	Four Electrode Technique Interelectrode Distance (m)
$m_i(t)$	Motor Unit Action Potential (V)
n	Node of Ranvier Index
$P_e(x)$	Cumulative Distribution Function Associated with the Efferent Fiber Diameter Distribution
P_{FP}	Membrane Surface Area of a Discretized Segment of Skeletal Muscle Fiber Used in the Parallel Equivalent Circuit (m^2)
p	Ratio of the Muscle Fiber Interior Volume to the Total Volume
$p_e(x)$	Probability Density Function Associated with the Efferent Fiber Diameter Distribution
q	Descritization Length Used in the Muscle Fiber Parallel Equivalent Circuit Model (m)
R	Gas Constant (J/(K mol))
R_c	Cytoplasm Resistance (Ω)
R_{CP}	Resistance of Intracellular Material to Current Flow in the Direction Parallel to the Muscle Fiber Long Axis Used in the Parallel Equivalent Circuit Model (Ω)
R_{EP}	Resistance of the Extracellular Material to Current Flow in the Direction Parallel to the Muscle Fiber Long Axis Used in the Parallel Equivalent Circuit Model (Ω)
R_{ET}	Resistance of Extracellular Tissue medium in Transverse Muscle Fiber Equivalent Circuit Model (Ω)
R_m	Membrane Resistance (Ω)
R_{MP}	Resistance of a Section of Muscle Fiber Membrane to Current Flow Used in the Parallel Equivalent Circuit Model (Ω)
R_{MT}	Resistance of the Cell Membrane in Transverse Muscle Fiber Equivalent Circuit Model (Ω)
r	Radial Distance from Electrode in the Four Electrode Technique (m)

S_c	Conductivity Measurement Material Cross Sectional Area (m^2)
S_{EP}	Surface Area of Extracellular Material Used in the Parallel Equivalent Circuit Model (m^2)
S_{FP}	Interior Cross-Section Area of the Muscle Fiber Used in the Parallel Equivalent Circuit Model (m^2)
S_T	Total Cross-Section Area of the Muscle Fiber (m^2)
s	Number of Motor Units Contributing to the M-Wave
T	Absolute Temperature (K)
t	Time (s)
t_c	Conductivity Measurement Tissue Specimen Thickness (m)
t_d	Motor Unit Latency (s)
t_i	Time Delay Associated with Each Individual Impulse in the Motor Unit Action Potential Train (s)
u	Sequence of Uniformly Distributed Random Variables or Transient Simulation Time Step Index
V	Vector of Nodal Potentials or Potential (V)
V_a	Anisotropic Potential (V)
V_c	Conductivity Measurement Potential (V)
V_d	Relative Potential Difference as Per Equation (3.8)
V_e	Extracellular Potential (V)
V_i	Isotropic Potential (V) or Intracellular Potential (V)
V_m	Transmembrane Potential (V)
V_n	Finite Difference Computational Cell Potentials as per Figure 3.2 (V)
V_r	Resting Membrane Potential (V)
x	Length of One Side of the Assumed Hexagonal Muscle Fiber Geometry (m) or Sequence of Randomly Generated Efferent Fiber Diameters
x_o	Monopolar Electrode x Coordinate (m)
Y	Nodal Admittance Matrix (S)
y	Perpendicular Radius of the Assumed Hexagonal Muscle Fiber Geometry (m) or Longitudinal Distance (Gielen's Formula) (m)
y_M	Vector Consisting of Compound M-Wave Sampled Data Points (V)
y_o	Monopolar Electrode y Coordinate (m)
Z	Impedance (Ω)

α	Efferent Nerve Fiber Distribution Grouping
$\delta(t)$	Dirac Delta Function
$\delta_d(t)$	Functional Representation of Post Propagation Delay Motor Nerve Action Potential
$\delta_i(t)$	Functional Representation of Motor Nerve Action Potential
γ_f	Efferent Nerve Fiber Distribution Grouping
γ_s	Efferent Nerve Fiber Distribution Grouping

Ψ	Relative Frequency of Different Types of Efferent Fibers for Different Fiber Type Groupings or Induced Transmembrane Potential per Unit of Injected Current (V/A)
λ	Constant as defined in (2.23) (1/m)
μ	Mean Value of Fiber Diameter Distribution Groupings (m)
Φ	Scaled and Time Shifted Motor Unit Action Potential Data Matrix (V)
φ	Scalar Potential (V) or Conductivity Measurement Phase Shift (°)
ρ	Resistivity (Ωm)
ρ_c	Cytoplasm Resistivity (Ωm) (Note for Skeletal Muscle: $\rho_c = \rho_i$)
ρ_E	Resistivity of Extracellular Medium (Ωm) (Note for Skeletal Muscle: $\rho_E = 1/\sigma_e$)
ρ_l	Finite Difference Longitudinal Tissue Resistivity (Ωm)
ρ_t	Finite Difference Transverse Tissue Resistivity (Ωm)
σ	Standard Deviation of Fiber Diameter Distribution Groupings (m) or Conductivity (S/m)
σ_c	Conductivity (S/m) or Cytoplasm Conductivity (S/m) (Note for Skeletal Muscle: $\sigma_c = \sigma_i$)
σ_e	Conductivity of Extracellular Medium (S/m) (Note for Skeletal Muscle: $\sigma_e = 1/\rho_E$)
σ_{eff}	Effective Conductivity (S/m)
σ_H	Tissue Conductivity - High Conductivity Direction (S/m)
σ_i	Conductivity of Intracellular Medium (S/m) (Note for Skeletal Muscle: $\sigma_i = \sigma_c$)
σ_L	Tissue Conductivity Low Conductivity Direction (S/m)
σ_{LM}	Muscle Fiber Longitudinal Effective Conductivity (S/m)
σ_l	Finite Difference Longitudinal Tissue Conductivity (S/m)
σ_{TM}	Muscle Fiber Transverse Effective Conductivity (S/m)
σ_t	Finite Difference Transverse Tissue Conductivity (S/m)
σ_{eff}	Effective Conductivity (S/m)

Glossary of Terms

Electromyography (EMG) - The study of the electrical activity of muscle.

Functional Electrical Stimulation (FES) - Electrical stimulation of skeletal muscle tissue applied to produce a desired response.

MATLAB - Mathworks Corporation's mathematical software package.

PSPICE - Microsim Corporation's implementation of SPICE.

SPICE - Simulation Program with Integrated Circuit Emphasis. General purpose circuit simulator software package.

Introduction

Discussion of the Problem

Electromyography (EMG) is a routinely used clinical technique for the diagnosis of muscular, neurological or neuromuscular disorders. The basic principle behind EMG is the recording of electrical potentials generated by nerves and muscles. These electrical potentials can be produced by natural physiological recruitment of the muscles by the test subject. They can also be produced by electrical stimulation of the motor nerve where the signal propagates down the motor nerve to the target muscle group. Electrical stimulation in this fashion is an integral component of nerve conduction velocity studies as well as motor unit estimation studies [1].

Although electrical stimulation of nerves has been used for hundreds of years, it was not until this century that the mechanisms of nervous conduction of the electrical signal were understood. The pioneering work by Hodgkin and Huxley lead to an enormous body of research on the electrical properties of excitable cells. Much of this experimental work has focused on the study of extremely large unmyelinated neurons such as the giant squid axon.

Of more practical importance to clinical electromyography is the study of the excitability of nerve fibers in vivo under different stimulus current conditions such as stimulus pulse width and stimulus electrode orientation relative to the nerve trunk. It has been suggested that varying the stimulus current pulse width will afford a degree of selectivity in terms of the motor nerve fiber diameters that are recruited, and consequently the recruited motor unit size [2]. The ability to selectively recruit motor units of different size is especially desirable from the perspective of Functional Electrical Stimulation. A quantitative study of stimulus pulse width effects is also desirable from the perspective of establishing consistent protocols during clinical EMG tests. It is well known that stimulus electrode orientation relative to the direction of the nerve trunk influences the electrical response from the muscle. This fact suggests that optimizing the ability to orient stimulus electrodes consistently relative to the nerve trunk of a subject during different EMG tests would be highly desirable for the purpose of standardizing or optimizing the test results. In spite of this observation, stimulus electrode orientation effects have not been studied in any systematic fashion.

Theoretical nerve excitation studies to date have been limited by their focus on nerve fibers outside of a realistic tissue environment. Another drawback of these studies is that most, if not all, have been carried out on a single fiber. While these studies are useful in establishing trends associated with stimulus current requirements for a given diameter fiber to reach threshold, they are not sufficient to quantitatively predict the recruitment patterns of a nerve fiber population with a distinct fiber diameter distribution. Single fiber stimulus duration simulations are also difficult, if not impossible, to compare directly with in vivo experimental results.

Review of Previous Work

The study of electrical nerve stimulation has existed for hundreds of years and was pioneered in Italy by Galvani as reviewed in Rattay [3]. A thorough and empirically verifiable theory of nervous conduction was developed in the 1950's by Hodgkin and Huxley who were awarded the Nobel Prize for their work [4-8]. Hodgkin and Huxley's theory forms the basis of the electrical equivalent circuit models of nerve fibers that, in one form or another, are widely used in nerve fiber excitability simulations.

The electrical properties of biological tissue have also been investigated for many years. Reported measurements of tissue conductivity go back as far as the turn of the century [9]. Since that time there has been a great volume of literature dedicated to the subject. Continuing interest in this area has been fueled by the large variety of applications of electrical impedance measurement in medicine. In the sixties and seventies there was a great deal of effort made towards developing electrical impedance measurement techniques to monitor fluid accumulation in the lungs, ventilation characteristics and cardiac output [10-15]. More recently there have been efforts to develop an instrument that uses impedance measurement data from a subject to construct a two dimensional image similar to a computer aided tomograph (CAT) scan but without the risk of exposure to x-rays [16-21].

In addition to the purely experimental work focused on measuring frequency dependent tissue conductivity [22-24], some investigators have attempted to develop a theoretical foundation for these measurements based on the geometric structure of the tissue and the electrical properties of the materials that compose them [25-27].

A unified theoretical study of electrophysiology and the electrical properties of tissue has not been pursued to any great extent [28]. There have been several studies presented from the sixties to the present that focused on simulating a single nerve fiber in an idealized infinite extracellular medium and studying its response to electrical current stimulus [29-33]. Relatively few publications exist that mention the effect of a stimulus modality on a population of nerve fibers consistent with anatomically observed fiber diameter distributions [34].

There are some references, particularly in the area of Functional Electrical Stimulation, that discuss the effect of variations in stimulus current waveform on nerve fiber recruitment [2,35]. It has been suggested that some recruitment selectivity, in terms of fiber size, could be achieved by varying the stimulus current pulse width, however, a serious gap exists between the theory and the empirical studies that have been reported. Only qualitative comparisons between experimental observations and theoretical predictions can be made with single fiber stimulus strength duration simulations presented thus far.

Scope of this Thesis

The theoretical goal of this thesis is to develop a simulation tool to quantitatively study the effect of variations in stimulus pulse width on the recruitment patterns associated with a population of nerve fibers in a realistic tissue environment with an anatomically consistent fiber size distribution. This simulation approach is novel because it incorporates information about the nerve fiber population and the results can be quantitatively compared with experimental measurements. Development of the simulation tool requires knowledge of both tissue electrical properties as well as electrophysiological models of nerve fibers. In conjunction with the simulation discussed above, an experimental technique was developed for measuring data that could, for the first time, be quantitatively compared with simulation results. This technique is based on a motor unit number estimation algorithm with surface electrode stimulation and can be used to estimate the average recruited nerve fiber diameter observed under conditions of different stimulus pulse widths. The recruitment patterns observed in these experiments can be quantitatively compared with the simulation results. Surface electrode stimulation was used because, to date, it is still one of the most practical stimulation methodologies available [3].

Concepts from the field simulations discussed earlier, along with relevant theoretical considerations are used to explain the variations in muscle response observed with different stimulus electrode orientations relative to the direction of the nerve trunk. An experimental technique is developed to study stimulus electrode orientation effects relative to the direction of the nerve trunk in a systematic fashion. This experiment can be used as the basis of an automated technique for determining the optimal stimulus electrode orientation during clinical EMG tests for the purpose of standardizing such tests done at different times on the same subject. A computer controlled prototype instrument design is presented with this goal in mind.

An experimental and theoretical study of skeletal muscle tissue anisotropy is undertaken to establish the characteristics of the tissue environment. Anisotropic conductivity measurements were carried out on human as well as poultry skeletal muscle tissue. An equivalent circuit model was developed and implemented in PSPICE (Simulation Program with Integrated Circuit Emphasis) based on the geometric properties of skeletal muscle fibers as well as their electrical properties.

Electrical equivalent circuit models of the nerve fibers used in the simulation were based on the characteristics of myelinated nerves. In all cases the nerve fibers were assumed to have linear electrical properties which, under certain restrictions, is a valid assumption. The problem was also assumed to be time invariant in that the firing of one nerve fiber was assumed to be independent and to have no effect on the firing of all other nerve fibers in the population. This assumption is widely believed to be valid [36].

In order to accurately represent a realistic population of nerve fibers in terms of fiber diameter, a population of nerve fibers for efferent peripheral nerves, consistent with reported anatomical observations of fiber diameter, was randomly generated using a numerical technique that will be described later [37].

The simulation consists of two parts. The first part is a two dimensional finite difference electromagnetic field simulation that is used to calculate the potential distribution in the simulated isotropic (subcutaneous tissue and epineurium) and anisotropic (skeletal muscle and nerve fascicle) tissue domain. The second part uses the data from the finite difference simulation to determine the extracellular potentials along simulated nerve fibers lying at specific depths in the simulated tissue domain. This program determines whether the simulated nerve fibers have been depolarized to a sufficient transmembrane potential to be recruited.

In order to study the effects of anisotropic versus isotropic tissue media on nerve fiber recruitment, a series of experiments were carried out in which the orientation of electrodes placed above the median nerve was altered relative to the anatomical direction of the nerve.

Experiments were carried out in order to determine the effect of current pulse width on nerve fiber recruitment the results of which, for the first time, could be directly compared with the simulations. An automated technique developed for motor unit estimation was used for these experiments. The simulation as well as the experimental results demonstrate that there is some selectivity achievable in the recruitment of nerve fiber sizes with variable current pulse widths.

Chapter 1: The Structure and Function of Nerves and Skeletal Muscle Tissue

In this opening chapter, background information is presented on the anatomical structure of peripheral nerves. The theory of nerve fiber excitation is presented with a detailed discussion of the processes that result in nerve fiber excitation. There is a fundamental difference in the way in which nerves or neurons are recruited physiologically and the way they are recruited artificially by way of electrical stimulation: this difference is emphasized. A review of skeletal muscle structure is also undertaken with the goal of explaining how the anatomical characteristics of skeletal muscle tissue give rise to the observed electrical anisotropy.

1.1 The Basic Anatomy of the Nervous System

The fundamental unit of the anatomy of the nervous system is the neuron. A neuron is a single cell with a structure shown below in Figure 1.1 [38].

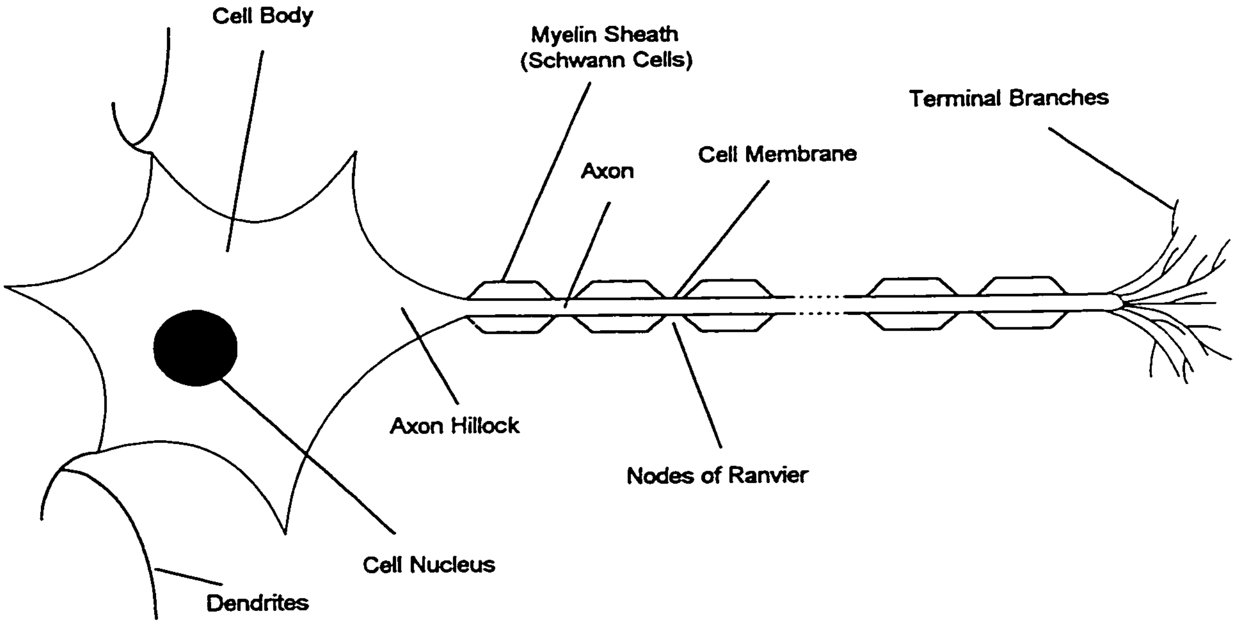

Figure 1.1 An idealized diagram of the peripheral nervous system neuron illustrating the major components that are associated with the cell body as well as the components associated with the axon. The drawing is not to scale and the dashed lines on the axon emphasize that the length of the axon is much greater than the length of the cell body and can extend for several tens of centimeters [38].

The neuron consists most basically of a cell body (soma), dendrites and an axon. The axon terminates in branches that connect or synapse with other neurons or, in the case of a motor unit axon or fiber, with skeletal muscle fibers. Since the neuron is a single cell, its interior can be described most basically as consisting of a fluid material called the axoplasm in which the organelles are suspended. Surrounding the neuron is a cell membrane that consists of a phospholipid bilayer in which are embedded transmembrane proteins. The most important of these proteins, from the standpoint of nervous excitation, are the voltage dependent gates that form an essential component of the process that changes the transmembrane potential of the cell. There are other proteins embedded in the cell membrane such as those of the sodium-potassium pump that perform equally crucial functions for the cell but are not directly related to the excitation process [39].

Surrounding the peripheral axon is a myelin sheath that consists of Schwann Cells. These cells wrap themselves around the axon and provide insulation from the highly conductive extracellular fluid for the electrical signal as it propagates down the length of the axon. The myelin sheath is interrupted at regular intervals by small 2.5 μm wide gaps referred to as the Nodes of Ranvier [33]. These gaps are the only points along the length of the axon that the cell membrane is in contact with the extracellular environment. It is at the Nodes of Ranvier that the propagating electrical signal traveling down the length of the axon is regenerated [40].

Physiological recruitment of a neuron occurs when the terminal branches from other neurons that synapse with the dendrites on the cell body provide sufficient excitatory input such that the cell membrane of the neuron reaches a threshold potential. In effect, the target neuron spatially and temporally integrates the input from up to thousands of other neurons. The spatially and temporally integrated inputs to the target neuron determine whether the target neuron reaches threshold and becomes excited [38,40].

Artificial electrical recruitment of nerves is an entirely different process than physiological recruitment. One primary difference between these two recruitment processes is the anatomical location of recruitment. In the case of external electrical stimulus, the neuron reaches threshold at some point along the axon which is often referred to as the nerve fiber. This is the point of initiation of the electrical signal or action potential. Physiological excitation occurs on the cell body and dendrites of the neuron where the terminal branches of other neurons synapse. The anatomical location of the initiation of the electrical signal or the action potential on the neuron is in the vicinity of the axon hillock [40]. The mechanism of excitation for artificial electrical stimulation does not involve synapses or connections with the neuron but is determined by whether sufficient electrical stimulation has been applied such that the transmembrane potential at some point along the axon is changed from the resting to the threshold value [41].

1.2 Mechanism of Nerve Fiber Excitation

At the Nodes of Ranvier, the membrane of the axon is in contact with the extracellular solution. There are marked concentration differences between membrane permeable ions in the extracellular solution and the ions internal to the cell in the axoplasm. It is these ionic concentration differences that maintain the transmembrane potential or the difference in the potential measured in the axoplasm and in the extracellular fluid at an equilibrium value. This potential E_m can be related to the concentration difference of a single ionic species through the Nernst equation. An extension of the Nernst relationship is the Goldmann equation (1.1) that describes the transmembrane potential in the presence of the three most significant ions for nervous conduction specifically, sodium, potassium and chloride. In general, sodium and potassium ions are most crucial to the nerve excitation process [42].

$$E_m = \frac{RT}{F}\ln\left(\frac{\left[K^+\right]_o + b\left[Na^+\right]_o + c\left[Cl^-\right]_i}{\left[K^+\right]_i + b\left[Na^+\right]_i + c\left[Cl^-\right]_o}\right) \qquad \textbf{(1.1)}$$

The constants b and c represent the relative ionic permeability of sodium and chloride to potassium.

The potential gradient created by the concentration differences in the ions can be viewed as batteries that drive the ionic currents through their respective membrane protein gates. These gates in the membrane can be modeled as lumped parameter conductances for each specific ionic species since the gates are species selective. The conductance of each gate is representative of the membrane permeability to that specific ionic species. At equilibrium resting transmembrane potential, the conductances of these voltage dependent gates are relatively small. It should also be noted that the phospholipid bilayer that forms the membrane of the cell is a dielectric that has charged particles on either side of it which effectively forms a capacitor. All these elements of the cell membrane can be combined into an equivalent circuit model that is representative of the electrical properties of a given length of axon membrane at the equilibrium transmembrane potential. The equivalent circuit model is shown in Figure 1.2 [43].

Since the resting cell membrane potential is different from the equilibrium Nernst potentials for sodium and potassium given their differential concentrations on the inside and the outside of the cell, the question arises as to how the cell maintains these concentration gradients. At the resting membrane potential, sodium ions will have a tendency to flow through the relatively low conductance sodium channels into the cell and potassium will have a tendency to flow from the inside of the cell to the outside. The cell maintains the resting concentrations of sodium and potassium inside by way of the sodium and potassium pump proteins that exist on the cell membranes. These specialized membrane proteins utilize chemical energy obtained from cleaving adenosine triphosphate molecules to move sodium ions against their natural concentration gradient. Utilizing this pumping mechanism, sodium is actively transported from the inside of the cell to the outside where the concentration is higher. In the same way, potassium is transported from the outside to the inside of the cell where it is in higher concentration [39].

Nervous excitation represents a state where the transmembrane potential of the axon varies widely from the resting potential. The ion species specific gates in the membrane of the axon do not maintain a static conductance. The ease with which these gates conduct ions is dependent on the transmembrane potential and time. If the transmembrane potential is increased from its equilibrium value of around -70 mV to approximately -40 mV, the sodium ionic gates will open allowing more positive sodium ions into the cell interior from the exterior where these ions exist in a higher concentration. This process will further increase the transmembrane potential which will open the sodium ion gates even further. A positive feedback process is therefore initiated that results in the transmembrane potential changing from approximately -70 mV to about +30 mV. At this point the neuron is said to have fired or become excited [44].

The sodium gates are time dependent and they will begin to close after a fraction of a millisecond choking off the influx of positive sodium ions. Simultaneously, the potassium gates will open allowing positive potassium ions to move from the cell interior where they are in higher concentration to the exterior of the cell. With the efflux of positive charge, the cell transmembrane potential is returned to the resting equilibrium value [44].

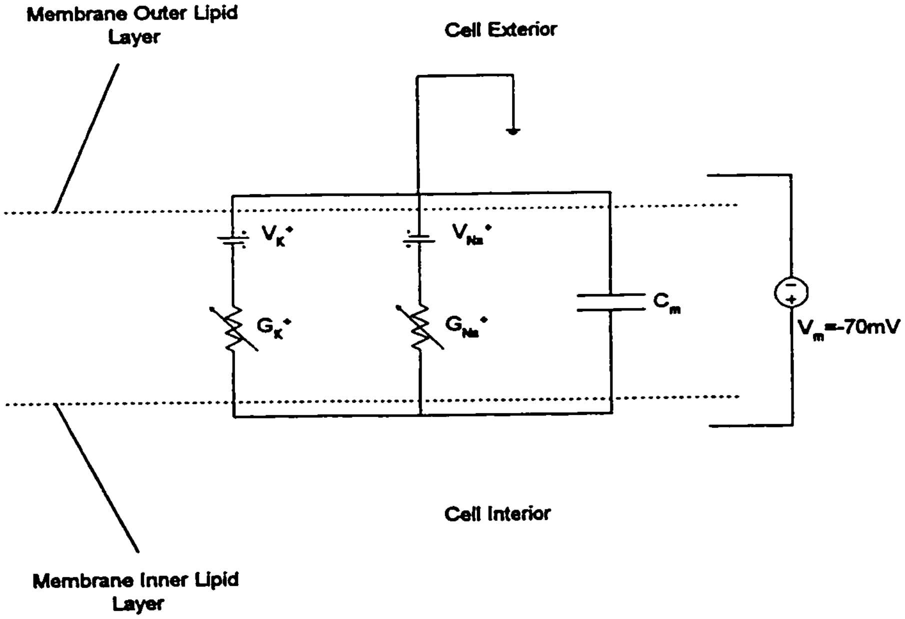

Figure 1.2 Equivalent circuit model of a unit area of nerve cell membrane. The diagram shows the lumped parameter ion specific membrane conductances that are a function of the transmembrane potential V_m and the time t. In the diagram V_K^+ = -85 mV and V_{Na}^+ = 35 mV

Once the action potential is generated in an unmyelinated fiber, the wave of depolarization will move in all directions away from the initiation site. If the initiation site is on the axon, then propagation will occur in both directions. Voltage dependent ionic gates that are a short distance from the initiation site will become depolarized setting up the same positive feedback mechanism and allowing the electrical signal to propagate down the length of the axon or nerve fiber. There is a refractory period for the sodium and potassium voltage dependent ion channels in the membrane. This refractory period limits the frequency at which the neuron can be stimulated since the sodium and potassium channels will not increase their conductance appreciably again for a few milliseconds after the initial action potential is generated.

Propagation of the action potential down the length of a myelinated fiber differs from the unmyelinated case. The myelinated fiber consists of insulating Schwann cells at regular intervals as shown in Figure 1.1. When an action potential is generated at a specific Node of Ranvier, the positive current will flow down the length of the fiber which will result in a depolarization of the membrane. Due to the presence of the insulating Schwann cells, only a relatively small amount of current will leak back through the membrane to the extracellular environment and the region over which the membrane is depolarized is effectively lengthened. At an adjacent Node of Ranvier, the membrane depolarization will be sufficient to generate another action potential. This process is referred to as saltatory conduction and will continue down the length of the axon [42].

1.3 The Anatomy and Function of Skeletal Muscle Tissue

Skeletal muscle tissue is one of several muscle tissue types. There are other types of muscle tissue such as cardiac muscle tissue which in many respects is very similar to skeletal muscle tissue in terms of its striated appearance. Smooth muscle tissue is different in that there is no regular geometric arrangement of muscle fibers in smooth muscle as is found in cardiac or skeletal muscle tissue [44].

During routine clinical EMG studies, the investigator will often attempt to stimulate a motor nerve to elicit a response from the muscle that it innervates. A good example of this type of test is stimulation of the median nerve in the arm that innervates the thenar muscle in the proximal thumb [45]. The time delay or latency between the instant of stimulation and the muscle response can be used as a diagnostic variable that is indicative of the status of the median nerve. An unusually long latency or no response of the thenar muscle can be indicative of some type of nerve pathology [46].

The motor nerve fibers in the median nerve synapse with muscle fibers in the thenar muscle of the hand. The signal conducted down the nerve fibers is electrical in nature and is conducted by the mechanisms discussed earlier. When the electrical signal reaches the end of the neuron branch, a neurotransmitter, acetylcholine, is released from the end of the branch into the synaptic cleft which is the region between the presynaptic neuron membrane and the muscle fiber post synaptic membrane. On the muscle fiber membrane under the branch terminus are receptor proteins that open and allow sodium ions to flow into the cell when a neurotransmitter binds with them. If a sufficient number of these neurotransmitter binding protein gates are activated by the neurotransmitter released from the presynaptic membrane, the muscle fiber is recruited and an electrical action potential propagates down its length facilitated by very similar mechanisms to those discussed earlier for nerve excitation. Under normal circumstances, the synaptic potential at the end plate is always supra-threshold and initiates a muscle fiber action potential. In this way, the electrical impulse that traveled down the nerve is converted to a chemical signal that propagates across the synaptic cleft between the nerve and the muscle fiber membranes. The impulse once again becomes electrical in nature once the muscle fiber reaches the excitation threshold potential.

Muscle fibers are single threadlike cells with a diameter of approximately 100 μm and a length of up to 30 cm that contract when they are recruited by an action potential from a motor nerve fiber. These cells contract to approximately 60% of their resting length [46]. The arrival of the action potential at the muscle fiber initiates a chain of events that result in the contraction of the muscle fiber. As a result of the propagating electrical action potential along the muscle fiber, calcium ions are released from the sarcoplasmic reticulum into the interior of the fiber. The sarcoplasmic reticulum is an organelle or structure that exists in the interior of the muscle fiber. The calcium ions initiate forces of attraction between filaments in the muscle fiber that are composed of actin and myosin. These filaments slide together which constitutes the contractile process. After several milliseconds, the calcium ions are pumped back into the sarcoplasmic reticulum. These ions remain in the sarcoplasmic reticulum until they are released again by another action potential propagating along the length of the muscle fiber.

Muscle fibers do not contract individually. All the muscle fibers that are supplied by a single motor nerve fiber contract as a group [46]. The nerve cell body in the spinal cord, its axon or nerve fiber, the terminal branches of the axon and all the muscle fibers that are innervated by the branches form a single motor unit. The overall structure of the motor unit is conceptually illustrated in Figure 1.3. The number of muscle fibers in a motor unit is dependent upon which muscle the motor unit belongs to. If the muscle is responsible for fine control such as those muscles involved in eye movement, then the number of muscle fibers in a single motor unit could be on the order of 10 fibers. If however the muscle is relatively large, such as the biceps brachii which is located in the arm, then there may be several thousand muscle fibers in a single motor unit such as found in the medial head of the gastrocnemius muscle [46].

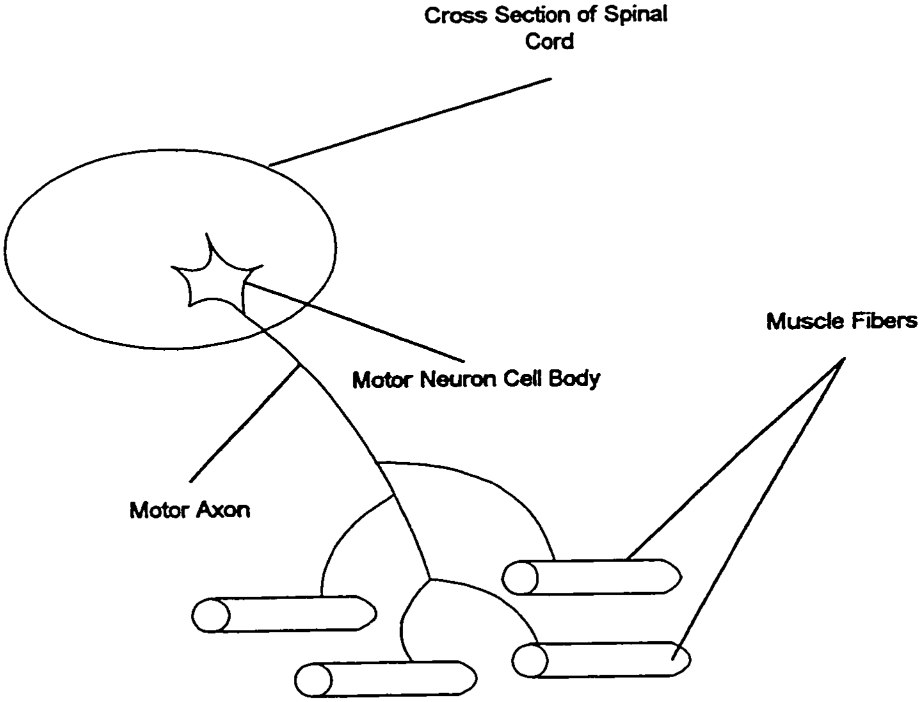

Figure 1.3 Anatomical definition of a motor unit. The motor unit consists of the cell body in the spinal gray matter, the motor axon, and all the muscle fibers that the neuron synapses with.

The nature of muscle fiber contraction is far different from what we observe during motion when we use our muscle groups to move. The raising of an arm or the movement of a hand appears as a fluid smooth motion that would suggest that the contraction of the muscle groups involved in the motion is also fluid in nature. Individual muscle fibers that belong to a single motor unit contract very quickly and almost in unison although the potentials that they generate can be separated by up to a few milliseconds. The time it takes for a muscle fiber to contract and relax completely is anywhere between a few milliseconds to approximately 200 milliseconds [46]. Fluid contraction of muscles, as we observe in practice, is a result of the averaging of these motor units that contract individually very quickly but in an un-synchronized fashion.

The potential developed by a motor unit is approximately 5 to 12 milliseconds in length. Action potentials recorded from individual fibers are on the order of about 1 to 2 milliseconds. A seemingly huge discrepancy exists between the overall motor unit potential duration and the duration of the action potential from a single fiber in the motor unit. The motor unit potential is considerably longer because all the fibers in the unit do not fire exactly in synchrony but can be separated in time by a few milliseconds. Although the electrical impulse from the motor unit can be relatively short, the mechanical contraction from a motor unit has been reported to be as long as a tenth of a second. In general, larger motor units produce larger motor unit potentials however this is not a hard and fast rule because of complicating issues such as the overall distance of the motor unit from the electrode [46].

During artificial electrical stimulation of nerve fibers, the larger nerve fibers are preferentially recruited first. Physiological recruitment in slowly changing contractions differs in that as we call upon a muscle to provide more and more force against a load, smaller motor units are recruited first. As the force requirement is increased, the larger motor units, with more muscle fibers, are subsequently recruited. At high force levels, the mechanism by which the force produced by the muscle is increased is predominantly an increase in the firing rate of motor units as opposed to the recruitment of additional motor units.

1.4 Modeling the Motor Unit Action Potential (MUAP) and the M-Wave

Figure 1.4 has been adapted from Basmajian [46] and illustrates schematically the genesis of a motor unit action potential. The diagram shows the terminals of a single motor neuron and its synapses with the associated muscle fibers in the motor unit. A bipolar electrode is also illustrated from which the superposition of the individual muscle fiber actions potentials is recorded. The relative amplitudes of the muscle fiber action potentials depend on their relative geometric distance from the recording electrodes and the filtering properties of the bipolar electrodes used to record the measurement. As a first order approximation, it is widely accepted that the amplitude of the individual muscle fiber action potential will decrease approximately inversely proportional to the distance between the active fiber and the recording electrode [46]. In addition, the sign of the phases of the action potentials will depend on the direction from which the impulse approaches the bipolar recording electrodes one of which is connected to the positive terminal of a differential amplifier and the other of which is connected to the negative terminal as shown in Figure 1.4.

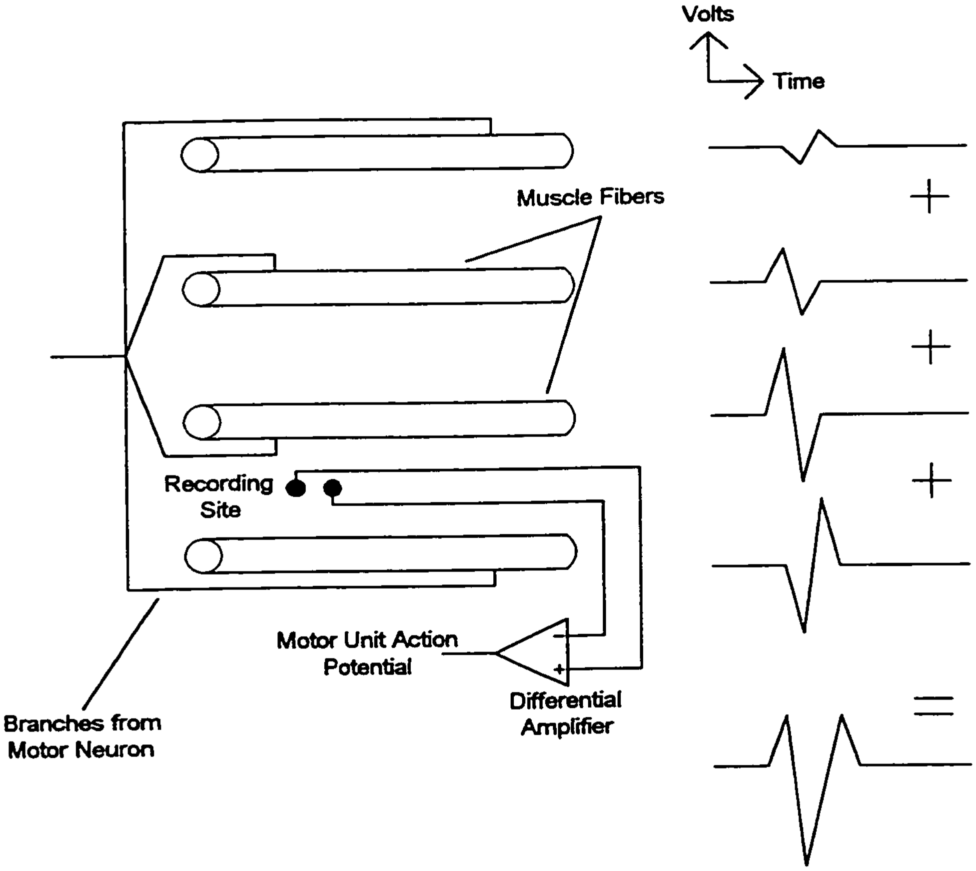

Figure 1.4 Idealized representation of the genesis of the motor unit action potential. The motor unit action potential is the superposition of the individual action potentials generated by the muscle fibers that belong to the motor unit. The diagram also illustrates the motor axon that drives the muscle fibers.

Because the muscle fiber action potentials overlap in time, the resultant motor unit action potential (MUAP) referred to below as m(t) will be the spatial and temporal superposition of the individual muscle fiber action potentials.

A model of the M-Wave that results from electrical stimulus of a nerve can be formulated in a manner that is similar to the formulation of the EMG signal as presented by other investigators [46]. Since the electrical stimulus recruits all axons in synchrony, the first step in developing the model is to define the action potential in terms of a Dirac Delta Function that occurs at time $t = 0$.

After the action potential is generated in a motor nerve fiber, the action potential propagates down the nerve at a speed that is dependent on the nerve fiber diameter. The time delay t_i required for the action potential to propagate a fixed distance to the muscle fibers that constitute the motor unit can be represented in a conceptual block diagram with a delay component of fixed time as shown in Figure 1.5. The shape of the motor unit action potential (MUAP) is specific to each individual motor unit but can be represented generically in the model by a filter with an impulse response $h_i(t)$. The output of the filter is the MUAP.

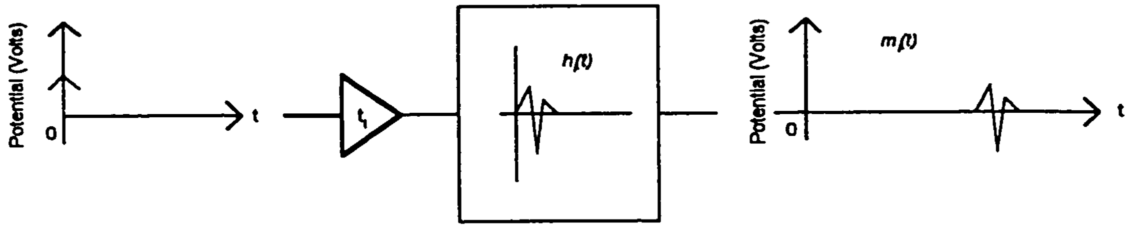

Figure 1.5 Block diagram of motor unit action potential model. The diagram illustrates an ideal delta function generated at $t = 0$ followed by a delay block representing the propagation time to the motor unit muscle fibers. A linear system block with impulse response $h_i(t)$ is excited by the delta function resulting in the motor unit action potential $m_i(t)$ as shown. The time delay associated with $m_i(t)$ is t_i.

The pulse representing the action potential for each individual motor unit can be written as in (1.2)

$$\delta_i(t) = \delta(t) \tag{1.2}$$

The arrival of each action potential at the muscle fibers of the associated motor unit is delayed by a time t_i that is dependent predominantly on the nerve fiber diameter. The expression for the action potential on arrival at the muscle fiber is given by (1.3).

$$\delta_{d_i}(t) = \delta(t - t_i) \tag{1.3}$$

The resultant delayed delta function is convolved with the impulse response of the filter representing the (shape generator) for the *ith* motor unit as shown in (1.4).

$$m_i(t) = h_i(t - t_i) \tag{1.4}$$

A finite summation can be written for the resultant M-Wave hereafter referred to as ***M(t)*** that is the superposition of all the individual motor unit action potentials that resulted from the electrical stimulus.

$$M(t) = \sum_{i=1}^{s} h_i(t - t_i) \tag{1.5}$$

A graphical interpretation of the expression for ***M(t)*** shown in (1.5) is illustrated in Figure 1.6 which has been adapted from Basmajian [46].

In the M-Wave mathematical model, the potential from the total number of individual motor unit action potential trains *s* that are detected at the electrodes is denoted as ***M(t)***. It is important to note that although a theoretical expression can be written for the M-Wave signal that results from the superposition of the individual MUAPs, this signal is not the detected signal in that it is corrupted by noise and modified somewhat by the electrodes as well as the electronics in the instrumentation used to detect the signal. The overall expression for the M-Wave signal prior to corruption by noise and the recording instrumentation is as shown in equation (1.5).

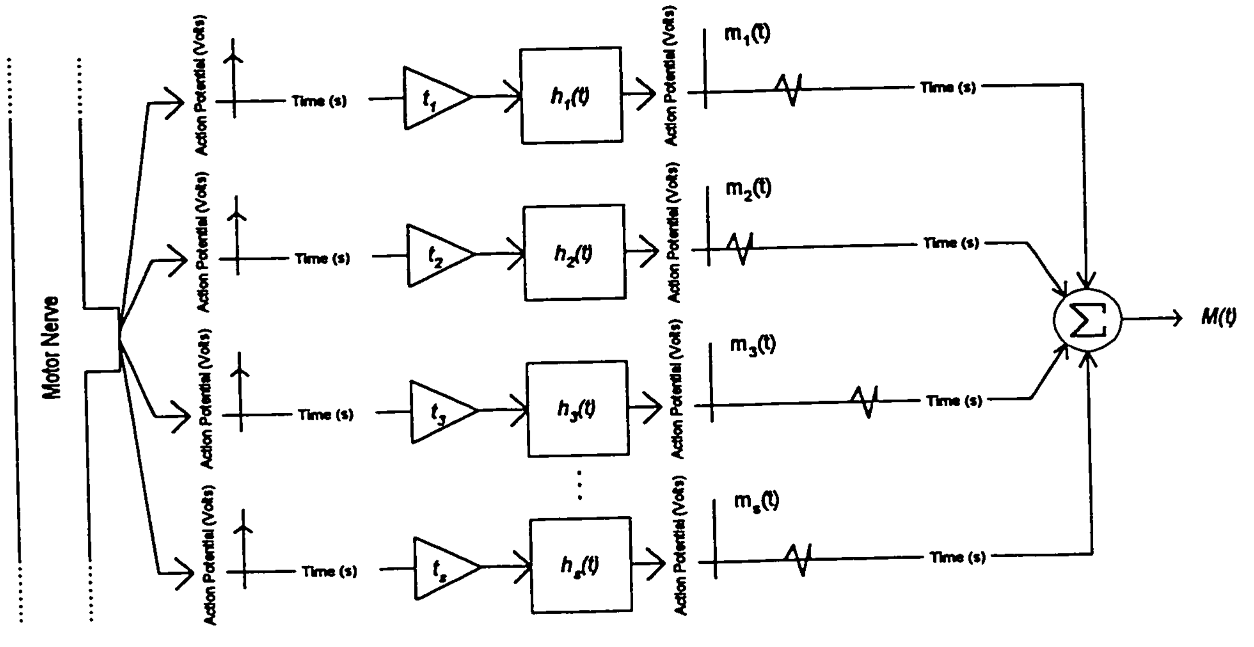

Figure 1.6 Idealized mathematical model of the synthesis of the M-Wave signal. The model shows the idealized delta functions that represents the action potentials generated by the motor nerves, each belonging to one motor unit. Once stimulated with the spike like action potentials, the muscle fibers generate a uniquely shaped pulse that is superposed to form the M-Wave signal.

1.5 The Physical Structure of Skeletal Muscle Tissue and Electrical Anisotropy

Skeletal muscle tissue consists of cells referred to as muscle fibers which, as an approximation, can be viewed as relatively long slender cylinders. The cell membrane consists of a phospholipid material that is a non-conducting dielectric. The conductance per unit area of a muscle cell membrane is relatively small. A typically quoted value for this conductance for frog muscle is 250×10^{-6} S/cm^2 [43]. In contrast, the material inside the cell consists of a relatively high conductance fluid-like substance referred to as the cytoplasm. Suspended in the cytoplasm by protein structures are the various organelles such as the mitochondria that the cell relies on to perform its normal metabolic functions.

It has been acknowledged for many years that skeletal muscle tissue exhibits different electrical properties in different directions [9]. Figure 1.7 is an idealized illustration of a section of skeletal muscle tissue illustrating the individual muscle fibers lying side by side.

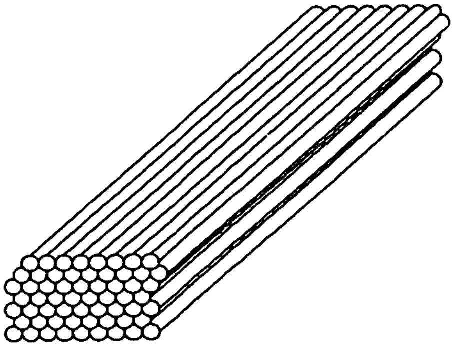

Figure 1.7 Idealized representation of a section of skeletal muscle tissue. The drawing illustrates the geometric arrangement of the muscle fibers that are roughly cylindrical in the real case.

The geometric nature of the arrangement of muscle fibers gives rise to the differences in electrical properties in the directions parallel and transverse to the muscle fibers. It is easier for electrical current to travel in the direction parallel to the long cylindrical axis of the muscle fibers because, in this direction, the current travels through the relatively highly conductive cytoplasm. Current flow in the directions transverse to the long cylindrical axis of the muscle fibers move through a large number of cell membranes that have a relatively low conductance when compared to the cytoplasm.

There is a large body of experimental and theoretical evidence that will be discussed in the following chapters that confirms this intuitive explanation of the directionally dependent electrical properties of skeletal muscle tissue.

Chapter 2: Equivalent Circuit Models of the Nerve Axon and Skeletal Muscle Fibers

In this chapter equivalent circuit models of skeletal muscle tissue and myelinated nerve fibers are discussed. Since both of these cell types can be approximated as extremely long and narrow cylinders, the equivalent circuit models of skeletal muscle tissue in the longitudinal direction and unmyelinated nerve axons are quite similar. Initially the equivalent circuit model of the nerve fiber is presented and its physical basis as it is related to the geometric structure of the axon is discussed. Several variations of the model that have been investigated in the literature are described.

A discussion of the skeletal muscle tissue equivalent circuit model, presented in the literature to simulate the frequency dependent skeletal muscle tissue conductivity, is subsequently presented. A modification of the model based on that introduced by Nicholson [25] and later expanded by Gielen and colleagues [26] is further modified to allow for implementation in SPICE. Gielen's equivalent circuit model used to simulate the transverse frequency dependent electrical conductivity is implemented in SPICE in its original form [27]. Since a different approximation of the basic geometrical shape is used in the literature, the section on skeletal muscle fibers is discussed in the context of hexagonal fiber cross sections as opposed to cylindrical ones which is the common assumption used when developing nerve axon equivalent circuit models. The formulas developed in the section on skeletal muscle fibers assume the hexagonal geometry.

A discussion of the electrical modeling of the nerve axon and the electrical conductivity modeling of skeletal muscle tissue is important because the developments in later chapters will use these two concepts. The skeletal muscle tissue electrical conductivity will figure prominently in the finite difference electromagnetic field simulations used to calculate the potential distribution due to current stimulation. The calculated potential distribution will then be used to determine the extracellular potential along a simulated nerve fiber, which will then be used to calculate the transmembrane potential along the nerve fiber in order to determine whether the fiber has received sufficient electrical stimulus to become excited. Since the effect of current stimulus on a population of nerve fibers will be examined, it is important to be able to realistically simulate the distribution of nerve fiber diameters or sizes. The reason for this requirement is that the ease with which a nerve fiber is recruited is dependent upon its size. From a theoretical perspective, larger fibers are more easily recruited than smaller ones because they require less excitation current to reach threshold. To satisfy this requirement, a technique is described whereby a sequence of uniformly distributed random numbers can be transformed to conform to any arbitrary probability density function. This technique is then applied to the generation of a sequence of random numbers that correspond to anatomically observed distributions of peripheral nerve fiber diameters that have been reported in the literature.

2.1 Equivalent Circuit Model of the Nerve Axon

To model the effects of the imposed extracellular field on the myelinated nerve axon, a cable equivalent circuit model is used that consists of passive conductances and, in the time domain simulation, passive capacitances. This modeling approach is similar to the circuit introduced by Bean [29] and used by Sweeney and colleagues [47]. There are several assumptions inherent to this modeling approach. In actuality, the transmembrane conductance per unit area of the nerve axon is a non-linear function of the transmembrane potential and time. To simplify analysis, the assumption is made that the conductance of the membrane is linear up until the nerve fiber reaches excitation [29]. It has been experimentally verified that there is a range of current amplitudes less than or equal to the threshold current for which all excitable cells will exhibit linear behavior. For this range of excitation currents, the transmembrane potential will be directly proportional to the excitation current. As the excitation current approaches the threshold value, the non-linear behavior associated with the transmembrane conductance will begin to manifest itself. The range for which this linear behavior is observed is variable dependent upon the type of cell under consideration [38].

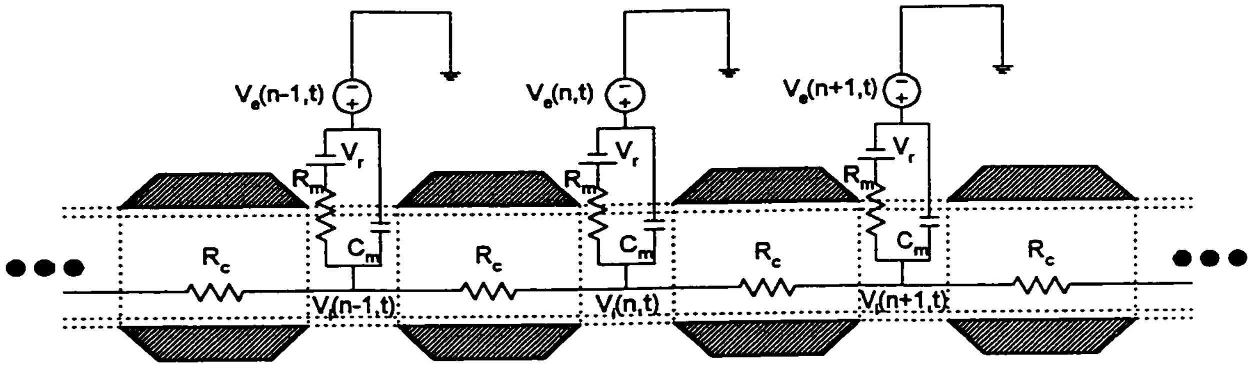

Figure 2.1 Equivalent circuit model of a section of myelinated axon. The circuit is superimposed on the axial cross section of the fiber in an attempt to relate the equivalent circuit components to the physical structure of the axon. In the diagram, R_c and R_m represent the resistance of the cytoplasm and the exposed section of membrane respectively. The parameter C_m represents the capacitance associated with the exposed section of the membrane. Extracellular potentials at the Nodes of Ranvier are represented by V_e and intracellular potentials by V_i where the n parameter denotes the specific Node of Ranvier and V_r is the resting membrane potential. The axon is assumed to continue on in both directions.

Figure 2.1 illustrates a section of the myelinated nerve axon and the associated electrical equivalent circuit model. The purpose of this figure is to demonstrate the relationship between the physical structure of the myelinated axon and the components in the equivalent circuit model. At the Nodes of Ranvier there is an exposed section of membrane of approximately 2.5μm in length. Only at these points is the membrane exposed to the extracellular environment. The intervening areas of membrane between the Nodes of Ranvier are insulated by the Schwann cells, in peripheral nerves, which are assumed to have an extremely high impedance relative to the bare membrane. Consequently, the assumption is made in virtually all models presented in the literature that the Schwann cells are effectively non-conducting. The membrane at the Nodes of

Ranvier has a resistive component R_m and a capacitive component C_m. In the interior of the cell, the cytoplasm is predominantly resistive and it is represented by the R_c resistors in the distributed circuit model. Extracellular potentials at the Nodes of Ranvier are denoted by V_e and intracellular potentials by V_i which are both discrete function of the specific Node of Ranvier at which the potential is specified.

Kirchhoff's current law can be invoked at the intracellular nodes to write a differential equation for the equivalent circuit model as shown in (2.1) where $V_m = V_i - V_e - V_r$ is the transmembrane potential.

$$\begin{aligned} C_m \frac{dV_m(n,t)}{dt} &+ G_m V_m(n,t) + G_c\left[V_e(n,t) + V_m(n,t)\right] \\ &- G_c\left[V_e(n-1,t) + V_m(n-1,t)\right] + G_c\left[V_e(n,t) + V_m(n,t)\right] \\ &- G_c\left[V_e(n+1,t) + V_m(n+1,t)\right] = 0 \end{aligned} \qquad \textbf{(2.1)}$$

$$\begin{aligned} C_m \frac{dV_m(n,t)}{dt} &+ G_m V_m(n,t) - G_c\left\{V_m(n-1,t) - 2V_m(n,t) + V_m(n+1,t)\right\} \\ &= G_c\left\{V_e(n-1,t) - 2V_e(n,t) + V_e(n+1,t)\right\} \end{aligned}$$

In the differential equations, G_c and G_m are the conductances or the inverse of the resistors R_c and R_m respectively shown in Figures 2.1 and 2.2. It should also be noted that the terms representing the extracellular potentials and the excitation sources in equations (2.1) and (2.2) are functions of both the position of the different Nodes of Ranvier, as indexed through the parameter n, and time represented by the variable t.

From a theoretical perspective, it can be shown that the potentials applied to the outside of the fiber are equivalent to a set of current sources applied intracellularly if these current sources are defined in a specific way in terms of the extracellular potentials. The equivalent circuit with intracellularly injected current sources is shown in Figure 2.2.

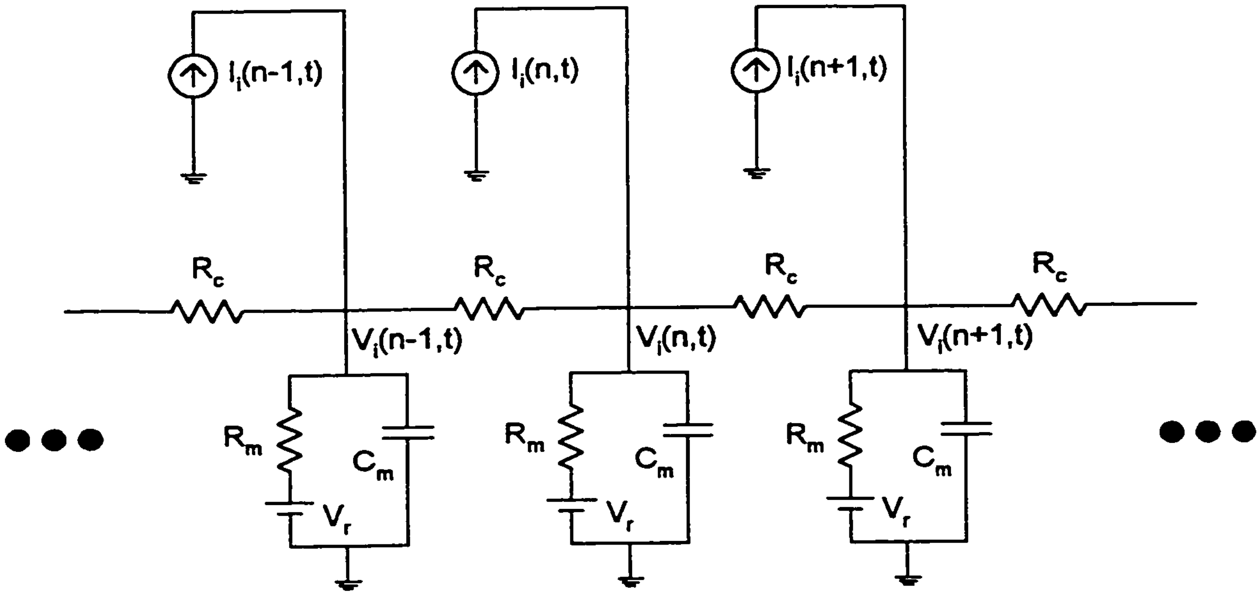

Figure 2.2 Intracellularly injected current equivalent circuit model of a myelinated axon. The equivalent circuit model of Figure 2.1 and Figure 2.2 are electrically equivalent provided that the current sources in Figure 2.2 are specifically chosen. Circuit parameters ***R_m***, ***C_m*** and ***R_c*** are defined the same way as in Figure 2.1. The intracellularly injected current sources labeled ***I_i*** take the specific Node of Ranvier number as an argument. The variables ***V_i*** and ***V_r*** are as outlined in Figure 2.1.

The differential equation for the intracellularly injected current equivalent circuit model is shown in (2.2).

$$C_m \frac{dV_m(n,t)}{dt} + G_m V_m(n,t) - G_c\{V_m(n-1,t) - 2V_m(n,t) + V_m(n+1,t)\} = I_i(n,t) \tag{2.2}$$

In order for the two models to be equivalent, the intracellularly injected current sources $I_i(n,t)$ must be chosen such that they are equivalent to the right hand term of equation (2.1) as per (2.3).

$$I_i(n,t) = G_c\{V_e(n-1,t) - 2V_e(n,t) + V_e(n+1,t)\} \tag{2.3}$$

The intracellularly injected current equivalent circuit model is used in the literature for nerve excitation simulations [41]. There are likely several reasons for this. From a circuit simulation perspective, the intracellular current injection circuit model lends itself more readily to conventional techniques for establishing the circuit equations.

It is a relatively straightforward task to compute the values of the equivalent circuit components C_m, R_m and R_c since they are based on the electrical properties of the axon membrane and the cytoplasm as well as the idealized geometry that has been assumed for the nerve axon. The capacitance per unit area of a cell membrane c_m is an important quantity in electrophysiological studies of cells and is often quoted in textbooks and the literature [33,43]. The distributed parameter capacitance that represents the capacitance of the cell membrane exposed to the extracellular medium can be calculated using the capacitance per unit area of the cell membrane multiplied by the surface area of the cylindrical portion of the membrane at the Node of Ranvier as per (2.4).

$$C_m = c_m 2\pi al \tag{2.4}$$

The radius of the axon membrane is represented by the variable a and the length of the Node of Ranvier by l. In a similar manner, an equation can be written for the resistance associated with the membrane that is exposed to the extracellular environment at the Nodes of Ranvier $\boldsymbol{R_m}$. In order to obtain the distributed membrane resistance value, the conductance per unit area $\boldsymbol{g_m}$ is used multiplied by the surface area of the cylindrical portion of the membrane exposed at the Node of Ranvier as per (2.5).

$$R_m = \frac{1}{G_m} = \frac{1}{g_m 2\pi a l} \tag{2.5}$$

Calculation of the value for the distributed axial resistance $\boldsymbol{R_c}$, requires that the resistivity of the cytoplasm ρ_c be known. The well known relationship between the resistance of a conductor, its resistivity, cross sectional area and length can then be invoked in the context of the idealized cylindrical geometry that has been assumed for the interior of the axon. The following formula for $\boldsymbol{R_c}$ can then be defined where $\boldsymbol{L}$ is the length from center to center between adjacent nodes of Ranvier.

$$R_c = \frac{\rho_c L}{\pi a^2} \tag{2.6}$$

There are more complex models available for representing the electrical behavior of a nerve fiber. Usually these models incorporate the non-linear conductance associated with the membrane. A study by Teicher and McNeal concluded that the response of both the linear nerve fiber models and the non-linear models to a pulse of 1000 μs duration predicted the same current thresholds to within 1% for any electrode/node distance between 0.5 mm and 20.0 mm [48]. The differences in predicted threshold current increased as the current pulse width decreased but were within 3% for pulse widths equal to 100 μs at a 2.0 mm distance and 11% for pulse widths of 10 μs at 2.0 mm. Since the difference is dependent on the duration of the stimulus pulse as well as the horizontal and vertical distance from the stimulating electrode and the electrode configuration, these results can only give a rough estimate of the threshold difference to be expected in a multi-fiber simulation. Although this study was reported in the late seventies, the authors emphasized that simulation of the more realistic non-linear model resulted in a twenty fold increase in the required computation time. The increase in computation time associated with the non-linear model would be prohibitive when performing excitation simulations on all but a very few fibers. Teicher and McNeal went on to state that for pulses that are of routinely used duration, such as 100 μs, the linear model provided a sufficiently close prediction of the required current to recruit the nerve fiber.

2.2 Nerve Fiber Diameter and its Impact on Electrical Recruitment

As can be seen from (2.5) and (2.6), axons that have larger diameters will have a lower membrane resistance at the Nodes of Ranvier $\boldsymbol{R_m}$ as well as a smaller axial resistance to current flow $\boldsymbol{R_c}$. It has been noted by several investigators that, based on qualitative considerations alone, larger diameter nerve fibers are more readily excited than smaller ones [2,49]. There have been some well documented theoretical simulations where the current required to excite a nerve fiber has been calculated from an equivalent circuit model of the nerve fiber and a simplified homogeneous, isotropic and infinite tissue environment assumption. These studies have corroborated the qualitative hypothesis [41]. In addition to it being easier to drive current into a larger fiber, larger diameter axons would also catch more of the current flux in the tissue environment by virtue of their physically bigger size than smaller fibers.

Although the effect of fiber diameter on nerve excitability is clear from a theoretical perspective, the situation is not as straightforward when the experimental literature is reviewed. Some investigators have reported seeing smaller motor units recruited first at relatively low levels of stimulus current amplitudes [50]. Since it is reasonable to assume that larger diameter motor nerve fibers would be associated with larger motor units, these results appear to be inconsistent with theory. These investigators blame the discrepancy on geometric factors such as the location of the nerve fiber in the nerve trunk relative to the stimulus electrode position. They also state that the discrepancy is unlikely associated with biophysical factors of the nerve fiber itself. It is however worth noting that some authors have observed that larger motor units are recruited first [51]. If a randomly generated population of nerve fiber diameters consistent with anatomically observed distributions is plotted in terms of its minimum current required to elicit recruitment, it is evident that most fibers are recruited at an extremely small fraction of the excitation required to elicit maximal recruitment as per the development illustrated in section 2.2.1. This clumping of the majority of the fiber diameter population at relatively low stimulus current intensities means that the excitation current difference required to recruit fiber diameters of different sizes, for the most part, is extremely small. Given this consideration, it is not surprising that somewhat smaller as well as larger motor units might be observed at low stimulus current amplitudes since even minute variations in position might be sufficient to alter the minimum stimulus current intensity required to recruit individual fibers.

2.2.1 Nerve Fiber Diameter Distributions

One of the most often quoted reference for anatomical distributions of nerve fiber diameters is the work of Boyd and Davey [52]. This work is definitive because not only are experimental measurements of nerve fiber diameter distributions for different types of efferent and afferent peripheral nerves presented, but suggested theoretical distributions of these nerve fibers with some parameters are also given.

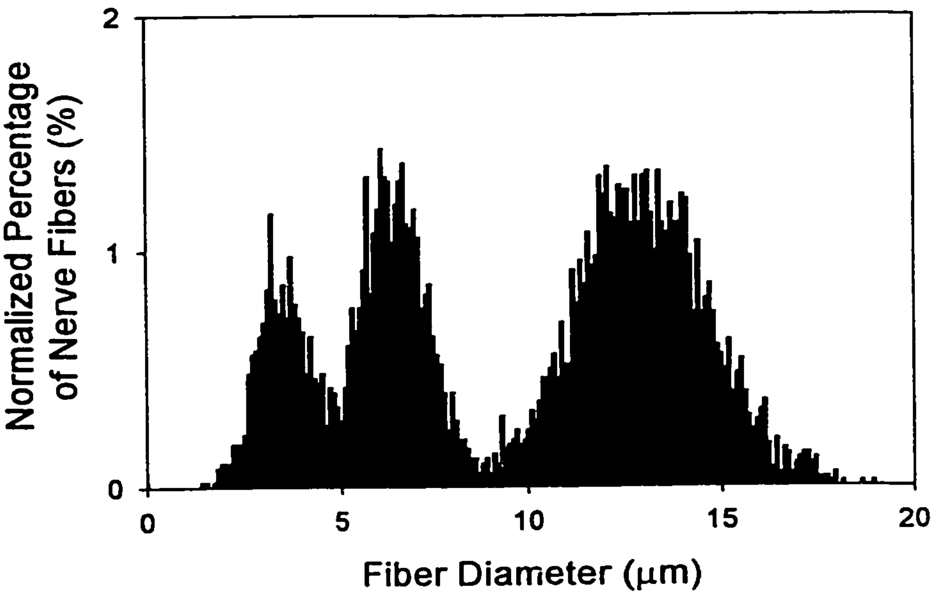

Figure 2.3 Efferent peripheral nerve fiber diameter histogram from simulated data. The histogram is drawn from the data plotted for 5000 randomly generated fibers consistent with efferent peripheral nerve distributions presented by Boyd and Davey [52]. Data is plotted as a percentage of the total number of fibers.

Figure 2.3 is a graph of 5000 randomly generated efferent peripheral nerve fiber diameters that are consistent with the distribution observed by Boyd and Davey for efferent peripheral nerves. It should be pointed out that the fiber diameter, as defined by Boyd and Davey, refers to the outer diameter of the axon including the myelin sheath.

The histogram from Figure 2.3 represents simulated data. A technique for simulating random distributions was applied to generate an anatomically consistent distribution of peripheral nerve fiber diameters [53]. This technique is based on the availability of a uniformly distributed random number generator between zero and unity. Since most mathematical software packages come with a uniformly distributed random number generator function or algorithm built in, the technique is relatively straightforward to implement.

The first step in applying this technique is to establish an approximate probability density function for the distribution. Boyd and Davey claim that the distributions of the individual grouping of fibers associated with efferent peripheral nerves, hereafter referred to as α, γ_f and γ_s motor nerves, are approximately Gaussian with the exception of the smallest group that has a slightly skewed Gaussian distribution.

For the purpose of the simulation, all three modes of the efferent fiber distribution have been modeled as Gaussian with the means and standard deviations outlined in Table 2.1. A mathematical expression can then be written for the assumed probability density function of efferent peripheral nerve fiber diameters. The equation consists of a summation of three different Gaussian functions that represent the individual groupings of fibers in the distribution. This categorization of fibers is long established in neurology and is based on size and function.

	α	γ_f	γ_s
Ψ	0.55	0.30	0.15
$\sigma(\mu m)$	1.7	0.8	0.6
$\mu(\mu m)$	13.0	6.50	3.50

Table 2.1 Parameters for the efferent fiber diameter distribution illustrated in Figure 2.3. The fiber groupings are also as per Figure 2.3 and the parameters correspond to those found in equation (2.7).

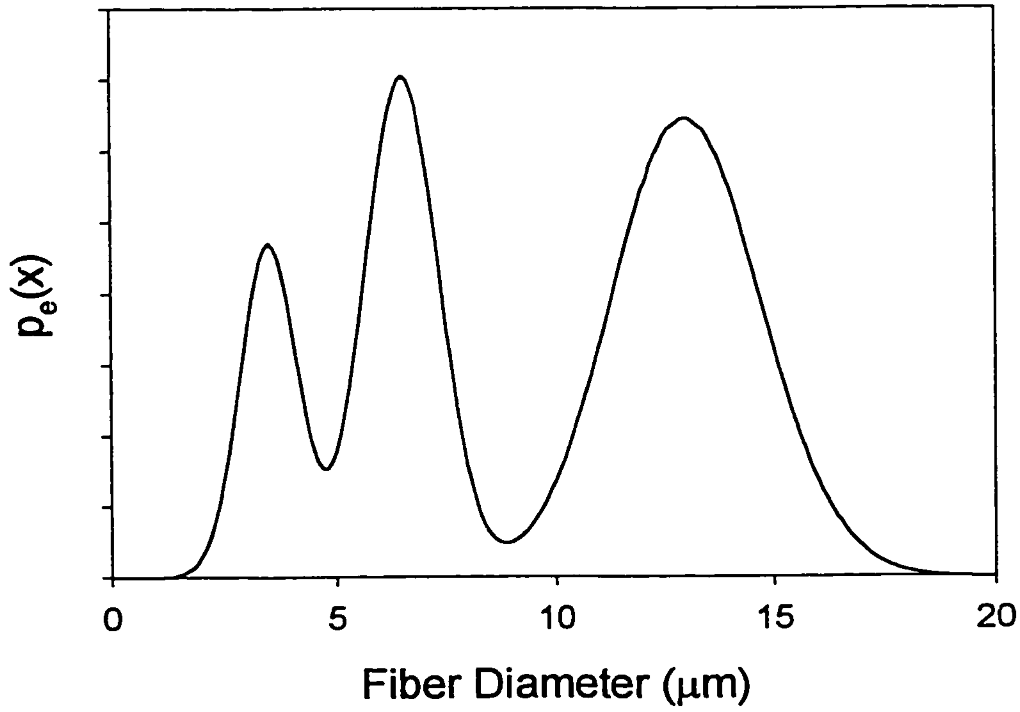

Figure 2.4 Graph of the assumed probability density function of efferent peripheral nerve fiber diameters. The parameters from Table 2.1 have been used.

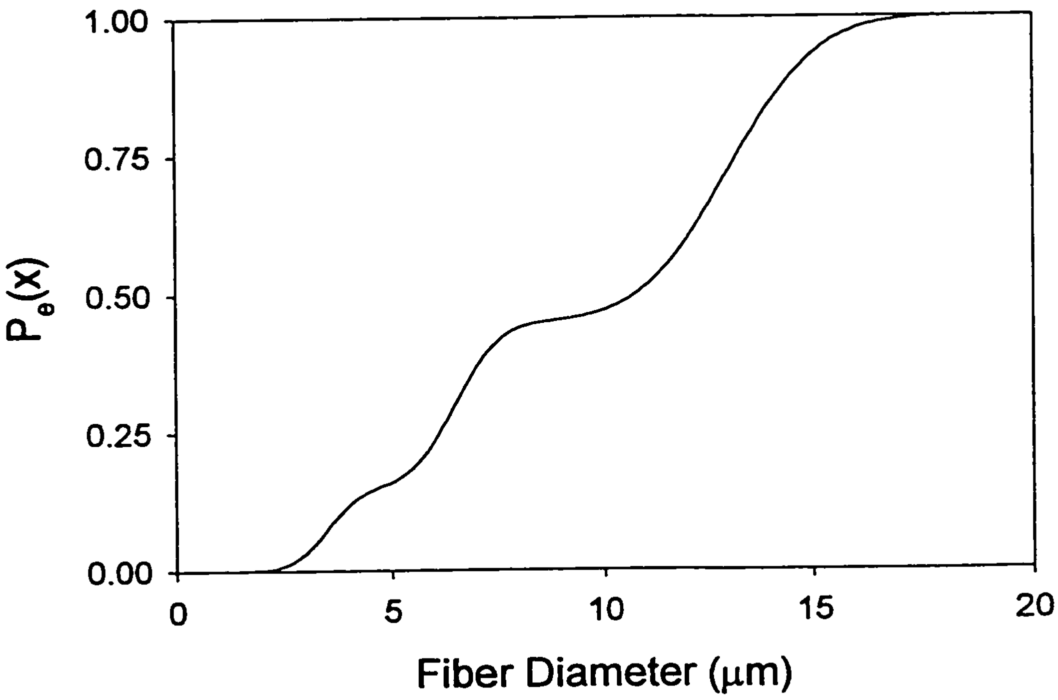

Figure 2.5. Graph of the cumulative distribution function of efferent peripheral nerve fiber diameters. The plot is calculated from the assumed equation for the probability density function (2.7) and uses the parameters of Table 2.1.

$$p_e(x) = \frac{\Psi_\alpha}{\sigma_\alpha\sqrt{2\pi}} e^{-\frac{(x-\mu_\alpha)^2}{2\sigma_\alpha^2}} + \frac{\Psi_{\gamma f}}{\sigma_{\gamma f}\sqrt{2\pi}} e^{-\frac{(x-\mu_{\gamma f})^2}{2\sigma_{\gamma f}^2}} + \frac{\Psi_{\gamma s}}{\sigma_{\gamma s}\sqrt{2\pi}} e^{-\frac{(x-\mu_{\gamma s})^2}{2\sigma_{\gamma s}}} \qquad (2.7)$$

Figure 2.4 is a plot of the probability density function of (2.7) with the parameters of Table 2.1.

Once the assumed fiber diameter probability density function has been established, the cumulative distribution function must be calculated by integrating the probability density function as per (2.8).

$$P_e(x) = \int p_e(x)dx \tag{2.8}$$

In general, a solution to (2.8) can be obtained numerically or in closed form assuming that the pdf is simple enough to integrate or that a closed form solution exists. In the case of the efferent peripheral nerve pdf proposed in (2.7), the presence of the Gaussian functions preclude a closed form solution to the integral of (2.8). Figure 2.5 is the cumulative distribution function (cdf) from the pdf of (2.7). Once the cdf has been obtained numerically or in closed form, the transformation of (2.9) can be applied to a sequence of the uniformly distributed random variable denoted by $\boldsymbol{u}$.

$$x = P_e^{-1}(u) \tag{2.9}$$

The sequence of the random variable $\boldsymbol{x}$ generated by way of the transformation of (2.9) will have a distribution consistent with the assumed probability density function of (2.7). A few words about the transformation procedure should be mentioned. As was the case with obtaining the cumulative distribution function, the inverse $\boldsymbol{P_e^{-1}}$ of the cumulative distribution function can be obtained either in closed form or the sequence $\boldsymbol{x}$ can be calculated numerically. The advantage to the closed form approach is that the sequence of uniformly distributed random numbers can be substituted directly into the expression for the inverse to obtain the desired output sequence. Unfortunately, in this case, a closed form expression for the inverse is not obtainable.

This is the procedure that was used in obtaining the histogram of the distribution of efferent peripheral nerve fiber diameters shown in Figure 2.3. The technique described previously is general enough to be useful in a wide variety of applications [53].

The random variable associated with the nerve fiber diameter can be transformed in accordance with the graph of the minimum stimulus current amplitude required to excite the fiber versus the fiber diameter as shown in Figure 2.6. When this random variable transformation is completed, the sequence of randomly generated nerve fiber sizes can be represented in a histogram that shows the number of fibers recruited versus a minimum stimulus current amplitude.

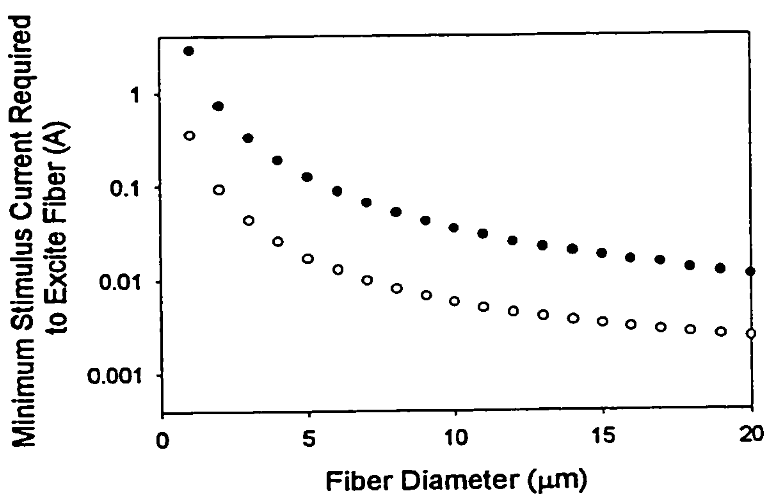

Figure 2.6 Plot of the minimum stimulus current amplitude required to excite versus the nerve fiber diameter. In this graph, the vertical distance, or depth, from the monopolar stimulus electrode is taken as a parameter. The solid circles represents the 10 mm depth case and the unfilled circles represent the 5mm depth case. The parameters associated with the electrical properties of the nerve fibers are identical to those presented in Chapter 4 of this thesis. The potential profile in the assumed homogeneous and isotropic tissue medium is calculated using the relationship of (3.7) with an assumed tissue resistivity of 4.575 Ωm. A 25 mV threshold potential is assumed.

Figure 2.7 is a histogram that shows the number of nerve fibers that are recruited versus a given stimulus current. The data for this histogram was obtained by transforming the sequence of numbers in the fiber diameter distribution of Figure 2.3. A random variable transformation was performed numerically in accordance with the 10 mm depth minimum stimulus current amplitude required to excite versus fiber diameter curve of Figure 2.6. Due to the nature of the minimum stimulus current amplitude required to excite versus fiber diameter curves, all but the smallest nerve fibers will be excited at relatively low stimulus current amplitudes.

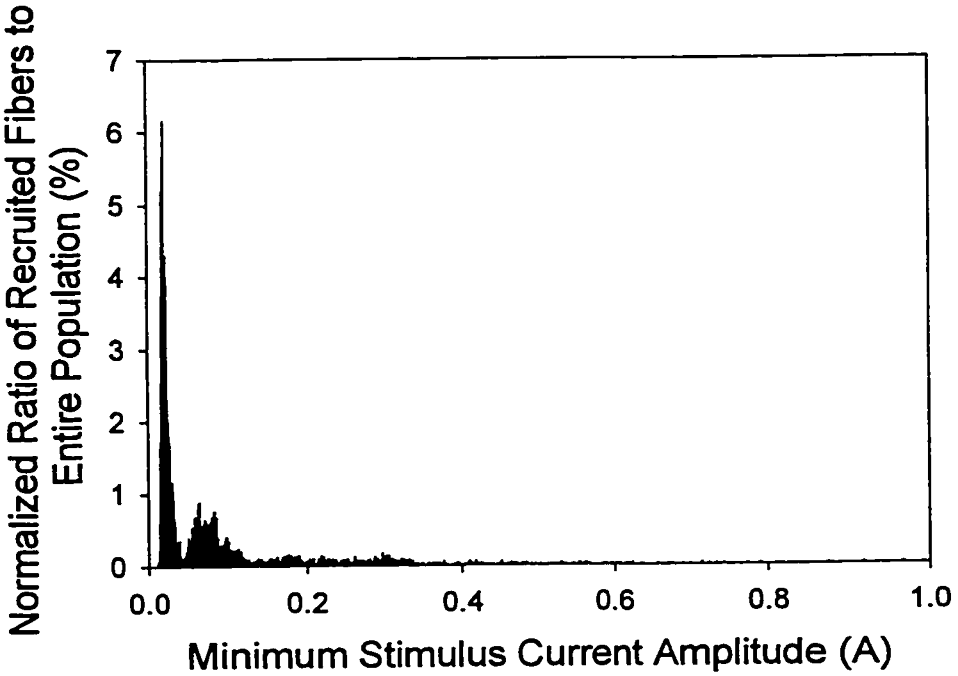

Figure 2.7 Histogram of the number of nerve fibers versus the minimum stimulus current required to reach excitation. The data for this histogram was taken from the efferent fiber diameter data used to plot the histogram of Figure 2.3. A random variable transformation was applied numerically in accordance with the 10 mm depth curve of Figure 2.6.

For the histogram shown in Figure 2.7, a stimulation current amplitude that is 10% of the minimum current required to excite the smallest 1 micron diameter nerve fiber will be sufficient to excite 94.6% of the population of fibers. This analysis assumed that the population is at a depth of 10 mm in the homogeneous isotropic tissue environment. Figure 2.8 demonstrates that the histogram of fibers versus minimum stimulus current amplitude required to recruit is even more compressed at low current levels for a smaller depth of 5 mm.

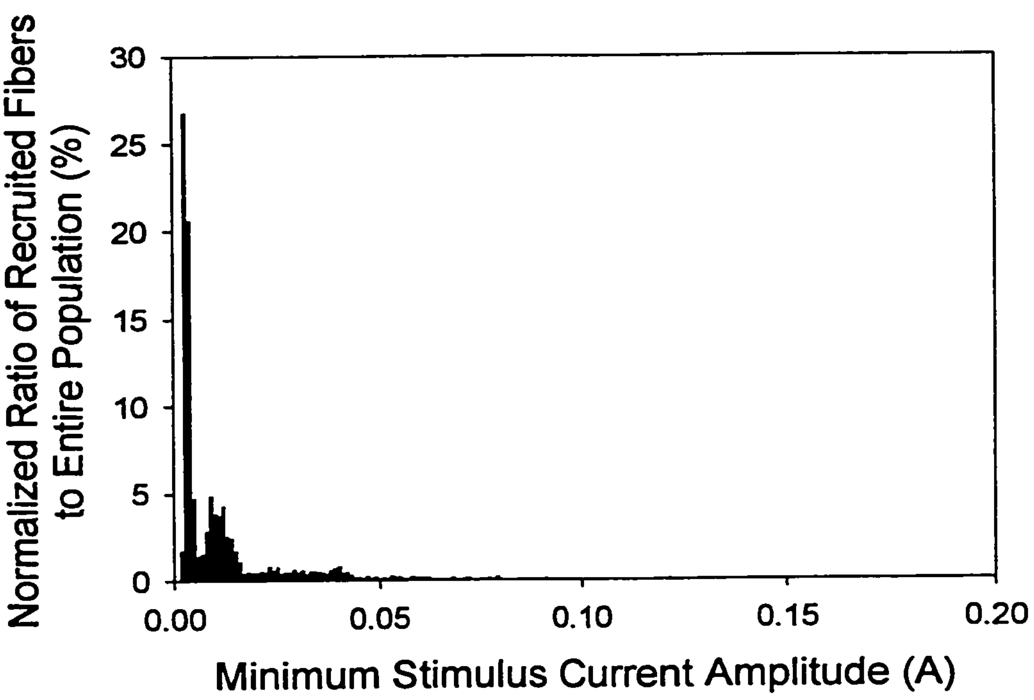

Figure 2.8 Histogram of the number of nerve fibers versus the minimum stimulus current required to reach excitation. The data for this histogram was taken from the efferent fiber diameter data used to plot the histogram of Figure 2.3. A random variable transformation was applied numerically in accordance with the 5 mm depth curve of Figure 2.6.

2.3 The Equivalent Circuit Model of Skeletal Muscle Tissue

One of the principal reasons that an electrical equivalent circuit model for skeletal muscle tissue was developed and presented in the literature by Gielen and colleagues, was the desire to compare the theoretically predicted electrical conductivity calculated from the model with conductivity measurements made in the laboratory. There are two complications associated with the nature of skeletal muscle tissue that must be discussed before a model of the tissue conductivity can be developed. First, skeletal muscle tissue is electrically anisotropic. This anisotropic nature of skeletal muscle tissue can be measured in the laboratory as per the procedures outlined in Appendix B. The conductivity measured in the directions transverse and parallel to the long axis of the cylindrical fibers differs by approximately a factor of 3 [9]. Previous investigators have approached the problem of modeling the anisotropy by developing two separate equivalent circuits for the parallel and the transverse directions.

2.3.1 Effective Conductivity

In addition to the complication of anisotropy, inhomogeneity is another characteristic of skeletal muscle tissue. Since skeletal muscle tissue is not a homogeneous material, in that it consists of, at a simplified level of separation, the cell membrane and the cytoplasm, the standard definition of conductivity for a homogeneous material as defined in (2.10), where Z is the impedance, cannot be applied [54].

$$\sigma_c = \frac{L_c}{Zs_c} \tag{2.10}$$

Figure 2.9 illustrates the geometric parameters associated with equations (2.10) and (2.11) where L_c is the length of the medium and S_c is the surface area in the direction perpendicular to current flow.

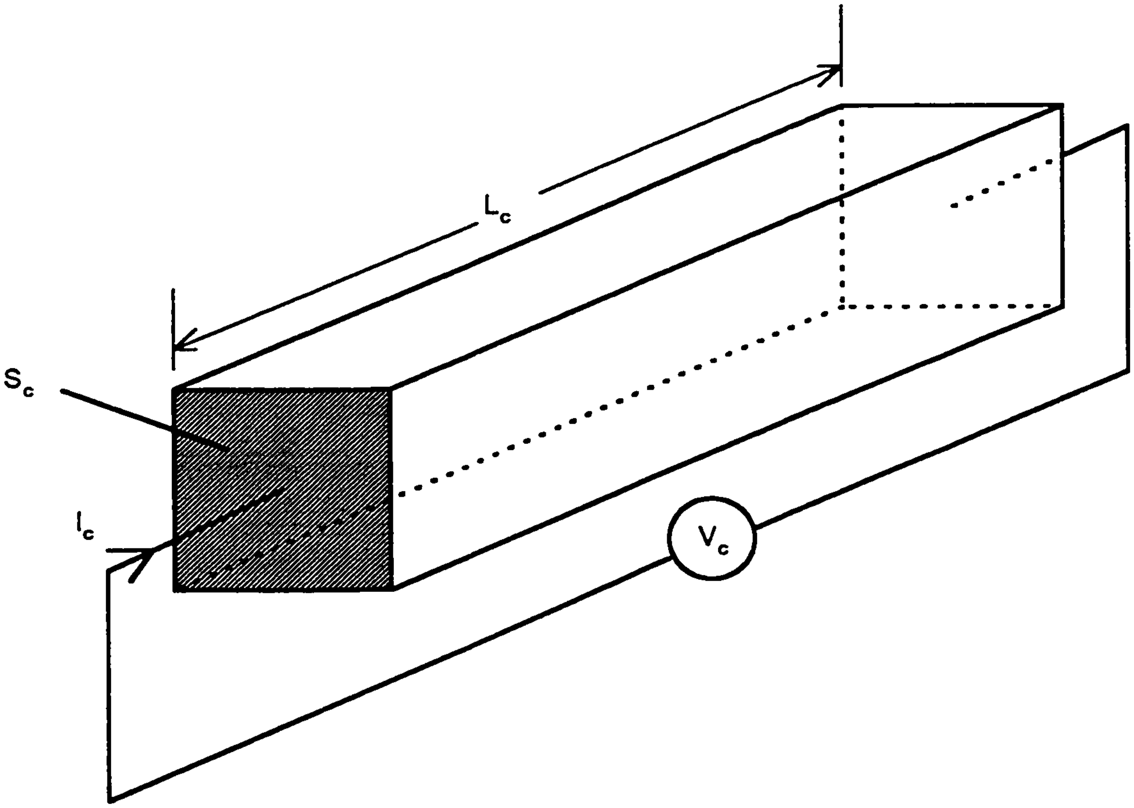

Figure 2.9 Idealized representation of effective conductivity measurement of an inhomogeneous material. The drawing illustrates the current flow I_c that is perpendicular to the surface S_c. A potential of V_c volts is measured between the two boundaries. The section of material has a length L_c.

The effective conductivity σ_{eff} for an inhomogeneous medium is defined in terms of the potential difference on the two opposite boundaries of the medium and the current flow perpendicular to the boundaries. The surface area of the boundaries and the length of the medium are also parameters. Effective conductivity is defined as in (2.11). No information about the current distribution or the potential field between the two measurement boundaries of the medium is implied by the effective conductivity.

$$\sigma_{eff} = \frac{L_c}{\frac{V_c}{I_c} S_c} \tag{2.11}$$

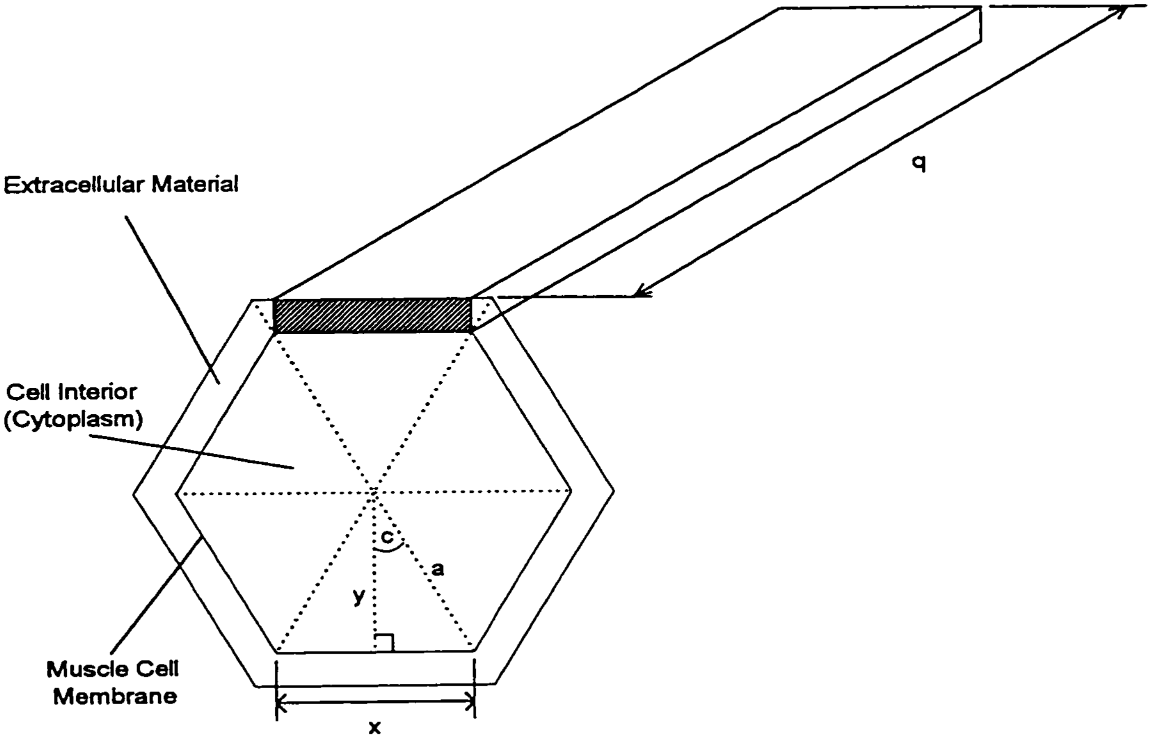

Figure 2.10 Idealized hexagonal geometry of a muscle fiber. Various lengths and angles are shown on the diagram that relate to the formulas developed in the text.

Since the highly simplified equivalent circuit model used for simulating the conductivity parallel to the long axis of the skeletal muscle fiber is similar to the nerve axon equivalent circuit developed earlier, this model will be discussed first. Although the models are similar, it should be emphasized that the internal organization of muscle fiber is very different from nerve axons. The model is simplified to resemble nerve fibers with only a cytoplasmic interior. Nicholson [25] and Gielen's [26] approach to defining an idealized geometry for the skeletal muscle fiber was to assume that the fiber was hexagonal in shape. The procedures involved in calculating the equivalent circuit model parameters is somewhat more complicated under the assumption of a hexagonal geometry. Figure 2.10 is a drawing of the cross section of a muscle fiber that illustrates the geometric variables of interest. A section of the membrane for one side of the hexagonal fiber is also shown illustrating the third dimension. Figure 2.11 illustrates the parallel equivalent circuit model of the muscle fiber and its relationship to the idealized hexagonal geometry of the fiber that has been assumed.

In Figure 2.11, the distributed parameter resistance R_{EP} represents the resistance of the extracellular material to current flow in the direction parallel to the muscle fiber long axis. The resistance R_{MP} and C_{MP} represent the resistance and capacitance respectively of a section of cell membrane.

The extracellular resistance parameter R_{EP} can be obtained from the well known relationship between the resistance of a homogeneous conductor, its resistivity ρ_E, surface area S_{EP} and length q as per (2.12).

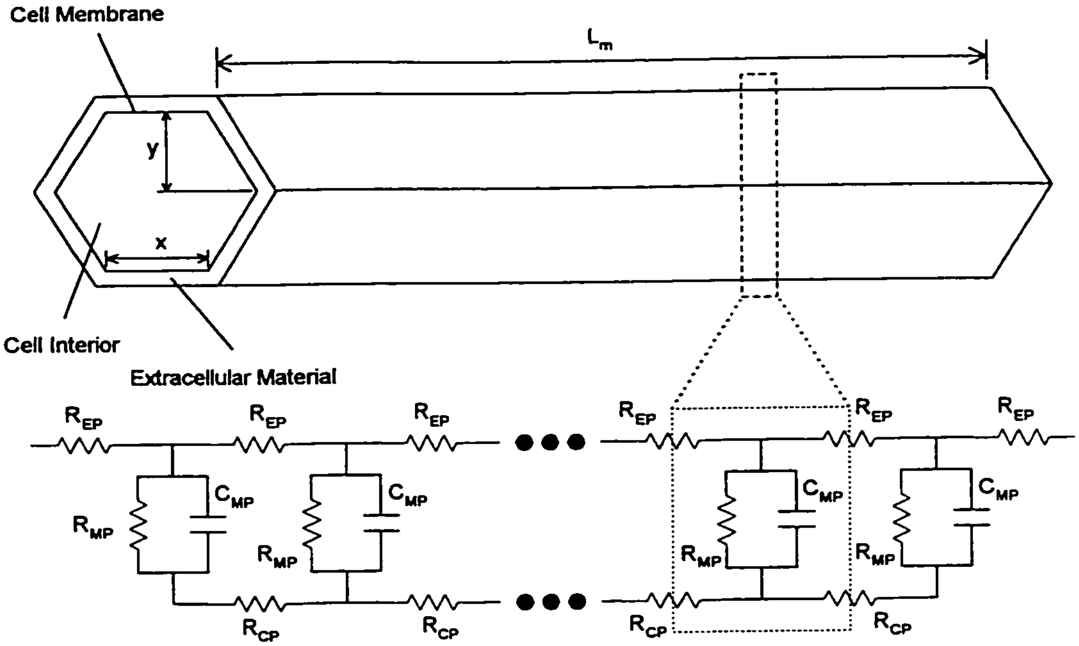

Figure 2.11 Parallel skeletal muscle tissue conductivity equivalent circuit model. The diagram illustrates the relationship between the equivalent circuit and the idealized hexagonal muscle fiber. In the diagram R_{EP} represents the longitudinal resistance of the extracellular material, R_{MP} and C_{MP} represent the resistance and capacitance respectively of a section of membrane and R_{CP} represents the longitudinal resistance of the cytoplasm. The geometric parameters are shown on the muscle fiber diagram.

$$R_{EP} = \frac{\rho_E q}{S_{EP}} \tag{2.12}$$

The only challenge in calculating this quantity, is developing an expression for the surface area of the extracellular material S_{EP}. Empirical measurements of the resistivity ρ_E can be obtained from the literature. An expression for the interior cross sectional surface area of the muscle fiber S_{FP} can be obtained by dividing the interior hexagonal region into six equal sections and then applying trigonometry to obtain values for x and y. A simple relationship for the area of a triangle can be applied and multiplied by six to obtain the overall cross sectional interior surface area of the hexagon as per (2.13).

$$S_{FP} = 3xy \tag{2.13}$$

If the ratio of the fiber interior volume to the total volume of the fiber including the hexagonal section of surrounding extracellular material is specified as ***p***, then the surface area of the extracellular material can be obtained from (2.14). It is important to note that inherent to this assumption is that the cross sectional surface area of the muscle fiber cell membrane is negligible compared to the dimensions of the interior and extracellular surface areas. This is in fact a good approximation since the width of the muscle fiber membrane is on the order of 10 angstroms [39].

$$S_{EP} = S_T - S_{FP} = \frac{S_{FP}}{p} - S_{FP} \tag{2.14}$$

Calculation of the membrane longitudinal cytoplasmic resistance can be done in a similar fashion by invoking (2.12) and using the value for the cytoplasm resistivity ρ_C, the cross sectional surface area of the muscle fiber interior S_{FP} and the length of the segment q as per (2.15).

$$R_{CP} = \frac{\rho_C q}{S_{FP}} \tag{2.15}$$

The membrane resistance and capacitance is an empirically measured quantity that is typically quoted as a per unit area value. In order to obtain the distributed parameter values for R_{MP} and C_{MP}, it is necessary to multiply the per unit area values by the surface area of the assumed geometrical shape of the muscle fiber P_{FP} which can be calculated as per (2.16).

$$P_{FP} = 6xq \tag{2.16}$$

Once the surface area has been calculated, the formula for R_{MP} and C_{MP} are straightforward.

$$G_{MP} = \frac{1}{R_{MP}} = P_{FP} g_m \tag{2.17}$$

$$C_{MP} = P_{FP} c_m \tag{2.18}$$

As mentioned previously, a different equivalent circuit model must be used to describe the conductivity in the transverse direction to the muscle fibers. The model proposed by Gielen and his colleagues [26] is based on a region taken from a cross section of muscle fibers that is perpendicular to the long axis of the fibers. The equivalent circuit model and its relation to the geometry of the cross section of muscle fibers is illustrated in Figure 2.12.

The extracellular resistance R_{ET} can be calculated by determining the resistance of the homogeneous block of extracellular material circumscribed by the rectangle ABDC in Figure 2.12. Since the entire surface AA' is assumed to be at an equipotential as is the surface II', the current flow is perpendicular to these two surfaces. The following formula can be applied to calculating the resistance R_{ET}.

$$R_{ET} = \frac{\rho_E x}{2dq} \tag{2.19}$$

Values for the membrane resistance and capacitance, R_{MT} and C_{MT} respectively, can also be obtained by multiplying the top surface area of the rectangle ABDC with the membrane conductance and capacitance per unit area as per (2.20) and (2.21).

$$R_{MT} = \frac{1}{G_{MT}} = \frac{1}{g_m q x} \tag{2.20}$$

$$C_{MT} = c_m q x \tag{2.21}$$

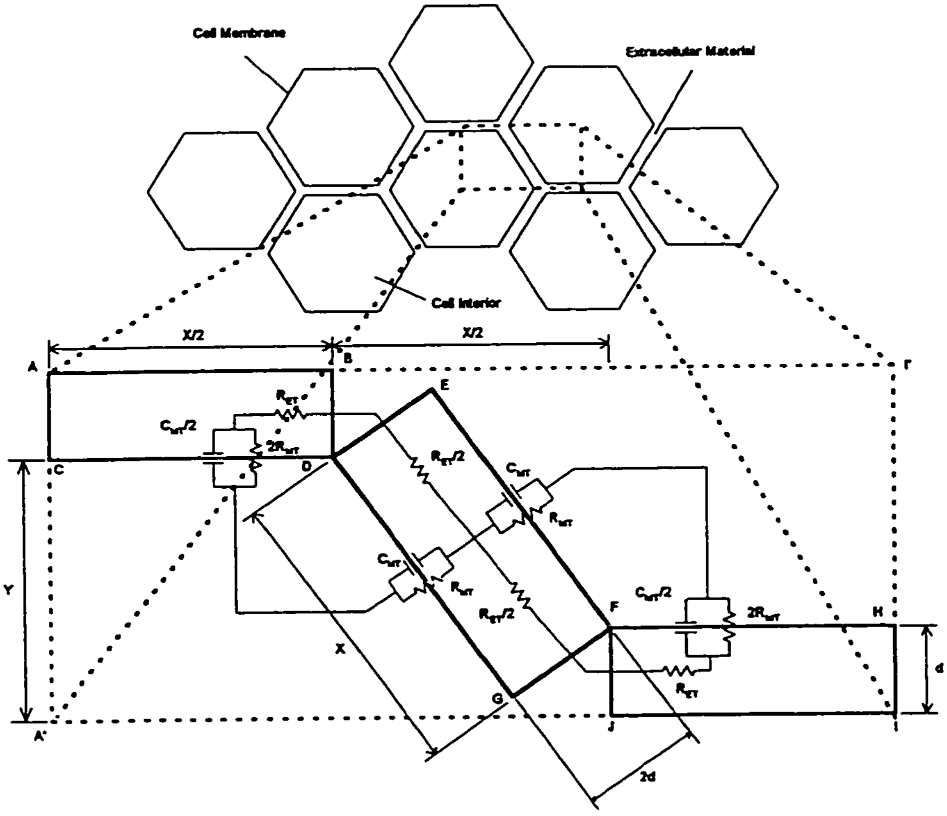

Figure 2.12 Transverse skeletal muscle tissue conductivity equivalent circuit model. The model by Gielen and colleagues [26] is based on the cross section through a group of fibers that is perpendicular to the fiber long axis. An illustration of a group of muscle fibers is presented with a box outlining the region on which the equivalent circuit model is based. Below is an expanded view of the region showing the dimensions of the important geometric parameters with an overlay of the equivalent circuit model. In the circuit R_{MT} and C_{MT} represent the resistance and the capacitance through the muscle fiber membrane. The resistance R_{ET} is associated with the path that the current can take through the extracellular material.

Once the impedance, as a function of frequency, is simulated using SPICE for the transverse and the parallel conductivity circuits presented in Figures 2.12 and 2.11, the effective conductivity formula of (2.11) must be applied to obtain the frequency dependent conductivity curves.

Figure 2.13 and 2.14 represent the frequency dependent complex conductivity magnitude and phase simulated from the circuits of Figures 2.11 and 2.12 using SPICE. The electrical and geometric parameters used in calculating the circuit components for the simulations shown in Figures 2.13 and 2.14 are given in Table 2.2. As a basis of comparison, the theoretical closed form expressions developed by Gielen *et al.* [26] have also been plotted.

For the longitudinal direction parallel to the long cylindrical axis of the skeletal muscle fibers, there is a close match between the modified equivalent circuit model of Figure 2.11 and the conductivity predicted by Gielen's expression (2.22) with the parameter λ as defined in (2.23). In equations (2.22) and (2.23) the variables σ_{LM} is the longitudinal effective conductivity, p is the ratio of the muscle fiber interior volume to the total volume, y is the longitudinal distance, σ_i and σ_e are the intracellular and extracellular conductivities respectively, g_m and c_m are the per unit area membrane conductance and capacitance respectively, a is the cross sectional interior fiber radius and S_T is the muscle fiber total cross sectional area. The difference between the SPICE circuit model conductivity and the conductivity predicted by Gielen's formula is due to the fact that in the derivation of (2.22) there is an infinite distance assumed between the source and sink current electrodes. There is no such assumption inherent in the equivalent circuit model of Figure 2.11.

$$\sigma_{LM} = \frac{\sigma_e(1-p)+\sigma_i p}{1+\dfrac{1-e^{-\lambda y}}{\lambda y}\dfrac{\sigma_i p}{\sigma_e(1-p)}} \tag{2.22}$$

$$\lambda = \sqrt{a(g_m + j\omega c_m)[\{\sigma_e(1-p)S_T\}^{-1} + \{\sigma_i p S_T\}^{-1}]} \tag{2.23}$$

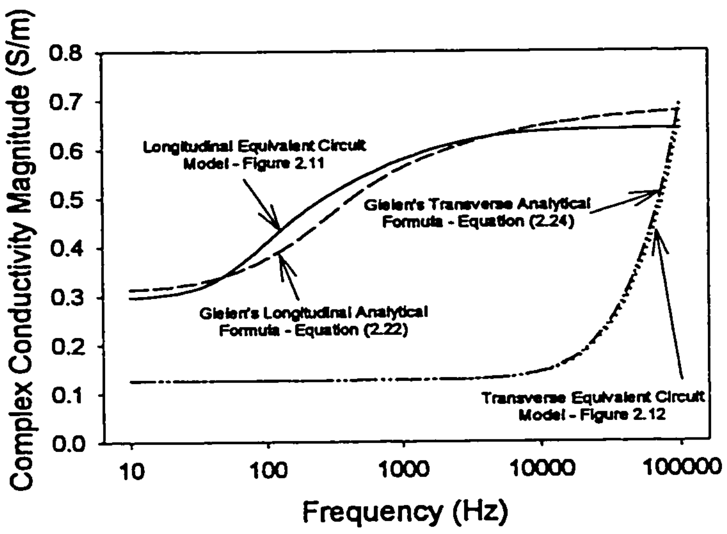

Figure 2.13 Semi-logarithmic graph of the magnitude of the frequency dependent complex transverse and longitudinal skeletal muscle tissue conductivity as simulated with the equivalent circuit models of Figures 2.11 and 2.12. Two additional curves are included that have been calculated from the closed form expressions developed by Gielen and colleagues [26]. — - Gielen's longitudinal direction analytical formula - Equation (2.22). —- Longitudinal direction equivalent circuit simulation - Figure 2.11. ••• - Transverse Equivalent Circuit Simulation - Figure 2.12. - •• - - Gielen's transverse direction analytical formula - Equation (2.24). The equivalent circuit parameters for the parallel model are R_{EP}=5.8×10^4 Ω, R_{CP}=3.1×10^4 Ω, R_{MP}=1.0×10^7 Ω and C_{MP}=7.5×10^{-10} F. The equivalent circuit parameters for the transverse model are R_{ET}=4.3×10^3 Ω, R_{MT}=6.0×10^6 Ω and C_{MT}=1.3×10^{-9} F.

σ_i	5.0×10^{-1} S/m	p	0.9
σ_e	2.4 S/m	x	5.0×10^{-5} m
g_m	3.3 S/m^2	y	4.3×10^{-5} m
c_m	2.5×10^{-2} F/m^2	L_m	2.4×10^{-3} m
a	5.0×10^{-5} m	d	2.4×10^{-6} m

Table 2.2 Electrical and geometric parameters used in calculating the equivalent circuit components of the complex parallel and transverse conductivity equivalent circuit models for the simulations shown in Figures 2.13 and 2.14. For the parallel circuit, 24 100 μm segments were used.

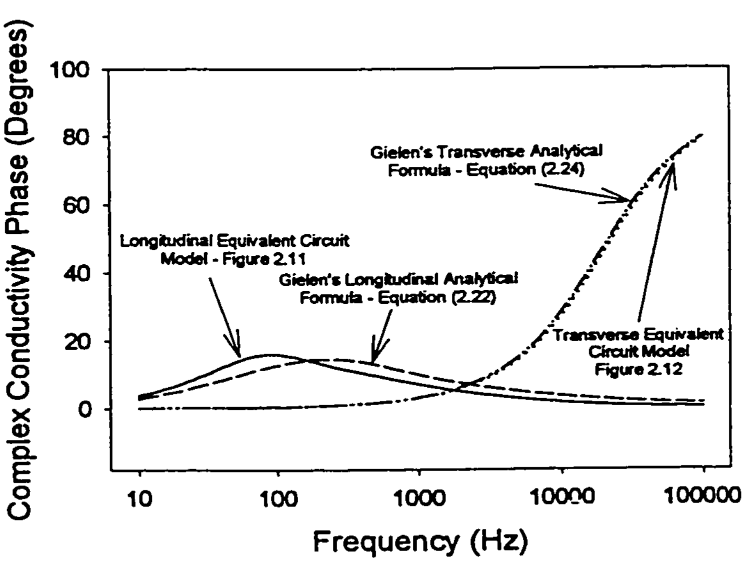

Figure 2.14 The above semi-logarithmic graph shows the phase of the frequency dependent complex transverse and longitudinal skeletal muscle tissue conductivity as simulated with the equivalent circuit models of Figures 2.11 and 2.12. Two additional curves are included that have been calculated from the closed form expressions developed by Gielen and colleagues [26]. — - Gielen's longitudinal direction analytical formula - Equation (2.22). — - Longitudinal direction equivalent circuit simulation - Figure 2.11. ••• - Transverse Equivalent Circuit Simulation - Figure 2.12. - •• - - Gielen's transverse direction analytical formula - Equation (2.24). The equivalent circuit parameters for the parallel model are R_{EP} =5.8×10^4 Ω, R_{CP} =3.1×10^4 Ω, R_{MP}=1.0×10^7 Ω and C_{MP}=7.5×10^{-10} F. The equivalent circuit parameters for the transverse model are R_{ET}=4.3×10^3 Ω, R_{MT}=6.0×10^6 Ω and C_{MT}=1.3×10^{-9} F.

In effect, the equivalent circuit of Figure 2.11 represents a distributed parameter model similar to the one proposed by Gielen from which he developed the closed form expression of (2.22). To determine if the conductivity predicted by the equivalent circuit of 2.11 was convergent, simulations were carried out in which the segment lengths were successively halved and the predicted frequency dependent conductivity curves were plotted. It was found that the difference between conductivity curves decreased with decreasing segment length.

$$\sigma_{TM} = \frac{\sqrt{3}a\left(g_m + jwc_m\right)}{2} + \frac{(1 - p)\sigma_e}{1 + p} \tag{2.24}$$

For the transverse direction, the match between the conductivity phase and magnitude predicted by the equivalent circuit model of Figure 2.12 and the expression developed by Gielen (2.24) is very close. The fact that the two responses are so similar is not surprising since both the equivalent circuit model and (2.24) were obtained from the same geometry. There is a small discrepancy between the two responses that is attributable to an approximation made in developing the closed form expressions specifically that the thickness of the extracellular region is much smaller than the hexagonal radius.

The advantages of having SPICE compatible equivalent circuit models that can be used to simulate tissue impedance characteristics are significant when designing tissue stimulation circuitry. By scaling the effective tissue conductivity σ_{eff} with the appropriate geometric parameters, an accurate representation of the inhomogeneous tissue load impedance can be included in a combined circuit simulation with the stimulator electronics.

Chapter 3: Finite Difference Simulations of Electrical Tissue Stimulation

In this chapter the theory behind a finite difference simulation of the potential distribution in skeletal muscle tissue during electrical current stimulation is presented. This description includes a discussion as to how the simulation grid is defined for the anisotropic conductivity case. It should be noted that in the finite difference simulations the assumption of isotropy that is commonly used in the literature has been removed.

In order to determine the impact of the isotropy assumption on the potential solution, the potential distribution associated with electrical current stimulation in anisotropic skeletal muscle tissue is compared to the solution for the isotropic case. The results demonstrate that there is a significant error associated with the assumption of isotropic tissue properties in calculating the potential distribution along an axon. Simulation studies indicate that the isotropy assumption is worst under bipolar electrode stimulation as opposed to monopolar stimulation and that the bipolar error increases as the distance between electrodes decreases. In light of these results, it is concluded that in order to avoid large errors in the calculated potential distribution along an axon, the isotropy assumption should only be used when the transverse depth from the electrode to the nerve is relatively small.

3.1 Finite Difference Simulations

The finite difference technique lends itself well to electromagnetic field problems in which there are inherent anisotropies associated with the electrical properties of the material under investigation. In addition, the technique can be readily applied where there are inhomogeneities that would make a closed form solution impractical [55]. Since the problem being solved is finite in size with specific boundary conditions, it is well suited towards implementation on digital computers.

The finite difference simulations undertaken in this study involved a two dimensional resistive grid where it was assumed that the field quantities do not vary in the third dimension. Figure 3.1 illustrates the idealized geometry associated with the simulations. The nerve trunk has been simplified to a single fascicle with epineurium. Perineural and endoneural tissues have been ignored. As well, the diameter for the fascicle is slightly larger than would be encountered in man to allow the calculation of intraneural fields using the grid spacing selected. The electrodes are approximated as point current sources that lie on the surface of an isotropic subcutaneous tissue layer. For the sake of simplicity, the effect of skin impedance has been ignored because of high resistivity [3]. A condition of zero current flow normal to the boundary was instituted for the tissue surface with the exception of electrode nodes. These constraints constitute the Neumann boundary condition at the tissue surface. Inside the tissue, at relatively large longitudinal and transverse distances from the electrode, the potential would decay to zero. A zero potential Dirichlet boundary condition was therefore applied to the other three simulation boundaries. Truncation of the simulation domain at points where the potential is relatively constant is permitted [55]. When using the field simulations in conjunction with nerve excitation studies, the validity of the finite domain size approximation is reinforced since the spatial distribution of the excitation currents driving the nerve fiber is proportional to the second derivative of the extracellular potential along the length of the fiber [30]. This observation can be used as a further check as to the adequacy of the simulation domain size.

The formulation of the finite difference equations follow from three fundamental relationships of electromagnetic theory, specifically the divergence of the current density, the elemental form of Ohm's Law and the equivalence between the electric field and the negative gradient of the scalar potential:

$$\nabla \cdot J = I_s \tag{3.1}$$

$$J = \sigma E \tag{3.2}$$

$$E = -\nabla \phi \tag{3.3}$$

In (3.1) (3.2) and (3.3) J represents the current density in A/m^2, I_s is the source current density in A/m^3, σ is the conductivity in S/m, ϕ is the potential in volts and E represents the electric field in V/m. These expressions can be combined resulting in a second order differential equation that relates the Laplacian of the potential to the source current:

$$-\sigma \left(\nabla^2 \phi\right) = I_s \tag{3.4}$$

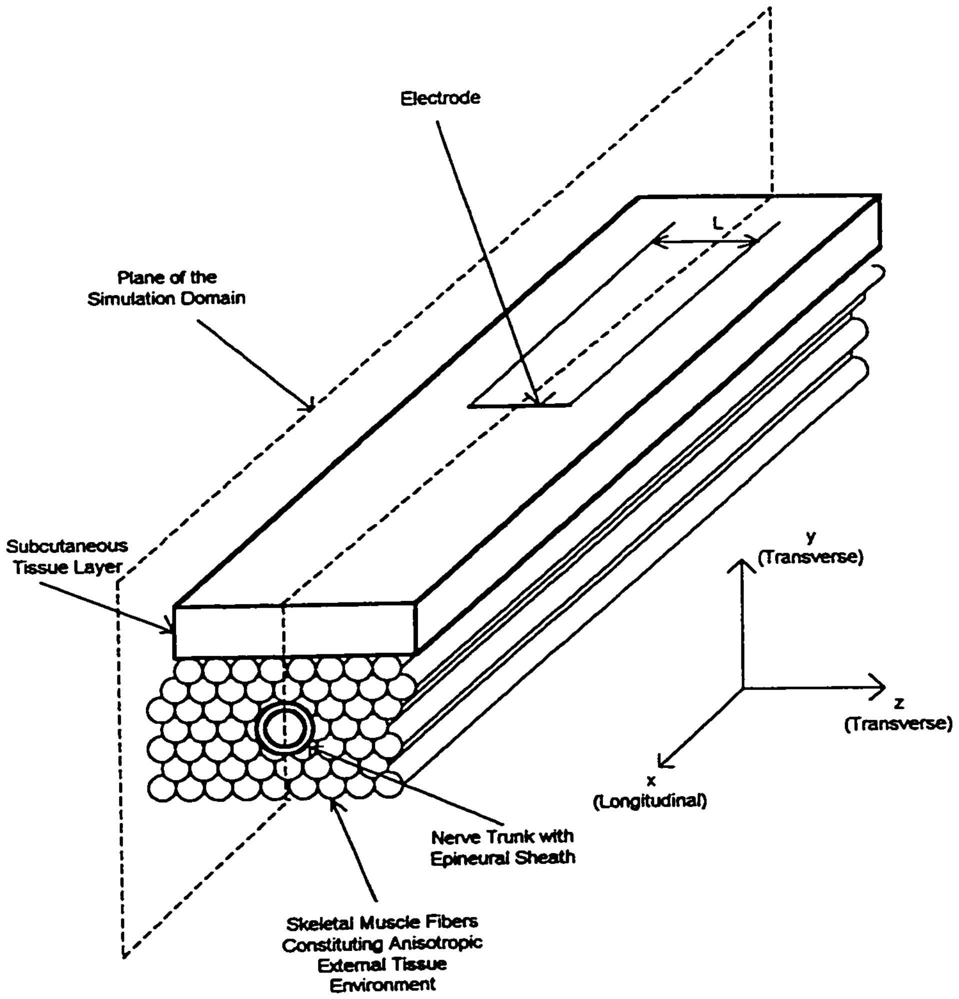

Figure 3.1(a) Representation of a section of tissue. This section includes a 0.5 cm layer of isotropic subcutaneous tissue. The electrodes are assumed to lie on the surface of the subcutaneous tissue layer. An intervening layer of anisotropic tissue exists between the subcutaneous tissue layer and the nerve trunk. The section is assumed to pass through the idealized nerve trunk structure that consists of a 1mm thick isotropic epineurium with a 2mm inner diameter that surrounds a single anisotropic nerve fascicle. The depth of the nerve trunk from the surface of the subcutaneous tissue layer is 1 cm.

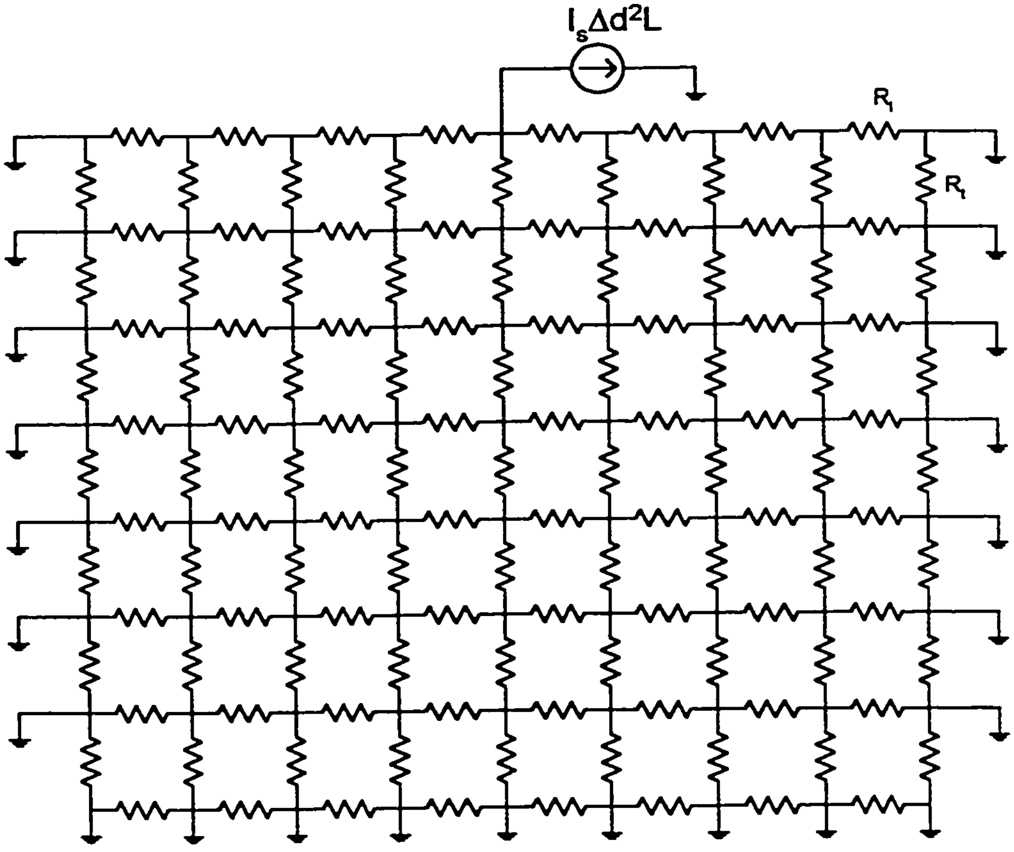

Figure 3.1.(b) The circuit shown above illustrates the finite difference simulation mesh with R_l and R_t representing the longitudinal and transverse resistances taken from the plane of the simulation domain for the tissue sample. The grid used in the simulation consists of 253×252 nodes with node spacing Δd. In a 2-D representation, the current source becomes a point source as shown scaled by L which is the length of the electrodes in the z-direction. A stimulus current amplitude of 100 mA was used in these simulation for an electrode length of L = 10 mm.

The above equation can be written in terms of the discrete voltages defined at the points of the simulation domain grid. In two dimensions, the discrete form of (3.4), with reference to Figure 3.1(b), can be written as

$$\begin{aligned}&\left[\sigma_l(V_2 - V_0) + \sigma_l(V_1 - V_0) + \sigma_t(V_3 - V_0)\right.\\&\qquad \left. + \sigma_t(V_4 - V_0)\right]L = \begin{cases} I_s \Delta d^2 L & (x_0, y_0) = (x_s, y_s) \\ 0 & (x_0, y_0) \neq (x_s, y_s) \end{cases}\end{aligned} \tag{3.5}$$

In (3.5) σ_l and σ_t represent the longitudinal and transverse conductivities in the tissue external to the nerve trunk and within the nerve fascicle. The voltages V_0, V_1, V_2, V_3 and V_4 represent the potentials associated with a computational cell as shown in Figure 3.2 [56]. Since the longitudinal and transverse spacing between the mesh nodes were chosen to be equal, the spacing is symbolically represented by Δd. The field quantities in the z-direction, as per Figure 3.1, are assumed to be uniform everywhere under the electrode in the z dimension. This simulation does not account for fringing effects associated with the boundaries of the electrode length. These should have a minimal impact on nerve excitation studies since it is assumed that the nerve is located under the middle of the electrodes in the z-direction. It should be noted that the right hand side of (3.5) is zero everywhere in the computational domain with the exception of the nodes at which the source current electrode is attached at (x_s, y_s).

All anisotropic simulations in this study assumed a transverse resistivity of 6.75 Ωm and a longitudinal resistivity of 2.4 Ωm for the tissue medium external to the nerve trunk. These resistivity values were chosen to be consistent with skeletal muscle tissue [22]. The resistivity values associated with the nerve fascicle for the transverse and longitudinal directions were 12.5 Ωm and 2.0 Ωm respectively. The epineurium resistivity was 10 Ωm and the subcutaneous tissue layer resistivity was 25.0 Ωm [57]. Electrical properties of the nerve trunk were assumed to be the same for both the anisotropic and isotropic field calculations. Again the transverse designation refers to the resistivity in the directions perpendicular to the assumed x-directed longitudinal orientation of the nerve or muscle fiber axis. For the isotropic simulations, the external tissue transverse and longitudinal resistivity were averaged to give a resistivity of 4.575 Ωm.

A spacing of Δd = 0.5 mm was chosen for the longitudinal and transverse directions as the distance between the mesh node points. When using the finite difference field simulations in conjunction with nerve excitation studies, the choice of the mesh spacing becomes an issue. Unlike a closed form potential solution where the potential is defined everywhere, the finite difference solution only defines the potential at the mesh nodes. The spacing of Nodes of Ranvier in peripheral nerve fibers is dependent on the size of the fiber as typified by the often quoted relationship [33] between the Nodes of Ranvier spacing and the fiber diameter:

$$\frac{K}{D} = 100 \tag{3.6}$$

In peripheral motor nerves, the fibers range in diameter between approximately 1 μm and 18 μm which corresponds to a spacing between the Nodes of Ranvier of 100 μm and 1.8 mm respectively [37,52]. Since ultimately, the potential at the Nodes of Ranvier for different size fibers will have to be interpolated from the values calculated at the finite difference mesh points, it is reasonable to choose a value for the mesh spacing that is in this range and is a compromise between spatial resolution and the computational effort required to represent a relatively large tissue volume by a large number of nodes.

For a 253 by 252 node simulation domain and a longitudinal and transverse spacing of 0.5 mm, the solution of the linear system of equations generated by (3.5) at the mesh nodes is best undertaken using an iterative Gauss Seidel approach. It is advantageous to accelerate the rate of convergence of the solution by modifying the iterative technique to incorporate successive over relaxation [55]. In this study, a relaxation constant of 1.9 was used. Each finite difference simulation was iterated until the change in the potential of each node was less than 100 μV.

It is advisable, in terms of storage considerations, to take advantage of the sparse nature of the admittance matrix. Solution of systems of equations of the size presented here by matrix inversion techniques is not advisable since this approach, in its most basic form, necessitates storage of the entire admittance matrix in its full form and precludes taking advantage of its inherent sparseness.

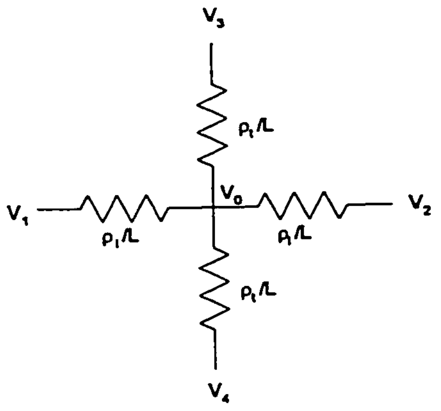

Figure 3.2 Diagram of the computational cell associated with the finite difference simulations implemented in this study where ρ_l and ρ_t are the longitudinal and transverse resistivities respectively, V_1 through V_4 are the potentials relative to V_0 as per (3.5) and L is the length along the electrode in the z-direction.

3.2 Impact of the Skeletal Muscle Tissue Isotropy Assumption

Motor nerves are routinely stimulated in electrodiagnostics to determine the conduction velocities of individual fibers and populations of fibers, or to estimate the number of motor units in a selected muscle [1,58,59]. Both surface [58] and intramuscular [1,59] electrodes are used to stimulate the nerve fibers as well as a range of stimulus pulse durations. Functional electrical stimulation (FES) also employs a wide variety of electrode configurations and stimulation protocols. One of the goals of this research was to determine what effect electrode configuration or stimulus waveform has on the selective stimulation of populations of nerve fibers with different diameters. To gain a theoretical understanding of these effects and guide the design of in vivo experiments, simulation studies can be performed using sufficiently accurate models of nerve fiber populations and the surrounding biological tissues.

The approach that has been adopted by several investigators is to assume that the surrounding tissue in the nerve excitation simulations is isotropic, homogeneous and infinite or semi-infinite [31,32,41,60]. These assumptions lead to a simple closed form expression for the potential that can be derived from the elemental form of Ohm's Law.

$$V(x,y)=\frac{I_{ext}\rho}{4\pi\sqrt{(x-x_o)^2+(y-y_o)^2}} \tag{3.7}$$

Although in general the relationship in (3.7) can be extended to three dimensions, a two dimensional potential profile can be generated where I_{ext} is the magnitude of the injected current and ρ is the tissue resistivity. The variables x and y represent the longitudinal and transverse distance from the monopolar current electrode that is located at x_o and y_o. Implicit in the form of (3.7) is that the point current source lies in the same plane as the axon.

The fact that tissue can be anisotropic has been known for some time [61-63]. Some of the earlier papers that reported anisotropic tissue conductivity focused on pulse measurements [62]. More recently, investigators have made broad spectrum measurements of anisotropic conductivity using swept frequency sinusoidal excitation current sources as well as current pulse transient techniques [22,23]. It has been demonstrated that considerable variation exists in the tissue conductivity, as a function of excitation frequency [22]. The conductivity anisotropy in tissue such as skeletal muscle has been documented experimentally and theoretical models have been proposed based on a simplified structural geometry of the muscle fibers and their electrical properties [26].

There have been many volume conduction models presented in the literature that have accounted for the anisotropy associated with different tissue structures. Plonsey demonstrated a coordinate transformation technique that is useful for modeling anisotropy in idealized volume conductors [64]. Altman went further by investigating nerve fiber threshold current requirements in an idealized, infinite homogeneous and isotropic volume conductor given an anisotropic nerve fascicle [65]. Veltink and his colleagues used anisotropic volume conduction models to study extra-neural ring and intrafascicular electrode recruitment characteristics [57,66]. Struijk *et al.* have also used anisotropic volume conduction models to study spinal cord stimulation mechanisms [67].

From a computation perspective, there are many options to choose from when calculating the potential distribution in a volume conductor. In the case of symmetric geometries with idealized inhomogeneous structures, some investigators have opted to develop closed form solutions [66]. In situations with more complicated geometries, various numerical techniques, such as the finite difference approach, have proved useful [57,67].

The effect of the isotropy assumption was investigated by undertaking finite difference simulations of the potential profile that results from point source surface electrode current stimulation in an anisotropic and inhomogeneous tissue environment. These simulations can be easily extended to point source intramuscular stimulation. Finite difference simulations have been carried out that explicitly compare an anisotropic and isotropic exterior tissue environment outside the nerve trunk using realistic conductivity values to a purely isotropic exterior tissue environment, where the parallel and transverse conductivities from the anisotropic case have been averaged. Finite difference simulations of the potential profile for different stimulus electrode configurations and geometries were carried out and the impact of the isotropy assumption for each of these was assessed.

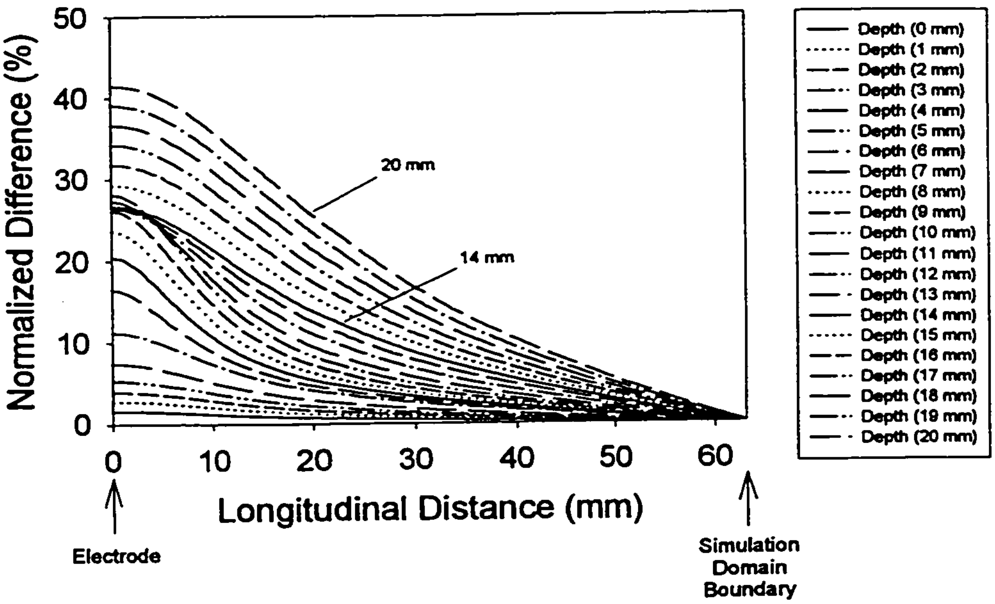

Figure 3.3 Relative potential difference profiles between the anisotropic and isotropic tissue simulations with a monopolar electrode configuration. Each curve is the potential difference at a specific depth (distance in the y-direction between the point of interest and the surface electrode). Due to symmetry, the graph shows only half of the simulation domain.

The principal goal of this study was to quantitatively compare the difference in potential solutions in tissue under the assumptions of anisotropy and isotropy for different electrode configurations and geometries. Simulations were performed for both monopolar and bipolar stimulating electrode configurations and potential fields calculated at different depths. The absolute relative errors resulting from the assumption of isotropy of the tissue external to the nerve trunk were calculated using (3.8). In this normalized difference expression, V_d represents the relative difference in potential between the anisotropic and isotropic cases as a function of the longitudinal distance from the middle of the simulation domain represented by x. The variables V_a and V_i represent the anisotropic and isotropic potentials respectively as functions of x, and the normalizing factor is the maximum anisotropic field calculated for each depth. Figure 3.3 is a plot of V_d at different transverse tissue depths for a monopolar stimulating electrode configuration.

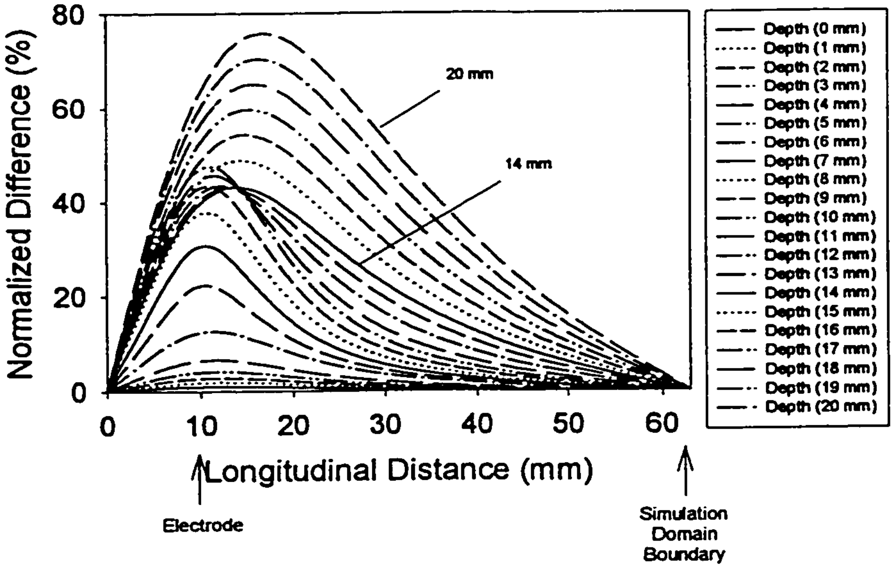

Figure 3.4 Relative potential difference profiles between the anisotropic and isotropic tissue simulations with a bipolar electrode spacing of 20 mm. The origin indicates the midpoint between the two electrodes. Each curve is the potential difference at a specific depth or increasing distance in the y-direction between the point of interest and the surface electrodes. Due to symmetry, the graph shows only half of the simulation domain.

$$V_d = \frac{|V_a(x) - V_i(x)|}{\max[|V_a(x)|]} * 100 \qquad (\%) \qquad (3.8)$$

In general the anisotropic field is less than the isotropic especially directly under the electrode. The relative difference is minimal for short transverse depths in the tissue under the electrode and increases from a maximum of approximately 2% at the electrode to a maximum of approximately 42% at a transverse depth of 20 mm. As expected, the normalized difference falls off with increasing horizontal distance, because of the rapidly decreasing anisotropic and isotropic fields at greater distances from the electrode.

In addition to investigating the error associated with the tissue isotropy assumption with monopolar stimulating electrodes, simulations were also undertaken to investigate the error associated with other electrode configurations. It should be noted that from 0 to 4 mm depth the normalized difference increases slowly reflecting the smaller field differences in the isotropic subcutaneous layer. From 5 to 10 mm the differences increase more quickly due to the anisotropic muscle layer, while the small decrease from 11 to 14 mm reflects the anisotropic nerve trunk common to both simulations. Bipolar electrode stimulation is commonly used in clinical nerve conduction or other studies where the axis of the electrode dipole is placed parallel to the nerve under test. The same amount of current is injected through one of the electrodes as is removed through the other. Figure 3.4 illustrates the relative potential difference profiles under the cathode electrode, calculated using (3.8), between the anisotropic and isotropic tissue conductivity cases for bipolar stimulation where the electrodes have been positioned 20 mm apart. Once again, the anisotropic potential fields are generally less than for the purely isotropic simulations and the minimum relative difference in potential is seen for small transverse depths in the tissue. As for the monopolar case, the general trend of increasing relative potential difference is observed with increasing transverse depths from the stimulating electrodes. Overall, the relative error observed in the 20 mm bipolar electrode case is worse than in the monopolar case for regions that are deeper than the subcutaneous tissue layer (5 mm) with a relative potential difference that increases from 1% at the electrodes to 76% at a depth of 20 mm from the surface. As in Figure 3.3, the maximum relative potential difference does not increase uniformly with increasing depth and, within the region of the nerve fascicle (10 - 14 mm), a small decrease in the maximal relative potential difference is observed.

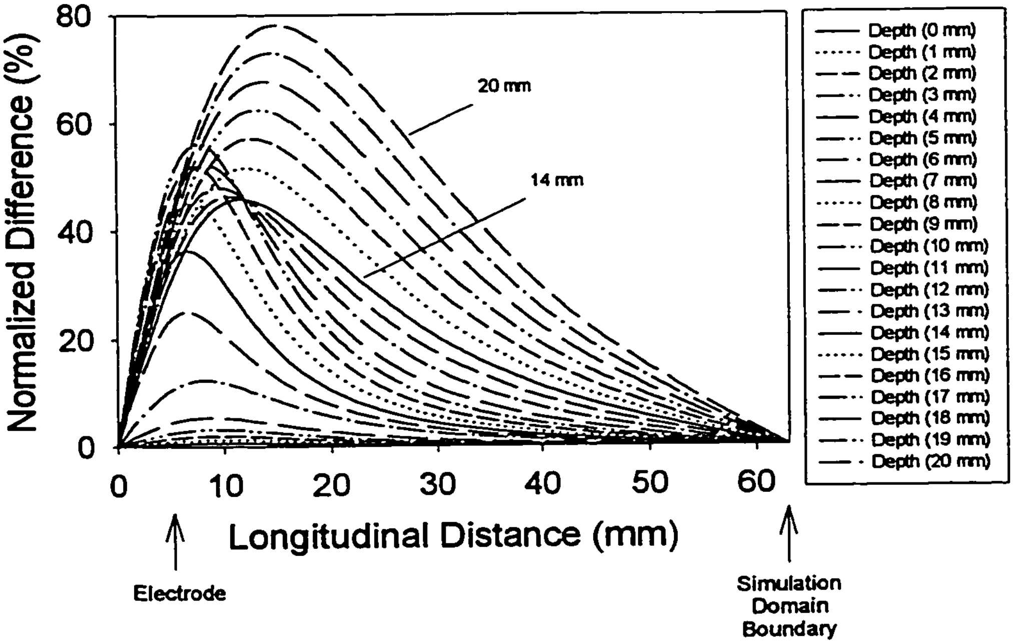

Figure 3.5 Relative potential difference profiles between the anisotropic and isotropic tissue simulations with a bipolar electrode spacing of 10 mm. Each curve is the potential difference at a specific depth (transverse distance in the y-direction between the point of interest and the surface electrodes). Due to symmetry, the graph shows only half of the simulation domain.

As the distance between the stimulating electrodes is decreased, there is an increase in the relative difference between the anisotropic and isotropic conductivity cases. The general relative difference trends observed for more closely spaced bipolar electrodes at 10 mm spacing, shown in Figure 3.5 are similar to those discussed previously for the 20 mm bipolar electrodes as well as the monopolar case. The more closely spaced electrodes exhibit peak relative potential differences from less than 1% at the electrodes to 78% at a transverse depth of 20 mm from the electrodes.

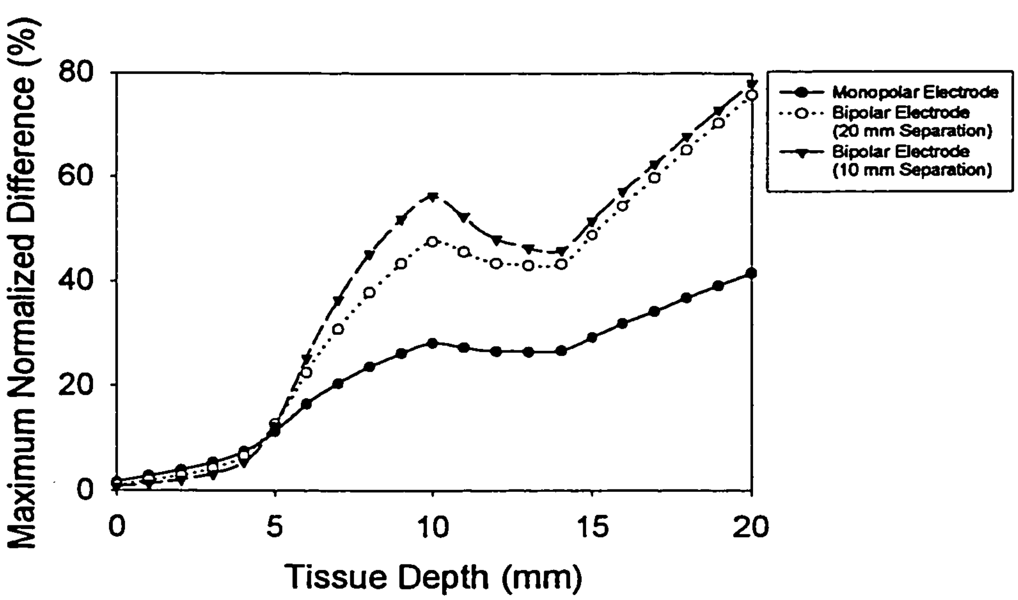

Figure 3.6 Maximum relative potential difference profiles as a function of the transverse depth from the surface of the simulated tissue domain for the three electrode configurations.

Figure 3.6 summarizes the trends observed in previous figures. In this figure, the maximum difference between the anisotropic and isotropic conductivity cases observed as a function of the transverse depth in the tissue have been plotted. This graph reinforces the fact that for depths greater than the subcutaneous tissue layer, the overall largest relative potential difference between the isotropic and anisotropic cases is observed in the bipolar electrode case with the smallest electrode separation. The monopolar case exhibits the lowest overall error of the electrode configurations studied. This order is reversed for depths within the subcutaneous tissue layer. The simulation data suggests that for short transverse depths between the point of interest and the electrode, the maximum difference between the anisotropic case and the isotropic case is comparable for all electrode configurations studied. Figure 3.6 also demonstrates the decreasing relative errors from 10 to 14 mm within the region of the nerve trunk.

3.2.1 Effect of Anisotropy on the Simulated Potential Profiles

A significant potential drop is observed across the relatively highly resistive isotropic subcutaneous tissue layer. A relatively small maximal relative potential difference is observed between the anisotropic and the isotropic potential distributions within the surface subcutaneous tissue layer. The reason for this phenomenon is that the field is similar within these regions for both cases irrespective of electrode geometry. A significant increase in the observed relative potential difference is demonstrated at greater depths where the differences between the isotropic and the anisotropic cases have greater impact on the field profiles. The simulation results also demonstrate that there is a significant change in calculated relative potential difference between the anisotropic and isotropic potential distributions for different electrode configurations. A monopolar electrode configuration exhibits a much smaller relative difference between the isotropic and anisotropic cases than a bipolar configuration at depths greater than the thickness of the subcutaneous tissue layer. There is a marginal, however not insignificant, increase in the relative difference between the anisotropic and the isotropic cases as the bipolar electrode dipole separation decreases.

A significant perturbation in the potential distribution local to the epineural sheath and the nerve fascicle is observed. This perturbation is due to the differences in the electrical properties of the epineural sheath and the nerve fascicle relative to the tissue external to the nerve trunk. The nerve fascicle tissue exhibits significant electrical anisotropy in the directions longitudinal and transverse to the roughly cylindrical axis of the fibers. In the case of the epineural sheath, the conductivity is isotropic and consists of loose fatty tissue with a higher conductivity than the subcutaneous tissue layer but still significantly lower than the transverse conductivity of the anisotropic tissue external to the nerve trunk. The perineurium was not modeled explicitly in these simulations however it has been demonstrated that for intrafascicular stimulation, the insulating properties of the perineurium are significant in the spatial localization of the stimulus which would result in greater localization of recruitment [57]. From the perspective of the relative difference calculations, the nerve fiber structure is identical in both the anisotropic and the isotropic simulations and consequently a small decrease in the relative potential difference is observed for depths associated with the nerve trunk region for all electrode configurations.

From the potential simulation results, it is evident that there is a minimum relative potential difference associated with making the isotropic approximation for the tissue external to the nerve trunk. If an isotropic assumption is made in calculating the resultant potential distribution from an excitation current electrode, then the relative error in the potential is minimal provided that the transverse depth between the point of interest and the electrode is within the depth associated with the subcutaneous tissue layer. As the transverse depth between the electrode and the point of interest is increased, the maximum relative potential difference associated with the isotropic approximation increases. This result is intuitively satisfying when the potential profile for the isotropic case is considered in comparison with the anisotropic case. In the isotropic situation, the impedance seen by the injected current is the same in all directions, however under anisotropic conditions this is not the case. Under anisotropic conditions, a greater drop in the potential in the transverse direction would be expected for the same depth as compared to the isotropic situation. The reason for this phenomenon is that the current is subjected to a much higher impedance in the anisotropic situation relative to the y-direction. It is not surprising therefore that at greater and greater depths in the tissue, a larger and larger relative difference is observed between the isotropic and the anisotropic potential.

The overall observed relative potential difference is worse for bipolar electrodes with short inter-electrode spacing and decreases as the electrode spacing increases for depths in excess of the thickness of the subcutaneous tissue layer. The monopolar electrode, which may be viewed as a limiting case of two bipolar electrodes at an infinite distance apart, exhibits the least overall relative potential difference. As the two bipolar electrodes are placed nearer to each other, there is a greater interaction between the fields generated from the positive current electrode and the negative current electrode and larger discrepancies are observed in the calculated potential distribution between the two cases. It is not unexpected that the field interaction is different under anisotropic conditions compared to isotropic conditions since more of the current flux would be confined to the regions near the surface of the tissue in the anisotropic case.

Chapter 4: The Theoretical Basis of the Nerve Fiber Excitation Simulations

In this chapter, the theoretical basis behind the nerve fiber excitation simulations are discussed. This explanation includes a description of the relationship between the finite difference field simulations that were described in the previous chapter and the nerve fiber excitation simulations that are discussed in this chapter. The nodal equation technique and the superposition technique that were used to solve for the transmembrane potential of the nerve fiber are described. A discussion of the effects of variable electrode orientation is undertaken with emphasis on why it is theoretically easier to excite nerves when the electrode dipole is oriented parallel to the direction of the nerve as opposed to a perpendicular orientation. The chapter concludes with a presentation of the simulation results demonstrating the effect on recruitment patterns for a population of nerve fibers that are stimulated with current pulses of variable width.

4.1 Nerve Fiber Excitation Simulations

To simulate the recruitment patterns of nerve fibers, the potential distribution in the anisotropic tissue due to the stimulus current must first be determined. In previous studies, the technique used to calculate the potential distribution in the tissue medium in which the simulated nerve fibers exist assumed a homogeneous, isotropic and infinite tissue medium as per (3.7). The potential distribution presented here has been calculated using a finite difference technique as outlined in the previous chapter. Once the potential distribution is known, this information can be used in conjunction with cable models of the nerve fiber to determine whether the fiber has been excited. The cable models used to simulate the electrical properties of the nerve fiber were discussed in Chapter 2.

It should be emphasized that there are several assumptions inherent to this simulation approach. The first of these assumptions is that excitation of a nerve fiber has no effect on the excitability of other nerve fibers or on the electrical properties of the surrounding tissue medium. Based on empirical evidence presented by other investigators, this assumption is widely believed to be true [36]. The other assumption is that the nerve fiber model is linear over the range of transmembrane potentials below the threshold potential. This assumption is also often used in the literature in conjunction with nerve excitation simulations. More realistic non-linear simulations result in the added expense of a significant increase in computation time for a relatively marginal gain in accuracy [29,47].

As was outlined in Chapter 2, a sequence of nerve fiber diameters are randomly generated such that the distribution of the nerve fiber diameters is consistent with anatomical observations.

A simplified axon equivalent circuit model composed purely of linear conductances described in Chapter 2 and similar to the axon model used by Sweeney *et al.* [47] was used to model the electrical characteristics of the nerve fibers. The appropriate equivalent circuit conductance parameters, based on the fiber size, were calculated for each nerve fiber in the population. The relevant electrical parameters are shown in Table 4.1.

ρ_a	Axoplasm Resistivity	1.1 (Ωm)
g_m	Membrane Conductance	304 (S/m$^{2)}$
c_m	Membrane Capacitance	0.02 (F/m^2)
l	Node of Ranvier Width	2.5 (μm)
D	Fiber Diameter	(m)
d	Axon Diameter	(m)
A	Fiber Radius	(m)
a	Axon Radius	(m)
a/A	Ratio of Axon to Fiber Radius	0.7
K	Nodes of Ranvier Spacing	100×D (m)
R_a	Equivalent Axoplasm Resistance	$(\rho_a K)/(\pi a^2)$ (Ω)
R_m	Equivalent Membrane Resistance	$(2\pi g_m al)^{-1}$ (Ω)
C_m	Equivalent Membrane Capacitance	$(2\pi c_m al)$ (F)

Table 4.1 Summary of the parameter values and formulas used to calculate the equivalent circuit component values shown in Figure 2.2.

Based upon the size of each individual fiber, the equivalent circuit components, as outlined in Chapter 2, are calculated according to (2.4), (2.5) and (2.6). Another important parameter that is calculated, based on the randomly generated diameter for each fiber, is the distance between the successive Nodes of Ranvier which is described by (3.6). Larger diameter fibers have larger inter-nodal distances. The inter-nodal distance parameter is an important link between the potential distribution calculated using the finite difference field simulation and the nerve excitation calculation. An interpolation of the potential distribution data at a given depth of the nerve fiber in the simulation domain is undertaken along the length of the nerve fiber circuit model at the positions of the Nodes of Ranvier. This interpolated vector of potentials represents the extracellular potentials that are used to calculate the change in the transmembrane potential of the nerve fiber at each node. Once the transmembrane potential change along the nerve fiber is determined, a calculation is performed to ascertain whether the transmembrane potential change at any point along the nerve fiber exceeds the pre-determined threshold value of 25 mV. If the threshold value is exceeded, the nerve fiber is assumed to have fired.

4.1.1 Calculation of the Transmembrane Potential

There are several methods that can be used to solve for the transmembrane potential along the nerve fiber equivalent circuit model. The most straightforward technique is to use nodal equations based on Kirchhoff's Current Law to write a system of linear equations which can then be solved for the nodal voltages. In Chapter 2, two nerve fiber equivalent circuit models were presented in Figures 2.1 and 2.2. The intracellularly injected current source model of Figure 2.2 is the most convenient to use from the perspective of establishing the nodal circuit equations as per (4.1) where $\boldsymbol{Y}$ is the nodal admittance matrix, $\boldsymbol{V_m}$ is the vector of the transmembrane potentials and $\boldsymbol{I_i}$ is the vector of excitation sources.

$$YV_m = I_i \tag{4.1}$$

There are several options available to solve for the nodal potential vector in (4.1). The most straightforward of these options involves an inversion of the admittance matrix $\boldsymbol{Y}$. In the software implemented to determine the nerve fiber recruitment methods, an iterative Gauss Seidel technique was used with successive over relaxation [55]. The relaxation constant selected for these simulations was 1.9 as it offered the most rapid convergence.

In addition to the above mentioned technique, an alternative method for solving for the nodal potentials was used to verify the accuracy of the nodal admittance matrix technique specified above. This technique is based on the superposition property that is an inherent feature of linear circuits [68]. The idea behind the superposition technique is to excite the circuit with each source individually with all the other sources turned off. Once the nodal potentials are calculated for each excitation source they are summed to obtain the potentials at the nodes that results from the excitation from all the sources. The intracellularly injected equivalent circuit model was selected for this approach.

$$V_m(k) = \sum_{n=1}^{s} \Psi_n(k) I_i(n) \tag{4.2}$$

Stated mathematically, the superposition approach can be written as shown in (4.2) where $V_m(k)$ is the resultant transmembrane potential at node k, $\Psi_n(k)$ is the induced transmembrane potential at node k per unit of current injected at node n and $I_i(n)$ is the current injected at node n.

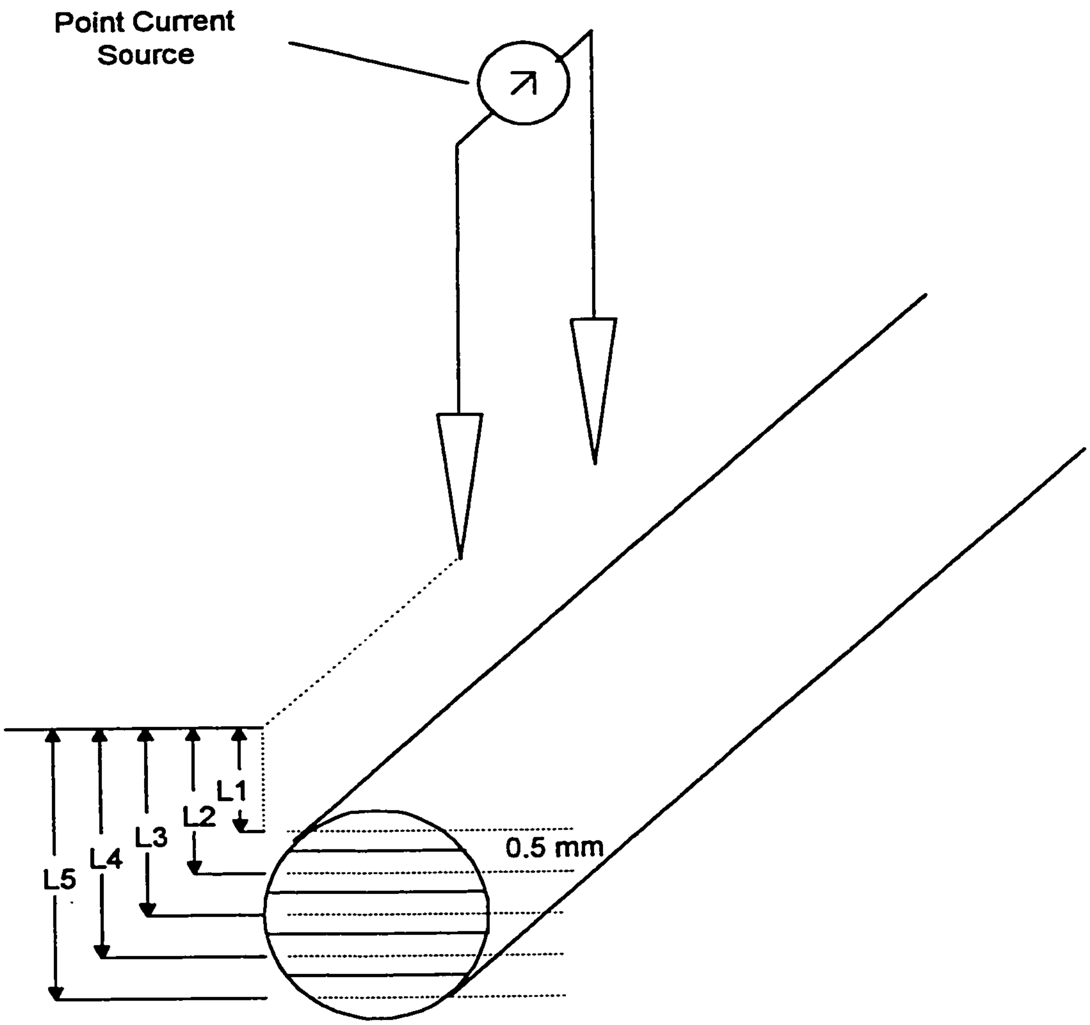

Figure 4.1 Conceptual drawing of the simulation domain for the nerve excitation studies presented in this work. The distances L1, L2, L3, L4 and L5 represent the positions of increasing vertical distance or depth from the electrode at which the randomly generated groups of nerve fibers are located.

For the variable stimulus current pulse width simulations, a time dependent or transient algorithm had to be implemented [69]. The procedure for formulating the nodal admittance matrix was essentially the same as used in the steady state DC simulations however, in this case, it is convenient to formulate the network equations by separating the capacitive and conductive components of the admittance matrix into two separate matrices as per the following equation.

$$C_A \dot{V}_m = -G_A V_m + I_i \tag{4.3}$$

In equation (4.3), C_A is the capacitive component of the admittance matrix which is itself a matrix and G_A is the conductive component of the admittance matrix which is also a matrix. The transmembrane potential vector is represented by V_m and the intracellularly injected current vector is represented by I_i.

In the custom designed software package for the nerve excitation simulation, an implicit Euler technique was used to numerically integrate (4.3) as per (4.4) where h is the time step and u represents the time step index.

$$V_{m_{u+1}} = V_{m_u} + h\dot{V}_{m_{u+1}} \tag{4.4}$$

Upon substitution and rearrangement using (4.3), equation (4.4) can be re-written in a more convenient form as shown in (4.5).

$$V_{m_{u+1}} = \left[\frac{1}{h}C_A + G_A\right]^{-1}\left[\frac{1}{h}C_A V_{m_u} + I_{i_{u+1}}\right] \tag{4.5}$$

Equation (4.5) is convenient from a computation perspective because, unless the time step changes, the first term can be evaluated once and used repeatedly. In the time domain simulations, V_m represents the transmembrane potential where u is the time step index. When the transmembrane potential change at any point reaches the assumed threshold potential of 25 mV, the axon is categorized by the simulation as having been recruited.

4.2 Impact of the Anisotropy Assumption on Nerve Fiber Recruitment Simulations

It has been illustrated in Chapter 3 that there are differences in the calculated potential between the isotropic and anisotropic conductivity cases. The question then arises as to whether these differences are significant enough to alter the firing predictions made by axon excitation simulations. For each of the simulations presented below, a sequence of fifty nerve fiber diameters were generated in accordance with the technique and distribution discussed in Chapter 2. The randomly generated fiber diameters were divided into five groups of ten and assigned different depths in the potential field simulation domain.

Table 2 shows the average recruited fiber diameter for each electrode configuration for anisotropic and isotropic tissue mediums. For the most part, the trends observed in the nerve fiber recruitment studies for the different stimulus electrode configurations can be qualitatively explained on the basis of the potentials calculated from the field simulation studies. The activation function, as described by Rattay [31], is a useful tool for qualitatively estimating relative excitability. However, it does not account for all the phenomenon that contribute to determining the relative recruitment potential of a nerve fiber [70]. Altman and Plonsey demonstrated that for large depths between the nerve fiber and the stimulus electrode, the activation function for myelinated fibers is independent of the fiber diameter. The diameter dependence can be compensated for by multiplying by an appropriate scaling factor. However, even the scaled activation function can only be relied on for a qualitative estimate of the relative recruitment potential of a fiber. The fundamental reason for this is that the activation function is an alternate representation of the extracellular potential and does not account for potential changes internal to the fiber that result from stimulus current flow across the fiber membrane. Altman and Plonsey emphasize that the forcing function is an integral component of the solution to the differential equation for the spatially varying transmembrane potential. However, excitation depends on this spatially varying transmembrane potential and not strictly on the activation function. Other effects such as conductivity, the parameters associated with the membrane and the geometry influence the overall spatially varying transmembrane potential.

Plots of the relative potential presented earlier demonstrated that the error associated with the isotropic assumption is consistently worst for bipolar electrodes with smaller inter-electrode spacing and decreases as the spacing increases. The monopolar configuration, which may be viewed as the limiting case of a bipolar electrode pair with an infinite inter-electrode spacing, exhibits the smallest difference. It should be noted that the absolute difference in the calculated potentials between the anisotropic and isotropic cases is largest for the monopolar electrode configuration and smallest for bipolar electrodes with a small inter-electrode spacing. This trend is consistent with differences observed in the average recruited fiber diameter for the different electrode configurations investigated.

Although the absolute potential differences for the examples presented earlier are consistent with the average nerve fiber recruitment pattern changes observed between the anisotropic and isotropic cases, this trend is not always observed. The reason for these discrepancies is that the range of different stimulus currents from the electrodes required to drive nerve fibers of different sizes to excitation increases with decreasing fiber diameter. If a given distribution of nerve fiber diameters is plotted in terms of the stimulus current required to reach excitation, the majority of fibers are grouped at relatively low stimulus current amplitudes. A relatively large change in the stimulus potential can therefore lead to a smaller change in the average recruited fiber diameter than a smaller change.

An investigation of the activation functions associated with the three different stimulus electrode configurations at a depth of 11.5 mm demonstrate that the bipolar electrode configuration with the largest inter-electrode spacing exhibits the largest magnitude activation function. The activation function associated with the monopolar electrode configuration is intermediate in amplitude and the bipolar electrode configuration with 10 mm separation has the smallest amplitude activation function. For the isotropic case, the above trend is consistent with the recruitment pattern associated with the average recruited fiber diameter. The results associated with the anisotropic case for the monopolar electrode and the bipolar electrodes with 10 mm separation are interchanged from what would be expected based on an examination of the activation functions. A possible reason for this inconsistency is that the activation function is largely independent of fiber diameter when the depth between the fibers and the stimulus electrodes is relatively large [70]. Since the recruitment patterns of a population of nerve fibers is being investigated, it is not possible to scale the activation function with a fixed nerve fiber diameter to re-introduce the nerve fiber diameter dependence. The effects associated with variable depth of the nerve fibers in these simulations could also be a contributing factor to the discrepancy observed in the anisotropic case. Unlike many simulations presented in the literature, our study does not assume that there is a Node of Ranvier lying directly under the stimulating electrode [41,70]. Imposing a fixed position for the Nodes of Ranvier, based on stimulus electrode location, for all the nerve fibers in the simulated population would be unrealistic. The potential at a specific Node of Ranvier nearest in horizontal distance to the stimulus electrode will therefore not necessarily be maximal and may alter the recruitment patterns from what would be intuitively expected based on an examination of the potential and activation function amplitudes.

Depth	Monopolar Electrode	Bipolar Electrodes (10 mm)	Bipolar Electrodes (20 mm)
Isotropic	12.81 μm	12.88 μm	12.65 μm
Aniso-tropic	13.74 μm	13.53 μm	13.45 μm

Table 4.2 Simulated data of the firing patterns of the same population of nerve fibers in isotropic and anisotropic medium. A total of 50 randomly generated nerve fiber diameters were divided arbitrarily into 5 groups of 10. These groups were assigned increasing depths in the virtual nerve trunk in 0.5 mm increments between 11.0 mm and 13.0 mm within the inhomogeneous tissue simulation domain illustrated in Figure 3.1(a). The stimulus current pulse amplitude used was 10 A/m. The isotropic and anisotropic table entries show the average recruited fiber diameter for each electrode configuration.

Cathodal blocking phenomenon was not considered in these simulations. In the bipolar electrode case, anodal stimulation would be possible but excitation from cathodal stimulation would occur at lower current levels before anodal stimulation since the electrode currents are symmetric. Implicit in these simulations is the assumption that currents generated from nerve fiber excitation do not appreciably perturb the stimulating field. It should be noted that this assumption has been used by other investigators in nerve excitation simulations [66] and is a reasonable approximation [36]. However, some effect on the stimulating field associated with the synchronous firing of many fibers, as would occur during stimulation, has been suggested [71].

4.3 The Effect of Electrode Orientation on Nerve Fiber Recruitment

4.3.1 Impact of Electrode Distance

There are three principal factors that contribute to the variations in stimulus response that are observed with different electrode dipole orientations. The first of these factors concerns positioning of the stimulus electrode dipole. Differences in electrode positioning will result in differences in the distances between the stimulus electrodes and the nerve fibers. A finite difference simulation study, shown in Figure 4.2, demonstrates the differences in the potential distribution observed for different distances between stimulus source and a specific depth in a homogeneous isotropic and anisotropic skeletal muscle tissue medium. Variations in the potential distribution with increasing distance between the stimulus source and the nerve fibers will result in variations in nerve fiber recruitment patterns. The other two factors leading to stimulus response variability are less easily understood and are discussed below in detail.

4.3.2 Impact of Tissue Anisotropy

Figure 4.2 compares the potential distribution from a 1 A/m bipolar current source in an isotropic medium and an anisotropic medium. In this example, the anisotropic medium conductivity values were chosen to be consistent with the reported values for skeletal muscle tissue. The isotropic medium conductivity value was taken as the average of the high conductivity and low conductivity values used in the anisotropic case. Since the current sources that drive the specific nerve fiber towards excitation are dependent upon the extracellular potentials, a different potential in the isotropic situation will lead to different recruitment patterns when compared to recruitment in the anisotropic case. During routine clinical stimulation of deeper motor nerves, it is unlikely that the stimulus electrode dipole will be placed exactly parallel or exactly perpendicular to the direction of the muscle fibers and the actual conductivity seen by the stimulus current will be a combination of the conductivity seen in the parallel and the transverse directions.

In addition to the anisotropy associated with a single type of tissue, such as skeletal muscle, the presence of different types of tissue under the stimulating electrodes can also contribute to the anisotropy seen by the stimulus current. Stimulation of the median nerve at the anterior aspect of the wrist is a good example of an inhomogeneous region beneath the electrodes where there are many different types of tissues present including nervous tissue, tendons and blood vessels. The electrically inhomogeneous nature of these different tissue types, combined with the fact that these tissues will also likely exhibit anisotropy, compounds the electrode orientation problem.

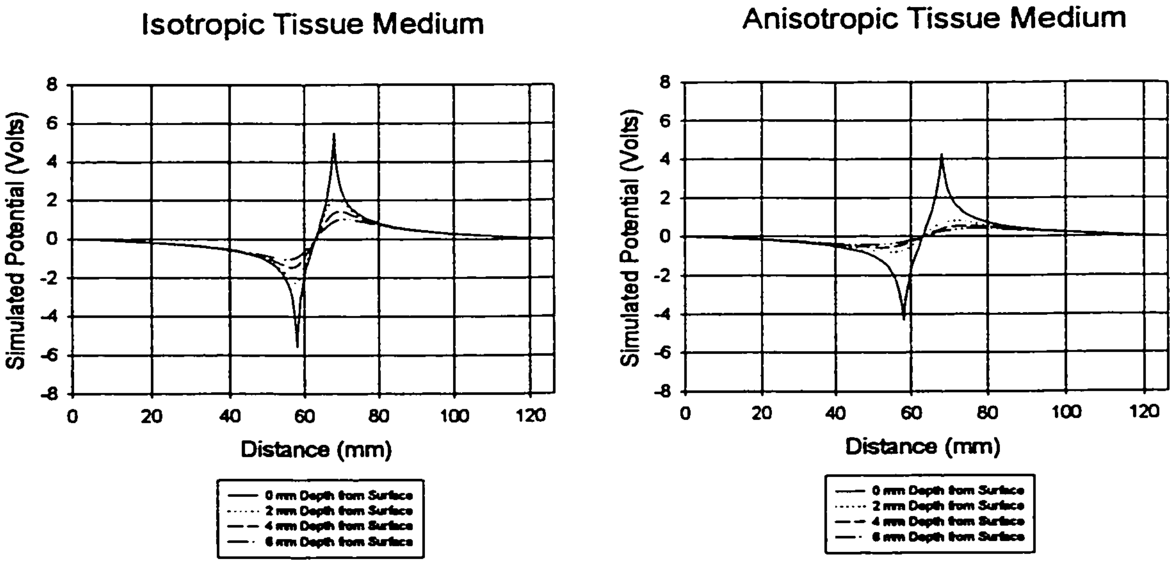

Figure 4.2 Simulated horizontal potential distribution in an isotropic and an anisotropic tissue medium resulting from a 1 A/m bipolar current stimulus (10 mm spacing). The tissue conductivities used in the anisotropic simulation are σ_t = 0.148 S/m for the direction transverse to the muscle fiber orientation and σ_l = 0.417 S/m for the direction parallel to the muscle fibers. In the isotropic simulation, the average value of σ_t and σ_l was used for both the transverse and parallel directions.

4.3.3 Impact of Bipolar Electrode Orientation

From a theoretical perspective, excitation of a cylindrical unmyelinated axon in a uniform electric field that is oriented perpendicular to the fiber axis is much more difficult than when the field is oriented in the direction parallel to the axis. The reason for this discrepancy in the ease of recruitment is that the transmembrane potential in the perpendicular case is proportional to the electric field with a constant of proportionality equal to the fiber diameter. In the parallel case, the proportionality constant is equal to the fiber length constant which is typically an order of magnitude larger [43,72]. As a consequence of the difference in scaling constant size, the fiber is recruited much more easily with the parallel oriented field.

Electrical current stimulation from bipolar electrodes establishes a spatially varying profile of extracellular potentials along the length of a given nerve fiber. As outlined in Chapter 2, the values of the distributed current sources that drive the nerve fiber towards excitation in the fiber model are directly proportional to the concavity, or the second derivative, of the extracellular potentials at the Nodes of Ranvier along the nerve fiber as per (4.6) where G_c is the axoplasm conductance between the Nodes of Ranvier, I_i is the source magnitude at the nth Node of Ranvier, V_e is the extracellular potential and n is the index for a specific Node of Ranvier.

$$I_i(n) = G_c\{V_e(n-1) - 2V_e(n) + V_e(n+1)\} \tag{4.6}$$

In the case where the stimulating electrodes are oriented parallel to the length of the nerve fibers, as shown in Figure 4.3(b), there will be a spatial variation of the extracellular potential at the Nodes of Ranvier along the length of the nerve fiber. As a consequence, the source terms $I_i(n)$ will be non-zero provided that the concavity associated with the spatial variation of the extracellular potentials along the nerve fiber is non-zero. Consider a homogeneous medium where the stimulus electrode dipole is oriented perpendicular to the length of the nerve fibers as shown in Figure 4.3(a). In this situation, the length of the nerve fibers under the stimulus electrodes will all be at the same potential. This fact implies that the source terms $I_i(n)$ under the electrodes will be zero, according to (4.6), and that there will be no current driving the fiber in this region. The above analysis is theoretical in that fringing effects at the end of the electrodes are neglected and a uniform current density everywhere along the length of the electrode is assumed.

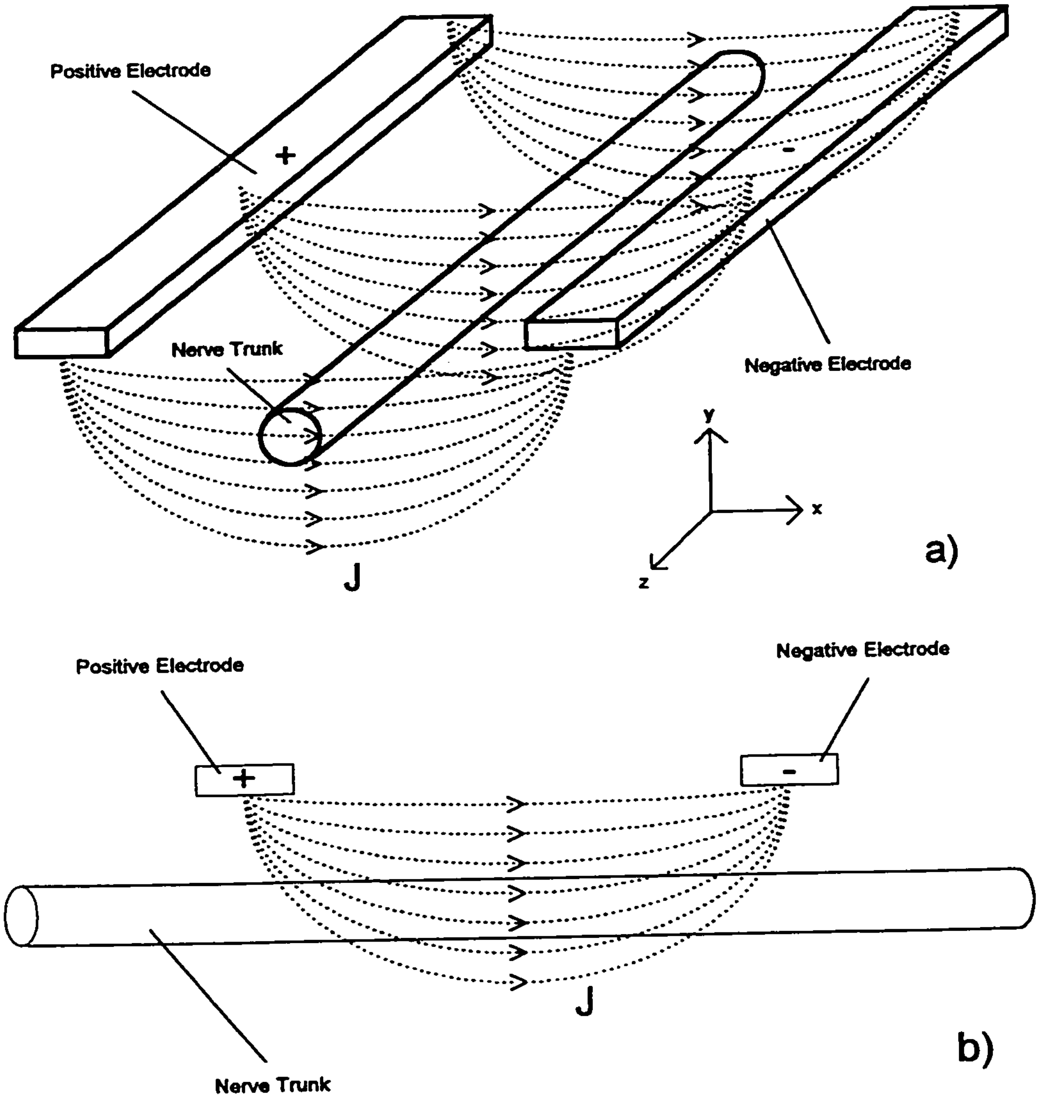

Figure 4.3 Idealized drawing of the stimulus electrode dipole perpendicular and parallel to the length of the nerve trunk. The drawing illustrates, in an idealized fashion, the lines of current flux emanating from the electrodes.

The above two cases represent the extreme situations. In practice, the electrodes will be oriented at some angle to the length of the nerve fibers and as a consequence, there will be a component of the stimulus current flux that is perpendicular to the fiber length and a component that is parallel.

4.4 The Effect of Stimulus Current Pulse Width on Nerve Fiber Recruitment

The average diameter of recruited nerve fibers, as a function of stimulus pulse width, is plotted in Figure 4.4. Three separate plots are shown on the graph for increasing distance between the simulated nerve trunk and the stimulus electrodes.

Figure 4.4 shows that the average recruited fiber diameter decreases with increasing pulse width. This result is consistent with expectations since larger diameter nerve fibers are recruited more easily than smaller diameter fibers. Stimulus strength versus stimulus duration curves also demonstrate this effect since a given fiber's stimulus threshold decreases with increasing pulse width or energy. Hence smaller, higher threshold fibers are increasingly recruited as pulse energy increases. Figure 4.4 also shows that the overall average recruited fiber diameter increased as the depth or the distance between the stimulus source and the nerve fibers increased. This result is also consistent with expectations, since as the distance between the nerve fibers and the stimulus source increases, only somewhat larger lower threshold nerve fibers would be recruited.

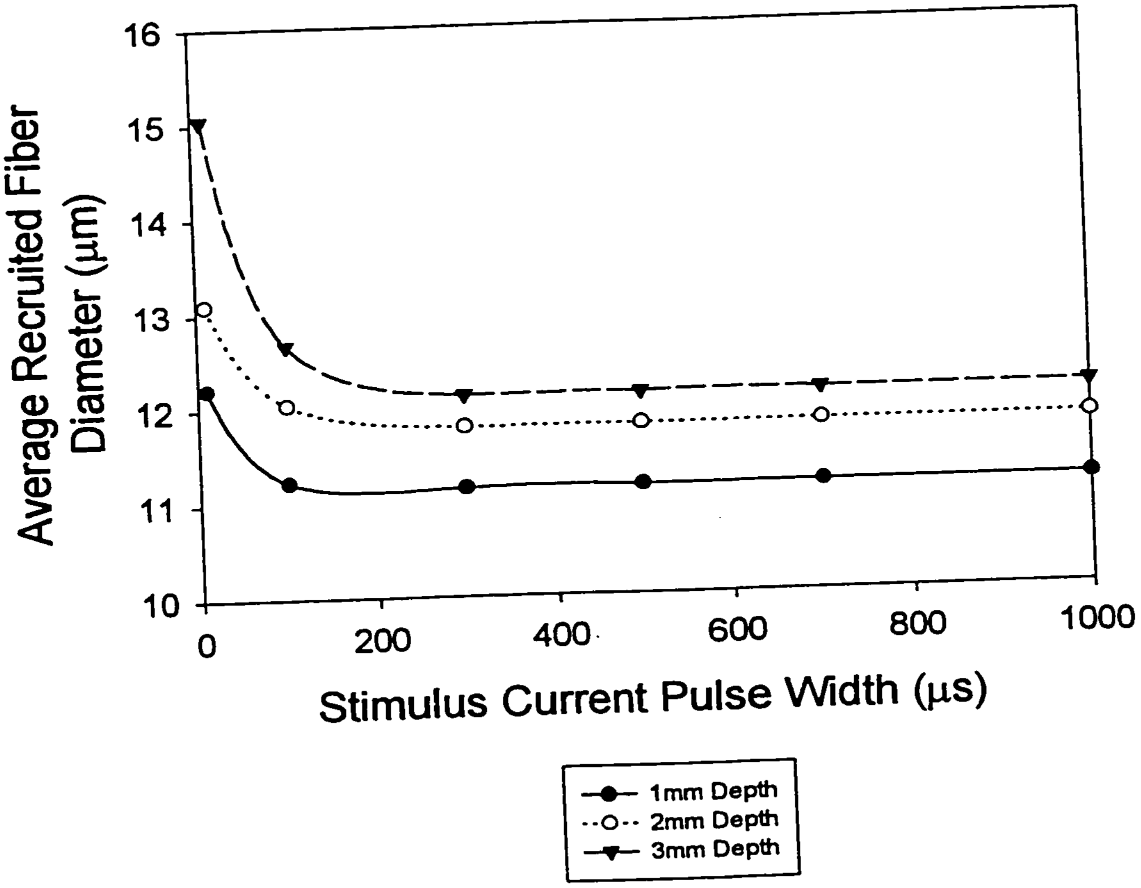

Figure 4.4 Plot of simulations of average recruited nerve fiber diameter under conditions of variable stimulus current pulse width. These simulations were carried out in a homogeneous anisotropic skeletal muscle tissue medium with conductivity values as outlined in Chapter 3. The stimulus current pulse amplitude used was 1 A/m with a monopolar stimulus electrode configuration. A population of sixty fibers was divided into six groups of ten with each group assigned an increasing depth, in 0.5 mm increments, in the tissue medium starting at the depth shown in the legend above.

Figure 4.5 shows the average diameter of recruited nerve fibers, normalized to the average calculated for a 10 μs pulse. This figure demonstrates the relative effects of changing pulse width. As can be seen, the relative effects increase with increasing nerve trunk distance from the electrode. This result is consistent with previously reported single fiber excitation studies [2].

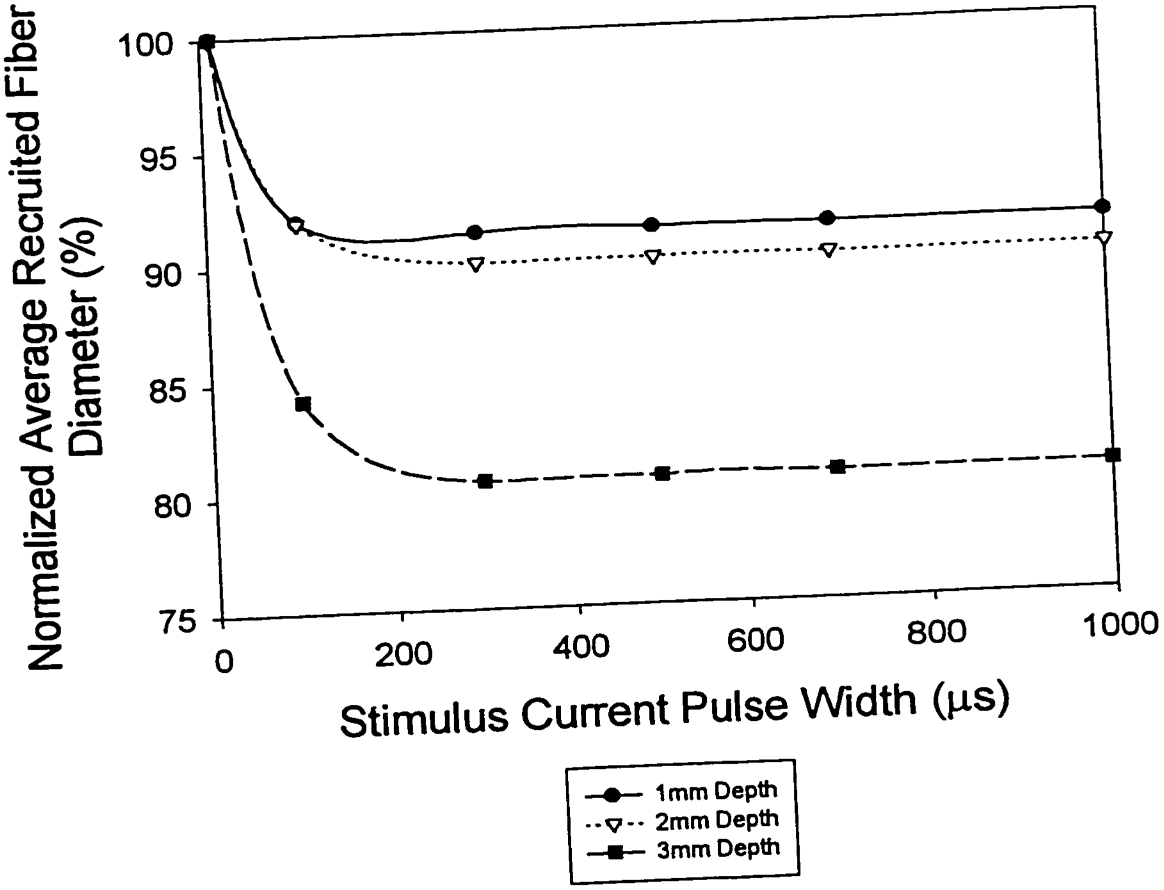

Figure 4.5 Plot of simulations of average recruited nerve fiber diameter under conditions of variable stimulus current pulse width. Each curve is normalized to the average recruited fiber diameter for a 10 μs pulse. These simulations were carried out in a homogeneous anisotropic skeletal muscle tissue medium with conductivity values as outlined in Chapter 3. The stimulus current pulse amplitude used was 1 A/m with a monopolar stimulus electrode configuration. A population of sixty fibers was divided into six groups of ten with each group assigned an increasing depth, in 0.5 mm increments, in the tissue medium starting at the depth shown in the legend above.

There was also an increase in the absolute range of the recruited fibers as the simulated pulse width is increased from 10 μs to 1 ms. This result implies that for wider stimulus pulse widths, the average recruited fiber diameter decreases and the overall population of recruited fibers increases as well as more fibers of different sizes are excited to threshold.

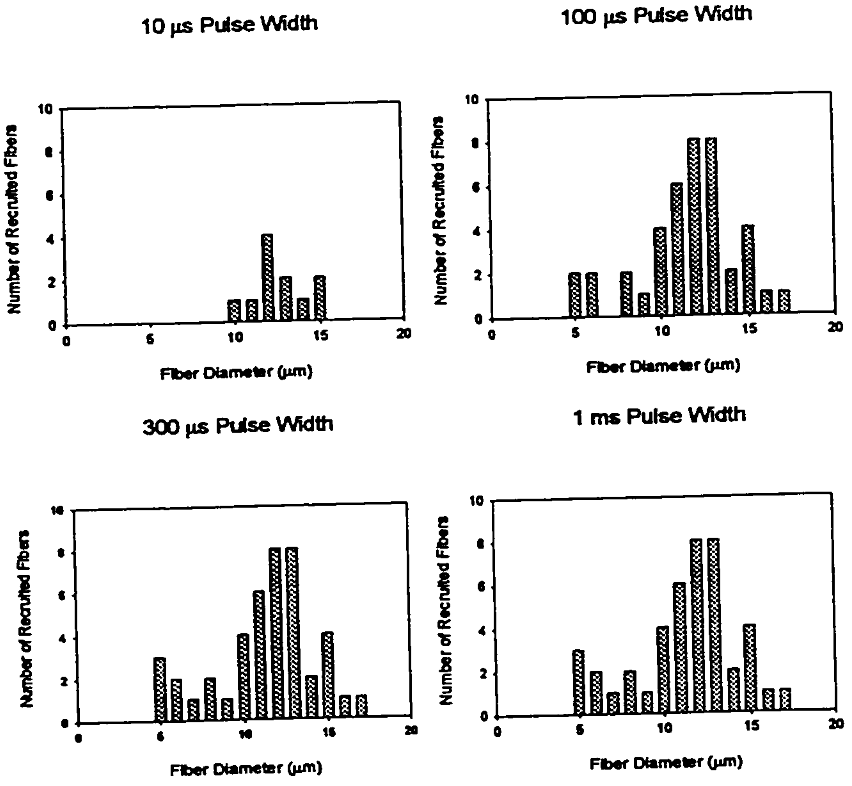

Figure 4.6 Histograms of the recruitment order of nerve fibers in the 2 mm electrode fiber group spacing simulations. As can be seen from the histograms, the distribution or recruited nerve fibers remains the same for pulse widths between 300 μs and 1 ms. These simulations were carried out in a homogeneous anisotropic skeletal muscle tissue medium with conductivity values as outlined in Chapter 3. The stimulus current pulse amplitude used was 1 A/m with a monopolar stimulus electrode configuration. A population of sixty fibers was divided into six groups of ten with each group assigned an increasing depth, in 0.5 mm increments, in the tissue medium.

Figure 4.6 illustrates the increase in the absolute range of the recruited fibers as the stimulus pulse width increases from 10 μs to 1 ms. The general trend observed is a recruitment of smaller diameter fibers at increasing pulse widths. Due to the fact that the fiber population is distributed across a range of depths starting at 2 mm, some larger fibers at greater depths are recruited as the stimulus current pulse width increases.

The trends observed in the simulation study are consistent with other studies investigating the differences in stimulus current requirements to recruit a fiber under conditions of variable stimulus pulse width and distance from the excitation source. The simulations presented in this paper exhibit a small (up to 20%) decrease in the average recruited nerve fiber diameter when the stimulus pulse width is changed from 10 μs to 1000 μs. As well, the variations in average recruited nerve fiber diameter are greater when the nerve fiber is positioned farther from the stimulus electrodes in the simulated tissue domain.

Although simulation results suggest greater achievable size selectivity at increasing distance between the stimulus source and the nerve fibers, a consequence of greater distance is the necessity to use larger stimulus amplitudes to recruit more fibers when a maximal response is desired. Larger stimulus current amplitudes have the disadvantage of causing greater discomfort to the subjects due to excitation of local sensory fibers. Utilizing narrower stimulus current pulse widths also has the consequence of requiring larger stimulus current amplitudes to recruit the nerve fibers.

Chapter 5: Stimulus Electrode Orientation and the Stimulus Current Pulse Width Experiments

In this chapter, the experimental techniques used to investigate the effects of stimulus current pulse width and stimulus electrode orientation will be described. Experimental results will then be discussed in conjunction with the novel simulation results presented earlier. The experimental technique used to investigate the effects of stimulus current pulse width on nerve fiber recruitment patterns involves a novel application of motor unit number estimation. Latency data from the individual motor unit action potentials were used to generate an estimate of the efferent motor nerve fiber diameter associated with each specific motor unit. By using this experimental technique to obtain an estimate of the recruited nerve fiber diameter statistics, a quantitative comparison could be made with simulation results presented earlier. An alternative experimental method for ascertaining the effects of variable stimulus pulse width is outlined in Appendix C. A novel experiment was implemented to investigate the effects of electrode orientation on nerve fiber recruitment patterns.

5.1 Stimulus Current Pulse Width Experiments

Motor unit estimation studies of the thenar muscle on the non dominant hand were carried out on five healthy male subjects between the ages of 24 and 53 with no known neurological or neuromuscular pathologies. A commercial EMG machine (Advantage Medical) using a computer automated motor unit number estimation technique allowed for the extraction of 20 individual motor unit action potentials and their latencies from the sub-maximal M-Wave [58]. The machine features a 12 bit analog to digital converter with a sampling frequency of 4 kHz. Settings of 10 Hz and 1 kHz were used for the high pass and low pass filters respectively. This technique assumes that cancellations between individual action potentials are minimal. In each study, the median nerve was stimulated on the medial side of the upper arm, proximal to the elbow. Independent studies were carried out for three different electrode orientations on each subject.

The stigmatic electrode was made by cutting a 27 × 22 mm EKG electrode (Sentry Medical Products, Irvine California) longitudinally, and mounting the 2 halves end to end over the thenar eminence to cross the first metacarpal bone perpendicularly at the junction of its proximal and middle thirds. The reference electrode was half of another EKG electrode over the proximal phalanx of the thumb. The first stimulus electrode orientation was parallel to the length of the upper arm, the second was perpendicular and the third orientation was taken at 45°. In all cases the orientation yielding the maximal M-Wave response at the lowest stimulus current was used for the motor unit estimation studies and motor nerve fiber latency data presented below.

The motor unit estimation study for each subject was repeated for stimulus current pulse widths of 50 μs, 100 μs, 200 μs and 500 μs. For all but one subject, the available stimulus current range was sufficient to obtain the full set of twenty different motor unit waveforms at all the stimulus pulse width settings. In one subject, the built in maximal stimulus current amplitude limit of 100 mA, in the motor unit estimation study, limited the number of motor units obtainable for the 50 μs pulse width setting to five. Onset latency data for each individual motor unit were obtained from measurements of the scaled output from the EMG machine as illustrated in Figure 5.1. The straight line distance between the stimulus dipole on the upper arm and the recording site on the thenar muscle was recorded for each subject. This information was used in conjunction with the latency data to obtain an estimate of the motor nerve fiber diameter for each individual unit as per (5.1) where $\boldsymbol{D}$ is the fiber diameter, $\boldsymbol{l_M}$ is the estimated straight line distance between the stimulus and the recording electrodes and $\boldsymbol{t_d}$ is the latency associated with each individual motor unit. A constant ratio of fiber conduction velocity to fiber diameter of $\boldsymbol{k_v} = 5.0\times10^6\ \mathrm{s}^{-1}$ was used in estimating the motor nerve fiber diameter of each individual motor unit from the conduction velocity estimates [36].

$$D = \frac{l_M}{k_v t_d} \tag{5.1}$$

All of the subjects studied exhibited a decrease in average diameter of recruited nerve fibers as stimulus current pulse width increased from 50 μs to 500 μs. Figure 5.2 shows the normalized average recruited fiber diameter as a function of pulse width. Although Fig. 5.2 shows the expected negative slope, it is not as consistent as for the simulation results of Fig. 4.5. As well, the relative change in average fiber diameter is not as great, even though the nerve to electrode distance is greater than 3mm. It should however be noted that the pulse width range for the experimental study was 50 µs to 500 µs but the simulation study encompasses a pulse width range of 10 µs to 1000 µs. Experimental investigations using narrower pulse widths than 50 µs was not possible because of equipment limitations. The stimulus current amplitudes that would likely be required to recruit nerve fibers at these shorter pulse widths would be prohibitively high especially in cases where the nerves were deep.

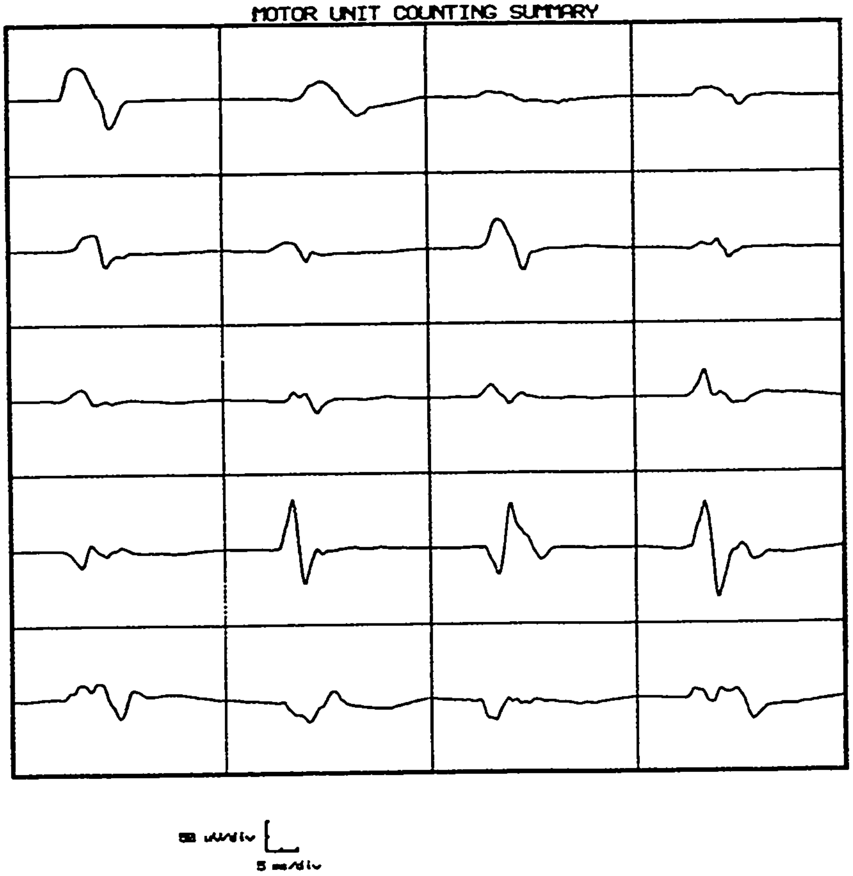

Figure 5.1 Surface motor unit action potentials recorded from the thenar muscle for 50 µs pulse width stimulation of the median nerve proximal to the elbow.

All subjects studied exhibited an increase in the absolute range of maximum versus minimum diameter nerve fibers that were recruited at some point as the stimulus current pulse width was increased. The results however do show that this range does not always consistently increase as the stimulus current pulse width increases. A maximum difference between the largest to smallest diameter fibers recruited was observed in the middle range of the stimulus current pulse widths for most subjects. Three of the five subjects that we studied exhibited an overall increased range of recruited fibers when we compared the smallest to largest diameter fiber recruited at 50 μs and 500 μs stimulus pulse widths.

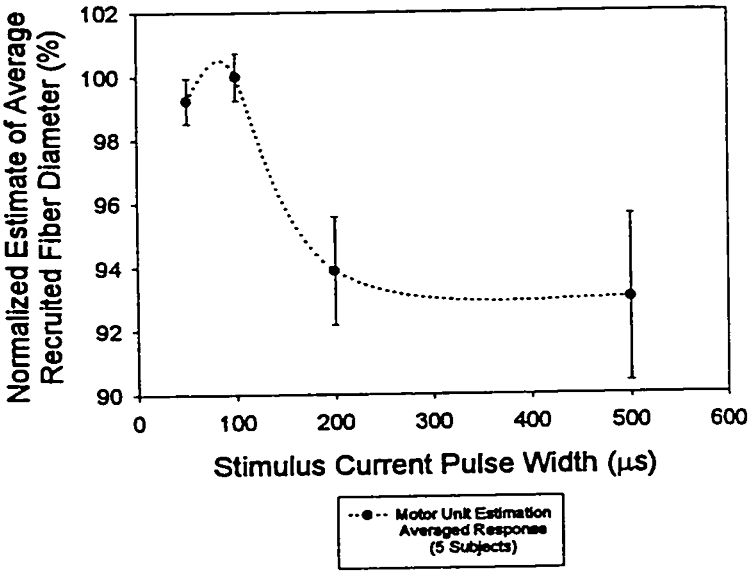

Figure 5.2 Plot of the estimate of the average recruited nerve fiber diameter as a function of stimulus current pulse width. These are the averages from data taken from five subjects where each subject's data has been normalized to the maximum average recruited fiber diameter estimate. The average nerve fiber diameter is estimated from data taken from motor unit estimation studies conducted at different stimulus current pulse widths. Standard error bars are shown for the motor unit estimation study.

5.2 Discussion of the Stimulus Current Pulse Width Experiment Results

The trends observed in the simulation study are consistent with other studies investigating the differences in stimulus current requirements to recruit a fiber under conditions of variable stimulus pulse width and distance from the excitation source. The simulations presented in Chapter 4 exhibit a small (up to 20%) decrease in the average recruited nerve fiber diameter when the stimulus pulse width is changed from 10 μs to 1000 μs. As well, the variations in average recruited nerve fiber diameter are greater when the nerve fiber is positioned farther from the stimulus electrodes in the simulated tissue domain.

The trends observed in the motor unit estimation studies that were performed on several subjects and the least squares estimation study are consistent with the simulation results, giving some validity to the simulation approach. These results suggest that the nerve fiber, and consequently motor unit size, selectivity that is achievable by varying the stimulus current pulse width within the commonly used clinical range, is not very promising. Only relatively small variations in the average recruited nerve fiber diameter of approximately 1 μm were observed in the experimental study, when the stimulus pulse width was increased from 50 μs to 500 μs. This was considerably less than the 20% change observed in Figure 4.5 at 3 mm depth in the simulation results, even though the median nerve is probably greater than 3 mm away from the surface stimulating electrode.

However, the majority of the variation observed in the simulations occurs in the range of 10 μs to 100 μs. Since the shortest pulse in the experimental studies was 50 μs because of machine limitations, the apparent difference between simulation and experimental results is not as significant, since we could not verify the 10μs to 50 μs range.

Although simulation results suggest greater achievable size selectivity at increasing distance between the stimulus source and the nerve fibers, a consequence of greater distance is the necessity to use larger stimulus amplitudes to recruit more fibers when a maximal response is desired. Larger stimulus current amplitudes have the disadvantage of causing greater discomfort to the subjects due to excitation of local sensory fibers. Utilizing narrower stimulus current pulse widths also has the consequence of requiring larger stimulus current amplitudes to recruit the nerve fibers.

The results presented here also provide evidence of the robustness of the McComas motor unit number estimation technique performed with surface stimulus pulse widths that vary across the commonly used clinical range. The results suggest that these motor unit number estimates are relatively independent of the stimulus current pulse width that is used. However, both simulation and experimental results indicate that the range of recruited fiber diameters increases with increasing pulse width. The use of pulse widths greater than 50 μs could stimulate a more representative sample of motor units. Whether this is true or not requires further investigation.

Although the estimates of nerve fiber diameter based on latency measurements from motor unit estimation studies demonstrate relatively small variations in the average recruited nerve fiber diameter, it may well be that these variations are marginally greater than demonstrated by this technique. The reason for this hypothesis is the fact that the individual fiber action potentials that sum to form the individual motor unit action potentials may be expected to exhibit a degree of temporal dispersion because of fiber endplate dispersion and different fiber distances to the recording electrode for the same motor unit. The overall effect would be a compression or masking of the observed temporal latencies in the motor unit estimates.

The theoretical prediction of the relatively small variation in motor nerve fiber recruitment patterns coupled with consistent experimental evidence suggests that there is little potential for achieving significant motor nerve fiber recruitment selectivity by varying the stimulus pulse width over the clinically useful range of 50 μs to 500 μs when surface stimulation is used. Our results also suggest that for motor unit number estimation with surface stimulation, the sample of nerve fibers recruited at one electrode location cannot be significantly changed by varying the stimulus current pulse width over the clinically used range. However there is some evidence that a wider range of fiber diameters is recruited at longer pulse widths.

Another important issue that must be considered is the reproducibility of the estimates obtained from individual subjects. This issue has been partially addressed by Galea *et al.* [58]. They reported a 22% overall coefficient of variation, for the normalized results from the 121 muscles studied.

5.3 Stimulus Electrode Orientation Experiments

5.3.1 Experimental Protocol

In order to investigate the effects of electrode orientation on stimulus response, the median nerve was stimulated at a site on the medial side of the left upper arm, proximal to the elbow on five healthy male subjects. A series of test stimuli were applied at varying angles from approximately forty-five degrees to parallel to the principal axis of the upper arm. At the cathode location of maximal response, a template was drawn, as per Figure 5.3, to facilitate stimulus electrode placement parallel, perpendicular and at forty-five degrees to the principal axis of the upper arm. In all cases, the separation between the electrodes of the dipole was maintained at approximately 3.5 cm and the stimulus pulse width was maintained at 50 μs. The limb position and elbow angle were kept constant for each subject during the course of the experiment.

The stigmatic electrode was made by cutting a 27 × 22 mm EKG electrode (Sentry Medical Products, Irvine California) longitudinally, and mounting the 2 halves end to end over the thenar eminence to cross the first metacarpal bone perpendicularly at the junction of its proximal and middle thirds. The reference electrode was half of another EKG electrode over the proximal phalanx of the thumb. A ground reference electrode was placed on the posterior aspect of the hand. All experiments were performed with an Advantage Medical EMG machine and the conduction velocity test software package. The machine specifications and settings used for this experiment are identical to the details outlined earlier in section 5.1. The data output from the conduction velocity test software on the Advantage machine consists of a printout that records the stimulus current pulse amplitude in milliamps and the maximum amplitude, in millivolts, of the resultant M-Wave.

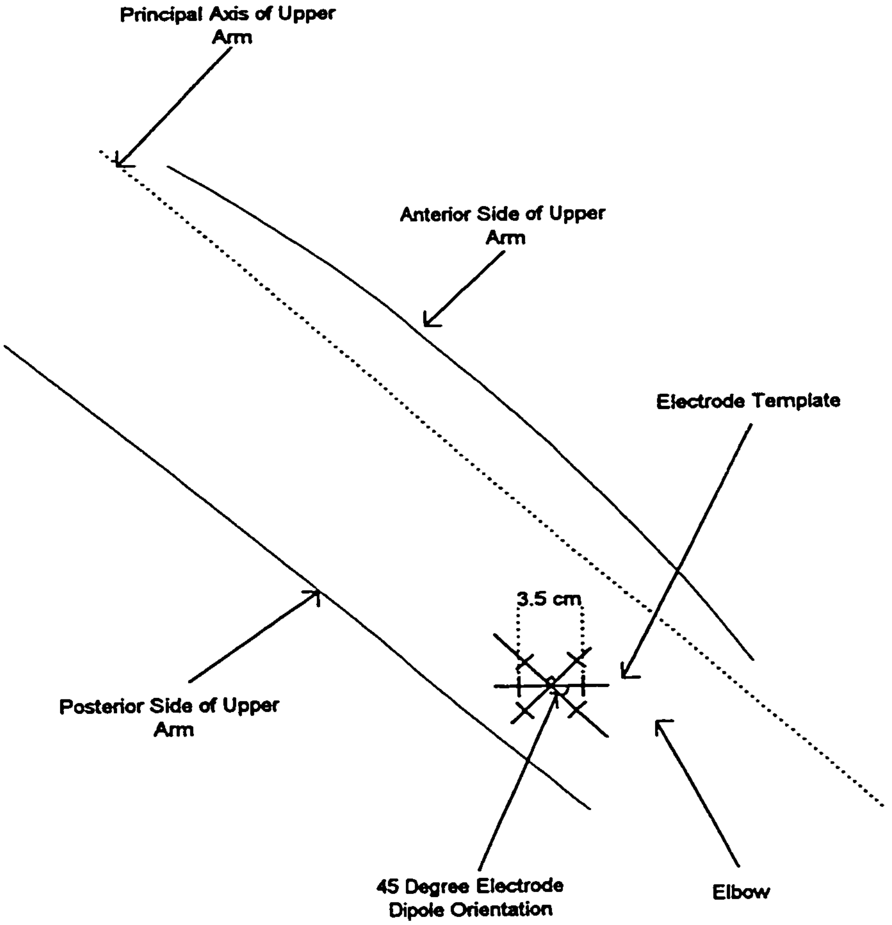

Figure 5.3 Idealized representation of the medial side of the left upper arm showing the location of the elbow and the approximate positioning of the stimulus electrode template. The electrode dipole oriented at 45° to the principal axis of the upper arm is illustrated along with the perpendicular and parallel electrode dipole orientations. All the angles drawn on the electrode dipole template are relative to the line labeled Principal Axis of the Upper Arm that is roughly parallel to the long cylindrical axis of the upper arm.

The electrode orientation experiment was conducted by increasing the stimulus current pulse from zero amplitude until a consistent minimal detectable response was observed. The stimulus was then increased in approximately 5 mA increments and the average maximal M-Wave amplitude for 10 pulses was recorded. This process was continued until the increase in stimulus current amplitude elicited a relatively small or negligible increase in the maximal M-Wave response amplitude. The leveling off region of the response versus the stimulus current amplitude is referred to as the plateau

	45° Slope (V/A)	45° Shift (mA)	0° Slope (V/A)	0° Shift (mA)	90° Slope (V/A)	90° Shift (mA)
Subject #1	0.203	33.1	0.196	56.6	0.124	49.7
Subject #2	0.279	30.1	0.316	49.9	0.270	54.6
Subject #3	0.142	112	0.219	106	0.061	106
Subject #4	0.094	51.2	0.069	44.8	0.056	56.0
Subject #5	0.203	51.2	0.143	76.8	0.067	76.8

Table 5.1 Electrode orientation experimental data for all subjects.

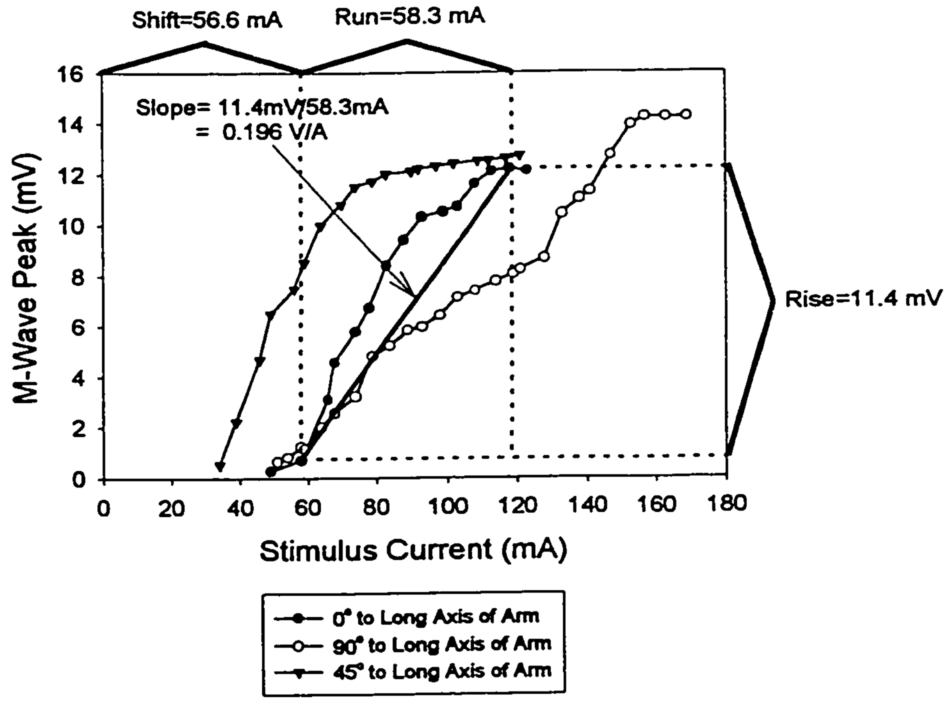

Figure 5.4 Illustrated calculation of the slope of the M-Wave peak versus stimulus intensity curve with the electrode dipole oriented parallel to the long axis of the arm for Subject #1. The maximum value of 11.4 mV is used in the slope calculation for all three curves.

5.3.2 Results

For all the subjects investigated, the results demonstrate a significant difference in the observed stimulus response for different electrode orientations. Figure 5.4 illustrates a typical maximal M-Wave amplitude response versus stimulus current amplitude curve for one of the five subjects studied. The effects of electrode orientation on the stimulus response were quantified by considering two variables associated with the sigmoidal stimulus response versus stimulus intensity curves. Figure 5.4 also shows how the curve characteristics were quantified. For different electrode orientations, a change in the minimum stimulus current required to elicit an M-Wave response was often observed. This variable horizontal shift shown in Figure 5.4 was characterized with a shift quantity that defines the minimum excitation current required to elicit a greater than minimal M-Wave response. The minimal M-Wave response was the first consistent motor unit action potential elicited at a minimum stimulus level.

In addition to the shift value, variations in the slope of the rising segment of the stimulus response versus stimulus intensity curves for different electrode orientations were also observed. In order to specify the rise of this slope, the same maximum M-Wave amplitude value was used for all electrode orientation curves measured for a given subject. There were small variations in the leveling off potential for high current stimuli observed for different electrode orientations in the tests done on each subject. In these cases, as shown in Figure 5.4, the smallest leveling off potential observed for all three electrode orientations tested was chosen as the maximum M-Wave amplitude value for calculating the rise of the slope. The higher leveling off potential for the 90° orientation could reasonably be ignored because it probably resulted from stimulation of the ulnar nerve at high stimulus currents. The ulnar nerve also innervates part of the thenar muscle specifically the deep head of the flexor pollicis brevis. For some subjects, the leveling off potential for all electrode orientations could not be reached within the available stimulus current amplitude range on the EMG machine. In these situations, the smallest stimulus response amplitude potential at maximum stimulus current for all three electrode orientations was taken as the maximum M-Wave amplitude for calculating the rise of the slope.

The rise of the slope was calculated by taking the difference between the maximum M-Wave amplitude described above and the value of the first acceptable M-Wave potential amplitudes that were observed. The run of the slope was calculated by taking the difference between the stimulus current amplitude values for these two points. Table 5.1 presents the results of these calculations for the 5 subjects studied. Each point on the stimulus response versus stimulus intensity curves is the result of ten averages taken from ten independent stimulus pulse measurements. The averaging capability is an inherent feature of the nerve conduction velocity test software on the EMG machine.

5.4 Discussion of Stimulus Electrode Orientation Experiment Results

Although the non-ideal characteristics of tissue anisotropy and the biophysical characteristics associated with the nerve fiber stimulation contribute to the differences in the M-Wave response observed for different electrode orientations, it is difficult, in practice, to isolate the effects of each experimentally. As an alternative, we chose to stimulate the median nerve at a fixed site on several subjects and observe the gross effects of electrode orientation. Both the tissue anisotropy and the biophysical constraints of the nerve fibers imposed by their direction relative to the direction of the stimulus electrodes are contributing factors to the observed results.

It cannot be said, with any certainty exactly what the orientation of the median nerve is at the stimulation site we used for each of the subjects tested. Anatomical illustrations suggest that, at this specific point of stimulation, the median nerve is oriented at an angle to the principal axis of the upper arm that is most consistent with the forty-five degree stimulus dipole orientation [45]. The electrophysiological evidence is consistent with this hypothesis in that we observe the maximal response (maximum slope) when the electrodes are oriented at forty-five degrees to the principal axis of the upper arm in most subjects. A minimal response is observed when the electrodes are oriented at ninety degrees or perpendicular to the principal axis of the upper arm in all subjects. It should however be noted that inhomogeneity and anisotropy of the tissue under the electrodes at the stimulus site will also be a contributing factor to these observations. As well, some of the inconsistencies in the observations likely result from different nerve-arm axis orientations for the different subjects studied.

The reason for the observed stimulus current requirement differences to achieve the same M-Wave response for different electrode orientations can also be explained on the basis of equation (4.6) presented earlier. There is a biophysical requirement, described by equation (4.6), that necessitates that there be a spatial variation in the potential along the length of the nerve fiber in order that the sources that drive the nerve fiber towards excitation be non-zero. In a conceptual situation, where perpendicular stimulation is carried out on a nerve fiber that is situated in a perfectly electrically homogeneous and isotropic environment, the potential distribution will be the same at all Nodes of Ranvier along the length of the fiber under the electrodes if a uniform current density from the electrodes is assumed. The only spatial variation in this situation will be associated with the fringing effects of the electric field at the end points of the electrodes. In a practical perpendicular stimulation experiment, there will also be electrical inhomogeneities associated with the different tissue types located under the electrodes. These electrical inhomogeneities will contribute to the spatial variations in the potential along the length of the nerve fibers and consequently the fibers will eventually be recruited although at larger stimulus current amplitudes.

From a theoretical perspective, excitation of an unmyelinated cylindrical axon in a uniform electric field that is oriented perpendicular to the fiber axis is much more difficult than when the field is oriented in the direction parallel to the axis. The reason for this discrepancy in the ease of recruitment is that the transmembrane potential in the perpendicular case is directly proportional to the electric field with a constant of proportionality equal to the fiber diameter. In the parallel case, the constant of proportionality is equal to the length constant of the fiber which is typically an order of magnitude larger [43,72]. As a consequence of the difference in scaling constant size, the fiber is recruited much more easily with the parallel oriented field.

The values shown in Table 5.1 demonstrate some variability among the subjects tested. However, the combination of the shift values and the slopes for all of the subjects, with the exception of the third, demonstrate a consistent trend. Three of the five subject's stimulus response versus stimulus intensity curve slopes demonstrate that a higher stimulus current amplitude is required to recruit the same amplitude M-Wave as the electrode orientation is changed from forty-five to zero to a ninety degree orientation. The trend observed for the second and third subject is different in that the order of recruitment difficulty is interchanged for the forty-five and zero degree electrode dipole orientations. Such an observation would be consistent with a median nerve orientation that is more parallel to the principal axis of the upper arm as opposed to a forty-five degree orientation at the stimulation site.

Gross changes in electrode orientation can result in differences in the stimulus current requirement for recruiting the same amplitude M-Wave. It is unlikely that in practice there would exist such large discrepancies in electrode orientation during tests on the same subject however, smaller variations in electrode orientation, on the order of five to ten degrees, are to be expected. One method to eliminate the standardization problems associated with electrode orientation is to develop an automated system for seeking out the maximal M-Wave response at a fixed stimulus current amplitude for a series of different electrode dipole orientations at closely spaced intervals. Such a device would consist of an electrode array, with stimulus dipoles oriented at five to ten degrees apart, that is driven by a current stimulator where the current can be switched between the different electrode dipoles under computer control. An analog to digital converter card connected to the same computer could then measure the amplitude of the M-Wave for the different electrode dipole orientations as it automatically routed the current through the various dipoles. A prototype design of this type of instrument is described in Appendix B.

Chapter 6: Conclusions and Recommendations for Future Investigation

6.1 Conclusions

The principal goal of this thesis was to establish a scientific and quantitative basis for describing specific observations during clinical electrical stimulation that to date have only been described qualitatively from both a theoretical perspective and an empirical one. There has been some focus in the relatively recent biomedical literature on the effects of electrical stimulus waveform variables on the stimulus response. From a simulation perspective, these studies have focused on single fiber stimulus pulse amplitude versus stimulus pulse duration simulations that give some insight as to the trends that would be observed during electrical stimulation with variable stimulus pulse width and variable perpendicular distance between the stimulus electrode and nerve fiber. The simulation approach adopted by these investigators does not facilitate a quantitative comparison between predictions made by the mathematical models and experiments that have been performed that attempt to demonstrate the effects of variable stimulus current pulse width. There are two principal reasons for this lack of quantitative comparability. The first reason is that the modeling that has been presented to date does not incorporate information about the anatomical distribution of nerve fiber diameters within a nerve trunk. Inclusion of this anatomical information in the modeling is essential because the electrical properties of the nerve fibers, or more specifically, the ease with which the fibers are recruited is strongly dependent on the individual nerve fiber diameters. In this thesis, a simulation model has been developed that incorporates anatomically consistent nerve fiber diameter distributions that are used to randomly generate a realistic population of nerve fiber diameters. The simulation procedure determines whether or not each individual virtual nerve fiber in the simulated population has fired based on different electrical current stimulus conditions. Because the simulations include information about the nerve fiber diameter distributions, the recruitment patterns that are predicted by the simulations can, in a statistical sense, be compared with empirical results from a suitably designed experiment to investigate nerve fiber recruitment characteristics as a function of stimulus current pulse width. The details of this approach have been reported in the literature [73]. The above discussion can be summarized with the following conclusive statement.

Conclusion #1 Quantitative comparisons of values such as the average recruited nerve fiber diameter can be made between variable stimulus current pulse width simulations and experimental results when the simulation model includes information about the anatomically observed distribution of nerve fiber diameters [73].

Of equal importance to the stimulus current pulse width simulation issue is the problem of developing an experiment that yields measurements that can be compared with the simulation results. The more conventional approaches presented thus far in the literature have been based on measuring the force generated by muscles where the nerve is stimulated with a variable stimulus current pulse width. Unfortunately, these techniques do not lend themselves well to direct comparison with the nerve fiber excitation sensitivity simulations presented thus far because information concerning the nerve fiber diameter distribution is not included in these simulations. Another important reason that these experimental results cannot be quantitatively compared with excitation simulations is that the association between nerve fiber recruitment patterns and the force of the resultant contraction is not easily quantifiable. What is required is an experiment where an observable value can be measured and related back to the nerve fiber diameter. The motor unit number estimation technique provides a latency value associated with the stimulus response of each individual motor unit. Motor unit or M-Wave latency information is used in clinical assessment of patients with suspected neuropathies to give motor nerve conduction velocities, however latency data from motor unit number estimation studies is not typically used for clinical purposes. The experiment proposed in this thesis that uses the latency data to estimate recruited motor nerve fiber diameters is a novel approach to the empirical evaluation of the effect of stimulus current pulse width variations. If certain specific assumptions are made that have been discussed in detail earlier in this thesis, this latency value can be used to obtain an estimate of the motor nerve fiber diameter associated with that specific motor unit. From a sample population of motor unit latency data for each stimulus current pulse width, an estimate of the average recruited motor unit nerve fiber diameter can be obtained which can then be compared with simulation results.

Conclusion #2 The latency value associated with motor unit number estimation data, or more specifically the individual motor unit waveforms, can be used to estimate the motor nerve fiber diameter. This comparison assumes a linear relationship between the nerve fiber conduction velocity and the fiber diameter. A population of recruited motor nerve fiber diameters can then be used to evaluate recruitment patterns such as average, minimum, and maximum recruited nerve fiber diameters and these values can be compared with the simulations results discussed earlier. Our experimental results reported in the literature demonstrated, for the parameters quoted, a decrease in the normalized estimate of the average recruited nerve fiber diameter of approximately ten percent when the stimulus current pulse width was varied from 50 µs to 500 µs [73]. The three millimeter depth simulation exhibited a twenty percent decrease when the stimulus pulse width was varied between 10 µs and 1 ms.

An important issue relating to nerve fiber recruitment simulations is the realism associated with the modeling of the tissue structures that make up the virtual simulation domain. Previous investigators have demonstrated that accurate modeling of tissue conductivity properties are essential in volume conduction models. A good example of this phenomenon is the necessity of including anisotropic tissue conductivity properties when reconstructing nerve compound action potential waveforms [36,74]. In this thesis, the gross effects on the potential distribution of the conductivity associated with the tissue external to the nerve trunk have been investigated quantitatively for the first time. Simulation results based on steady state DC excitation have demonstrated that there is a significant difference in the predicted recruitment patterns of nerve fibers when comparing the results associated with an anisotropic and an isotropic volume conduction model.

Conclusion #3 Including anisotropy in modeling the conductivity properties of the volume conductor in nerve fiber excitation simulations has a significant impact on the predicted recruitment patterns. For the case of muscle tissue conductivity anisotropy studied, the difference in the average recruited nerve fiber diameter between the anisotropic and isotropic cases can be as great as nearly seven percent.

Along with stimulus current waveform variables such as the stimulus pulse width, the geometric orientation of the electrodes can have a dramatic impact on the ease with which motor nerve fibers and hence motor units are recruited. Both the direction of the tissue conductivity and the target nerve relative to the orientation of the stimulus current dipole can be expected to have an impact on the ease of recruitment however nerve orientation appears to be dominant due to several theoretical factors that have been reviewed previously in this thesis. The degree of contribution of each of these factors is difficult to assess from experimental data. From the perspective of standardizing or facilitating nerve conduction experiments performed on a patient, the ability to consistently orient the stimulus electrode dipole would be of some benefit. The novel experiment outlined in this thesis can be used as the basis for the development of an automated technique for consistently determining the optimal electrode orientation on a patient.

Conclusion #4 Geometric orientation of the electrodes has a significant impact on the ease with which motor nerve fibers are recruited. The stimulus current amplitude required to elicit an 8 mV amplitude M-Wave for a non optimal electrode orientation in one of the subjects studied was nearly double that of the stimulus amplitude required for the optimal electrode dipole orientation.

As the stimulus current pulse width is increased, there is a relatively small but definitive decrease in the average recruited fiber diameter. Simulation studies predict that this effect is more prevalent at longer distances between the stimulus electrode and the nerve trunk. Experimental evidence supports the predictions of decreased average recruited nerve fiber diameter with increasing stimulus current pulse width. This conclusion is based on the evidence associated with an alteration in the distribution of the first 20 motor nerve fibers that are recruited with varying stimulus pulse width.

Conclusion #5 There is a small but definite theoretical effect on recruitment patterns as pulse width is varied. The study presented earlier demonstrates an approximately twenty percent change in the average recruited fiber diameter for the range of stimulus pulse widths studied and the parameters that were quoted. Experimental evidence supports the theoretical predictions of this effect made by the simulation studies.

6.2 Recommendations for Future Investigation

As was mentioned earlier, much of the focus in the literature on nerve fiber excitation modeling has gone into refinements of the nerve fiber equivalent circuit models. These refinements have included the addition of non-linear effects associated with the membrane conductances and proposals of new procedures for reducing the computational intensity associated with calculating the change in the transmembrane potential for a given stimulus amplitude. While these are important developments that are not to be minimized, it may be said that relatively little effort has gone into refinement of the models associated with the intervening tissue and analysis of the effects of simplifying approximations that are routinely made with regards to tissue electrical properties in these models. There is room for further work in applying more complex tissue models to nerve excitation simulations and further quantitative investigation of the impact of simplifying approximations on nerve fiber excitation simulations.

A more comprehensive mathematical model of the tissue volume conductor could be implemented with a three dimensional simulation. This refinement to the finite difference approach would remove the assumption inherent in the nerve fiber excitation simulations where it is assumed implicitly that the sampled population of nerve fibers all lie along the same plane of the two dimensional virtual space. There is some merit to developing a three dimensional simulation because geometric nerve fiber recruitment in the third dimension could then be quantitatively investigated. The principal drawback to implementing a three dimensional simulation is the increase in computational effort associated with solving for the potential distribution in the three dimensional volume conductor. It should however be pointed out that recent advancements in parallel computing architectures and the proposal of network topology reduction procedures for biomedical volume conduction problems will make the three dimensional field simulation a computationally reasonable alternative in the future [75,76]. Recent implementation in MATLAB that facilitate larger than two dimensional matrices go a long way towards simplifying the programming associated with three dimensional volume conductor modeling.

Further enhancements to the electrical equivalent circuit models of the nerve fibers presented in this thesis could also be implemented that account for the non-linear characteristics of the membrane conductances. This enhancement would allow for greater accuracy when evaluating the excitatory effects of extremely narrow stimulus current pulses as has been discussed earlier in this thesis. There is however a minimal advantage to implementing this refinement for the steady state DC stimulus or relatively long stimulus pulses that does not warrant the increase in computational effort required when considering the gain in the overall accuracy of the solution.

Although the simulations presented in this thesis incorporated depth dependent effects, further simulation studies that directly investigate the geometric localization effects on nerve fiber recruitment would be beneficial.

In addition to the experiments that were carried out to investigate the effects of variable stimulus current pulse width and stimulus electrode orientation, additional experiments could be performed to investigate the effects of variable tissue conductivity. As well, the effect of other stimulus protocols, whether different wave shapes or electrode configurations, could be further investigated theoretically using the comprehensive model developed in this thesis. The ability to simulate the expected effects of varying these quantities would be beneficial in theoretically predicting the outcome of experiments designed to test the effects of the parameter changes.

Appendix A: Measurement of Skeletal Muscle Tissue Conductivity

Experimental measurement of tissue conductivity is fundamental to nerve fiber recruitment pattern simulations where the fibers are assumed to lie in a realistic tissue medium. In order to accurately model the tissue electrical properties, knowledge of the tissue conductivity values is essential. Tissue conductivity measurement is also essential from the practical perspective of tissue identification in the newly developing field of tissue impedance imaging as well as the differentiation between diseased, necrotic and healthy tissue [77,78].

In this appendix several different experimental techniques for measuring tissue conductivity that have been investigated are discussed. Before describing these techniques, the theoretical basis behind calculating the anisotropic conductivity from the potential measurements done parallel and transverse to the direction of the skeletal muscle fibers is explained. It is important to introduce the calculation procedure that is based on the universally used four electrode configuration because the calculation is common to all the techniques for tissue conductivity measurement that are subsequently described.

The techniques for measuring tissue conductivity that are discussed include traditional swept frequency techniques that have been reported by several individuals in the literature. An alternative to the swept frequency approach is introduced based on an idea that was proposed in the 1940's that is more commonly associated with circuit frequency response measurements. In describing these techniques, the advantages and disadvantages will be highlighted in terms of the following criteria:

1) Attainable measurement bandwidth
2) Speed of the measurement
3) Measurement apparatus complexity

In conclusion, the frequency dependent tissue conductivity measurements that were made using the modified current pulse technique will be presented and discussed.

A.1 Tissue Conductivity Calculations and the Four Electrode Technique

Many of the reported tissue conductivity experiments use a four electrode configuration, as shown in Figure A.1, as the basis of the experiment [79]. In the four electrode measurement, a current source drives current I_c between the two outer electrodes while an analog to digital converter connected to the output of an instrumentation amplifier measures the potential difference V_c between the two inner electrodes. As per the diagram, the electrodes are placed an equal distance m apart from each other.

If the tissue specimen has a thickness t_c that is large compared to the length of the electrode array $3m$, the specimen may be considered to be semi-infinite. If the tissue is assumed to be both homogeneous and isotropic, the current will leave the electrodes in radial paths where the equipotential surfaces are hemispherical. The current density from each of the electrodes at any point in the tissue can be calculated by dividing the current from the electrode by the surface area of the hemisphere that intersects the reference point as per equations (A.1) and (A.2).

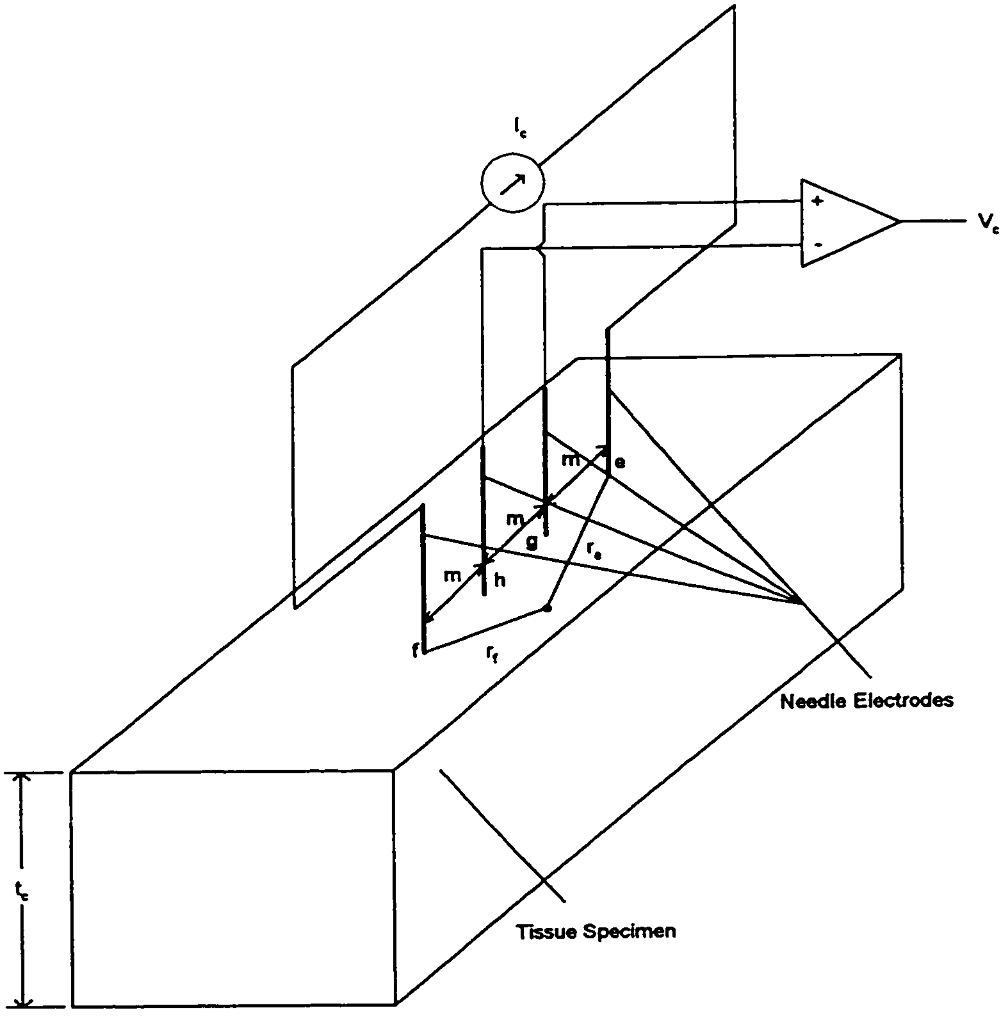

Figure A.1 Idealized representation of tissue conductivity measurement using the four electrode technique. The diagram shows the four needle electrodes placed at equal distance *m* from each other. A current source drives current I_c through the outer two needle electrodes while the potential difference V_c between the inner two electrodes is measured.

$$J_e = \frac{I_c}{2\pi r_e^{\,2}} \tag{A.1}$$

$$J_f = \frac{I_c}{2\pi r_f^{\,2}} \tag{A.2}$$

The current magnitude from the two current electrodes is I_c and $-I_c$ respectively and the radial distances from the electrodes to the point of interest are r_e and r_f respectively. We can write the potential difference between the potential sensing electrodes labeled g and h as the superposition of the potentials. The resultant measured potential V_{gh} can therefore be written as:

$$V_{gh} = V_g - V_h = \int_m^{2m} \frac{I_c}{2\pi\sigma_c r_e^{\,2}} dr_e - \int_{2m}^{m} \frac{I_c}{2\pi\sigma_c r_f^{\,2}} dr_f = \frac{I_c}{2\pi\sigma_c m} \tag{A.3}$$

We can then use V_{gh} to solve for the tissue conductivity, as per equation (A.4), which is the desired quantity in this case.

$$\sigma_c = \frac{I_c}{2\pi m V_{gh}} \tag{A.4}$$

While valid, the above development is only applicable, in its present form, to isotropic media. As has been shown in previous chapters, some tissue types such as skeletal muscle are non-ideal because they are electrically anisotropic. The previous development must therefore be modified to account for tissue anisotropy [61,79].

In general, the anisotropic biological medium can be viewed as having a different conductivity in the three principal axis directions x_c, y_c and z_c. The conductivity in the three directions will be defined as σ_x, σ_y and σ_z. If the biological tissue medium is assumed to be electrically homogeneous and anisotropic, the conductivity values in the three directions will be constant. Through the use of a coordinate transformation, the anisotropic situation can be transformed to an isotropic one where the primed values are associated with the new coordinate system as shown:

$$\begin{aligned} x' &= \frac{\sqrt{\sigma_y \sigma_z}}{\sigma_c} x_c \\ y' &= \frac{\sqrt{\sigma_x \sigma_z}}{\sigma_c} y_c \\ z' &= \frac{\sqrt{\sigma_x \sigma_y}}{\sigma_c} z_c \end{aligned} \tag{A.5}$$

The parameter σ_c is an arbitrarily chosen constant that represents the conductivity of the virtual isotropic medium. In the virtual system, the potential distribution ϕ is chosen such that potential at the transformed coordinates x', y', z' are identical to the potential at the x_c, y_c, z_c coordinate in the original system as per equation (A.6).

$$\phi'(x',y',z') = \phi(x,y,z) \tag{A.6}$$

If we consider the case of homogeneous anisotropic skeletal muscle tissue as an example, we can define the coordinate system such that the x_c and z_c directions are parallel to the low conductivity direction and the y_c direction is parallel to the high conductivity direction. Given the expression for the relationship between the stimulus current, the inner electrode potential and the conductivity that was derived for the four electrode configuration shown in equation (A.4) and the geometric variable transformation of equation (A.5), an expression can be derived relating the conductivity in the directions transverse and parallel to the muscle fibers to the stimulus current amplitude and the inner electrode potential difference as per:

$$\sigma_L = \frac{I_c}{2\pi m(V_{gh})_H} \tag{A.7}$$

$$\sigma_H = \left[\frac{(V_{gh})_H}{(V_{gh})_L}\right]^2 \sigma_L \tag{A.8}$$

In the above expressions, the ***m*** variable is the inter-electrode spacing, V_{gh} is as defined in equation (A.3), I_c is the stimulus current amplitude and σ is the conductivity. The capital subscripts **L** and **H** indicate potential measurements and conductivity values for the low and high conductivity directions respectively.

A.2 Experimental Techniques for Measuring Skeletal Muscle Tissue Conductivity

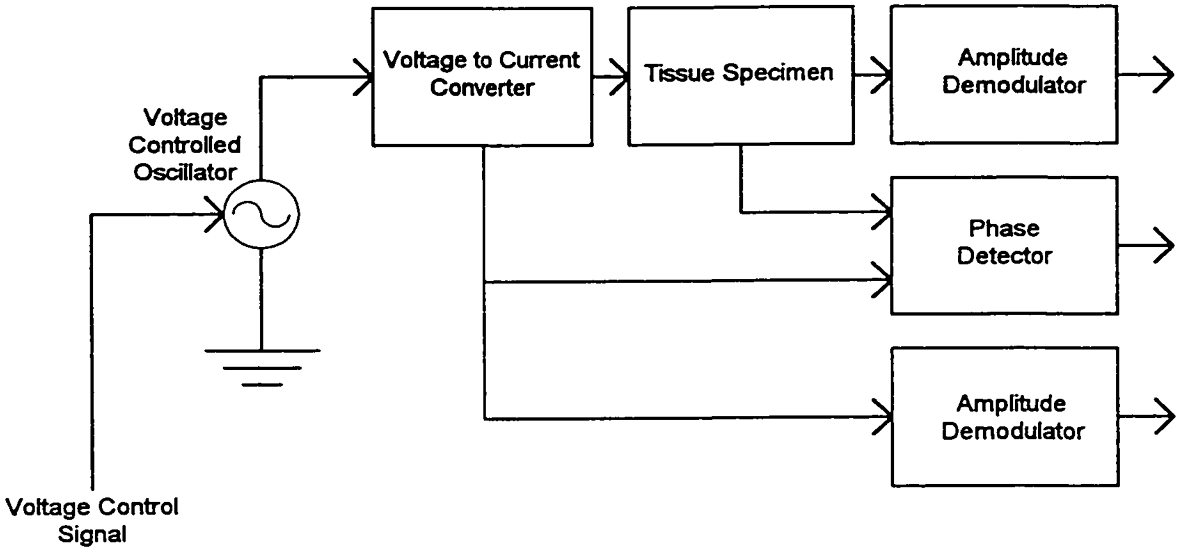

Figure A.2 Block diagram of swept frequency tissue conductivity apparatus. A tissue specimen is excited by a sinusoidal current signal that is generated from a voltage controlled oscillator. The differential voltage generated across the two inner electrodes of the four electrode configuration shown in Figure A.1 is amplitude demodulated. A phase detector is used to determine the phase shift between the sinusoidal excitation current signal and the sinusoidal potential waveform measured from the tissue sample. The excitation current amplitude is converted back to a differential voltage signal and amplitude demodulated to determine the amplitude of the excitation current. A voltage control signal steps the voltage controlled oscillator frequency and a measurement of the complex conductivity is made at the desired number of points across the usable system bandwidth.

The preferred approach of measuring skeletal muscle tissue conductivity, from a historical perspective, is based on a swept frequency technique [22]. Figure A.2 is an illustration of the basic instrumentation for a swept frequency conductivity measurement apparatus. The basic idea behind the swept frequency technique is to excite the tissue specimen with a sinusoidal current source where the current is driven between the two outer electrodes of the traditional four electrode configuration. The sinusoidal current frequency is swept from low to high frequencies and the resultant potential amplitude is measured at each of the frequency steps. In addition, the phase difference between the excitation current sinusoid and the resultant potential sinusoidal wave is measured.

The one principal advantage of the swept frequency approach to tissue conductivity measurement is the large measurement bandwidth available. Bandwidth limitations associated with this technique are dictated by the bandwidth of the voltage controlled oscillator and the components used to construct the amplitude demodulators and the phase detectors. A disadvantage of the swept frequency technique is the time required to obtain conductivity measurements across the bandwidth of interest particularly at low frequencies. The relatively long measurement time is particularly critical when *in vivo* measurements are performed. A swept frequency conductivity measurement apparatus, in general, requires more components than the pulsed transient measurement method that will be discussed below. However, no analog to digital sampling hardware is necessary since the complex conductivity can be calculated from the amplitude demodulator and phase detector signal values.

An alternate and in some instances preferable technique to the swept frequency method discussed above is the pulsed transient technique first described by Teorell [80]. This method is borrowed from a method that is more familiar in the field of electronics and is used to obtain the frequency response of a circuit by exciting it with a transient pulse signal and measuring the output.

The formulae that relate the measured potential between the inner two electrodes and the anisotropic conductivity using the four electrode configuration were initially derived by Rush [63] and used by other investigators. These formulae are re-written below with the modification that the stimulus current variable $I_c(f)$ and the measured voltages in the high and the low conductivity directions $V_H(f)$ and $V_L(f)$ respectively are explicitly shown as functions of frequency. The variables $\phi_H(f)$ and $\phi_L(f)$ represent the phase shift between the voltage and current for the high conductivity and the low conductivity directions respectively.

$$\sigma_L(f) = \frac{I_c(f)}{2\pi m V_H(f)} \exp[j\phi_H(f)] \quad \text{(A.9)}$$

$$\sigma_H(f) = \left[\frac{I_c(f)}{V_L(f)}\right]^2 \frac{V_H(f)}{2\pi m I_c(f)} \exp[j(2\phi_L(f) - \phi_H(f))] \quad \text{(A.10)}$$

Construction of the pulsed transient tissue conductivity measurement apparatus can be accomplished with fewer overall components than the swept frequency apparatus that was described earlier. All that is required is a transient current stimulator, a differential amplifier and an analog to digital converter which is interfaced with standard personal computer hardware. A block diagram of the completed pulsed transient tissue conductivity measurement system is shown in Figure A.3.

The pulsed transient tissue conductivity method has the advantage of extremely rapid measurement time since the entire measurement bandwidth can be obtained by recording the stimulus and the response waveform of a single pulse. In practice, it is advantageous to stimulate the specimen with several identical current pulses and synchronously average the stimulus and the response waveform for the purposes of white noise reduction. The most significant and limiting drawback of the pulsed transient tissue conductivity measurement approach is the limitations on the obtainable bandwidth. From a theoretical perspective, the pulsed transient technique should have a virtually infinite bandwidth since the frequency spectrum of the a stimulus current pulse is in theory infinite. In practice the useful bandwidth has been observed to be limited to approximately half of the inverse width of the stimulus current pulse for current pulse amplitudes of approximately 500 μA. The obtainable bandwidth can be increased by decreasing the stimulus current pulse width since a decrease in stimulus pulse width constitutes an increase in the bandwidth of the stimulus current pulse spectrum. There is a lower limit on the stimulus current pulse width that can be used in these measurements that is dictated by the maximum sampling frequency of the analog to digital converter hardware. Figure A.4 is a plot of the impedance magnitude and phase as obtained experimentally from a parallel RC circuit. The PSPICE simulations of the theoretical frequency response magnitude and phase have been superimposed on the plot as a continuous curve.

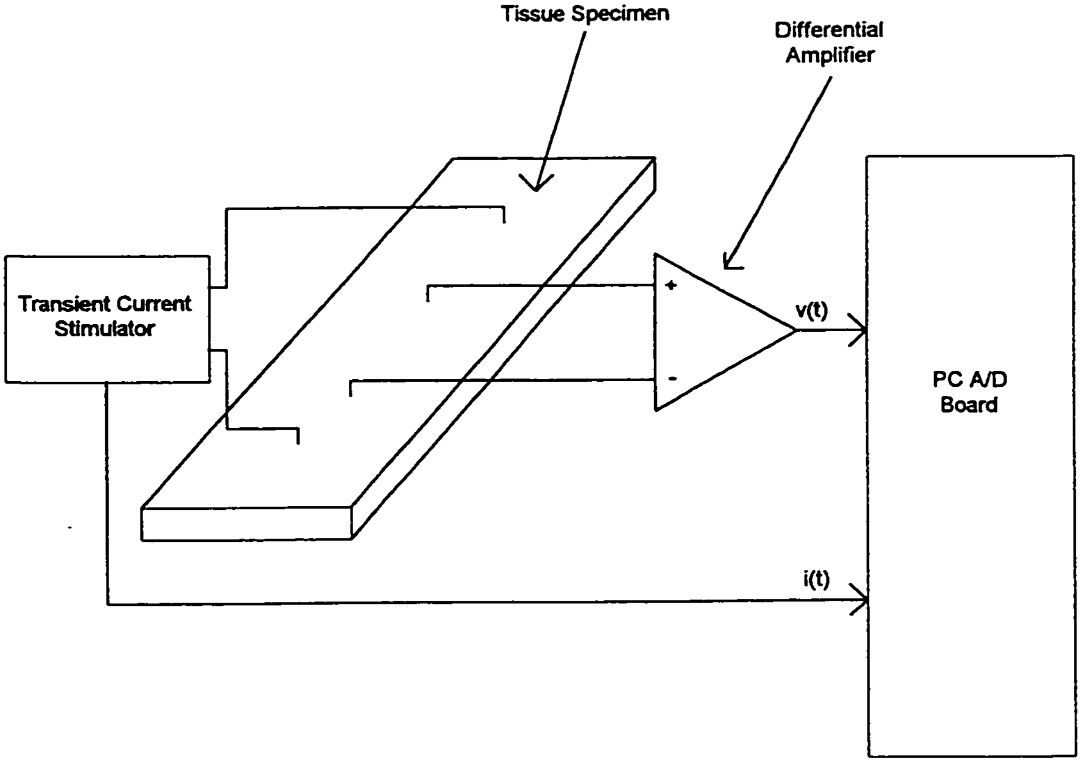

Figure A.3 Block diagram illustrating the major components of the pulsed transient tissue conductivity experiment. A transient current stimulator is used to generate a current pulse. The resulting potential measured between the two voltage sensing electrodes is amplified and the signal is recorded using an analog to digital conversion board in a personal computer. In addition, the stimulation current waveform is also sampled using the same A/D board.

Figure A.5 is a graph of the complex conductivity magnitude and phase obtained from conductivity measurements carried out on poultry breast skeletal muscle tissue in the transverse and parallel directions to the muscle fibers. These measurements were conducted with an electrode spacing ***m*** of 1 mm. Placement of the electrodes was accomplished using a stereoscopic microscope and glass reticle with a 100 μm per division measurement grid. A 400 μA stimulus current amplitude was used. In general the conductivity magnitudes that were obtained in these experiments were greater than would be expected. These results are likely due to the fact that our measurements were not made on fresh animal tissue *in vivo* but on *in vitro* specimens. An increase in tissue conductivity with time after death has been reported by other investigators [9].

In other respects, the results are similar to observations made by Gielen *et al.* [22] for the bandwidth investigated. Gielen's results show a positive phase shift in the conductance for the direction parallel to the muscle fibers and a negative phase shift for the perpendicular direction within the investigated bandwidth. For the majority of the spectrum, the observed trend is a larger conductivity in the direction parallel to the muscle fibers and a smaller conductivity in the perpendicular direction.

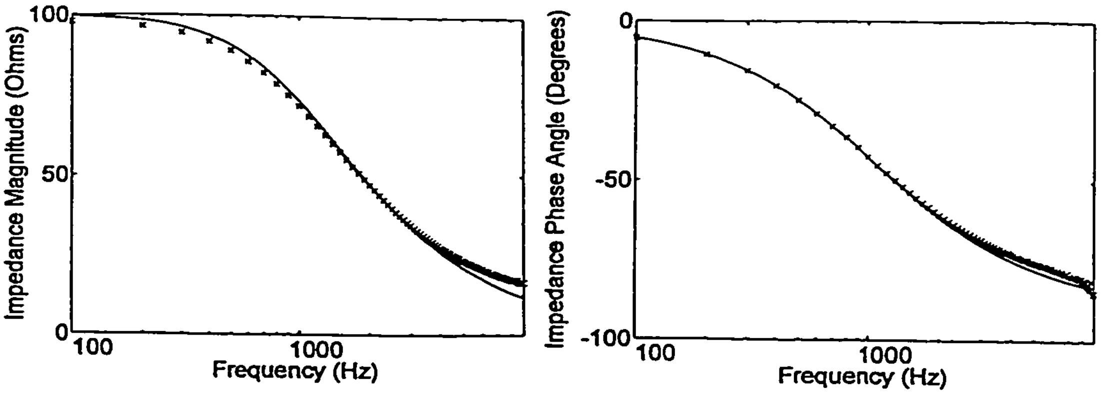

Figure A.4 Plot of the measured impedance magnitude and phase of a parallel RC circuit - x. The parallel resistance is 100 Ω and the parallel capacitance is 1.47 μF. A theoretically calculated plot of the frequency response magnitude and phase have been superimposed on the plot.

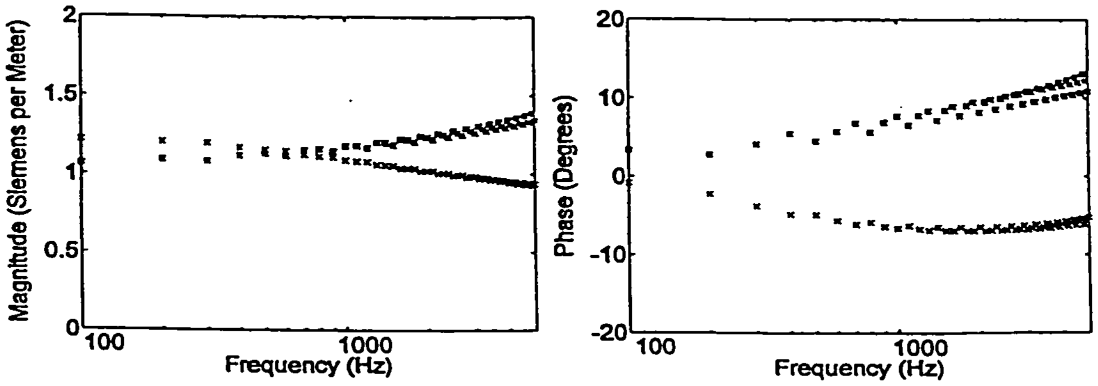

Figure A.5 Plot of the measured complex conductivity magnitude and phase of a poultry skeletal muscle tissue sample. Parallel conductivity data -☆, transverse conductivity data - x.

Appendix B: Automated Instrument Prototype for Consistently Determining the Optimal Stimulus Electrode Dipole Orientation

A novel experiment for ascertaining the effects of variable stimulus electrode dipole orientation was presented in Chapter 5. The motivation for carrying out these experiments was to gain an appreciation of the effects of stimulus electrode orientation on the amplitude of the resulting M-Wave during routinely performed clinical electrophysiological testing. There are many factors that influence the magnitude of the measured electrical response of a muscle when the motor nerve is stimulated such as the stimulus amplitude, the placement of the stimulus electrode dipole and the orientation of the dipole relative to the motor nerve. The results of the experiments presented in Chapter 5 demonstrated that there was a significant difference in the elicited response at various levels of electrical current stimulation for different stimulus dipole orientations. While it may be argued that the electrode orientations that were investigated represented extreme cases and that such a degree of variability would not be encountered clinically, variations in electrode placement of five to ten degrees in a clinical setting would not be out of the ordinary.

B.1 Instrument Design Philosophy

There are several possible approaches that may be considered that could compensate for the changes in the stimulus response associated with variable stimulus electrode orientation. A purely theoretical approach would involve attempting to account for these variations in a volume conduction model and using the results of these simulated effects to scale the measurements. Unfortunately, this approach would require volume conduction models specific to each stimulus site and even if such a variety of models could be generated, they would not account for the anatomical variability in terms of the local tissue structures that is routinely encountered between individuals. A much simpler approach, when only the maximum M-Wave is required is to increase the stimulus amplitude. However, this may cause considerable stimulus pain and even then, the maximum M-Wave may not be achieved because of operating limitations on the equipment. Such operating limitations on stimulus current amplitude can arise when the nerve lies fairly deep in the tissue. Another practical approach would be beneficial such as an automated technique for consistently determining the optimal stimulus electrode orientation. The block diagram of Figure B.1 represents a system level overview of what was required to build an instrument of this type.

With the advent of modern day personal computers, implementation of the device proposed in Figure B.1 was relatively straightforward. The system consists of a stimulus current pulse generator of the type that is routinely used clinically that is triggered by a microcomputer through a custom designed digital input/output port. Recording electrodes on the subject's target muscle group detect the electrical response of the muscle to the excitatory stimulus. This signal is amplified and then digitally sampled using a custom designed analog to digital board.

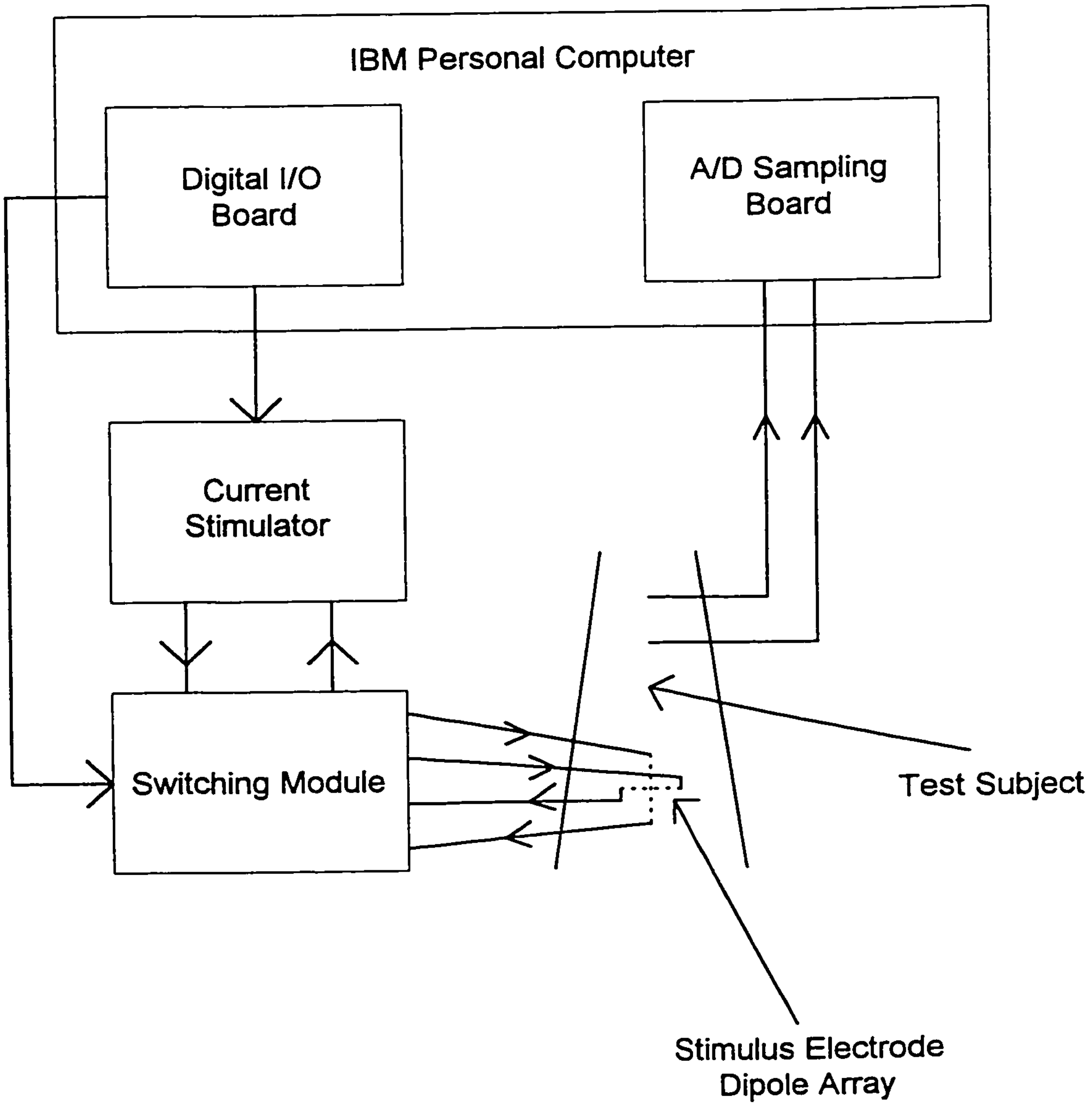

Figure B.1 Automated instrument prototype for consistent selection of optimal stimulus electrode orientation. The block diagram illustrates the main components that comprise the system. The current pulse from the stimulator is routed to a pre-selected stimulus electrode dipole with the switching module under computer control. Not shown explicitly on the diagram is the instrumentation amplifier used to amplify the detected signal.

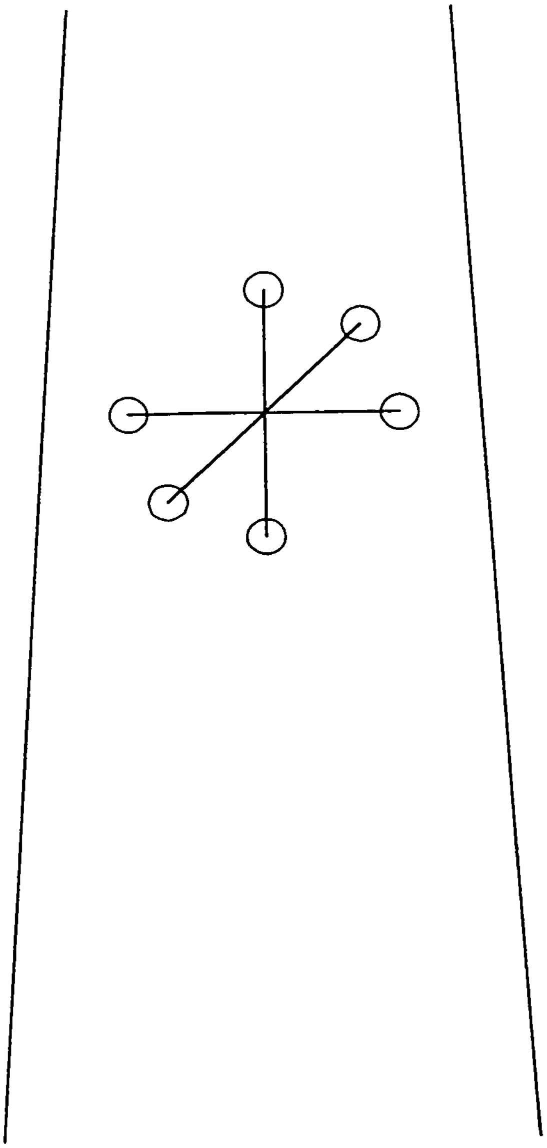

Figure B.2 Illustration of electrode dipole array on the forearm. The diagram shows a three dipole electrode array with the dipole orientations separated by 45°. The typical dipole separation is a few centimeters. (The above drawing is not to scale.)

The automated selection of optimal electrode orientation is accomplished by a computer controlled electronic switch that can selectively route the stimulus current pulse from the stimulator through any of several paths. Each of these current paths is connected to its own stimulus electrode dipole that is placed on the subject. An array of these dipoles, each one of which is connected to its own current path, can be placed on the subject at different orientations as shown in Figure B.2. By automatically routing the current through different stimulus electrodes at different orientations and sampling the stimulus current response, the instrument can detect the stimulus electrode orientation that consistently yields the maximal response. The electrode orientation yielding the maximal response would be considered the optimal stimulus electrode orientation.

Subsequent to determination of the optimal stimulus electrode orientation, it is convenient to leave the electrode array in place for the remainder of the electrophysiological testing. The instrument can be powered down and the computer connection disengaged after which the optimal current path that was determined by the software can be manually selected using a series of switches on the front end of the panel. The operator also has the option of using an integrated test environment hardware system for EMG analysis such as the Advantage EMG machine because the stimulator terminals from the integrated system can be connected to the front panel of the switching instrument.

B.2 Limitations of the Prototype

The prototype that was implemented is limited in the number of stimulus current paths and consequently stimulus electrode dipole orientations that are available for testing to three. An instrument with more channels could be easily implemented by extending the prototype design to include more path modules. From a practical perspective, the number of electrode dipoles at different orientations that can be placed on a subject remains the principal constraint to the number of different electrode dipole orientations that could be tested. A practical design for clinical use would benefit from a custom designed reusable or disposable electrode array with dipoles placed at several fixed orientations. This type of electrode array could likely achieve a greater density of stimulus electrode orientations than is possible with the manual placement of disposable surface electrodes. As an alternative to this approach, a relatively small number of dipoles that only differ by 20° could be used since an electromyographer already has a general estimate of the nerve orientation at specific commonly used stimulus points such as the wrist.

The stimulus current variables such as the stimulus pulse width and amplitude are configured on the control panel that is associated with the stimulus current generator that was used (Dogwood CMS1-200). Choice of stimulus waveform variables are therefore limited to the settings available on the stimulator. For the stimulus amplitudes this range encompasses hundreds of microamps to tens of milliamps. The stimulus current pulse width has five settings ranging from 50 microseconds to 2 ms.

B.3 Detailed Instrument Design

B.3.1 Switching Module

The design of the switching module is based on a bipolar junction transistor driven relay as shown in the diagram of Figure B.3. Each individual current path is constructed with one transistor switch combination. The current path is closed when the transistor is turned on by way of a TTL decoder followed by an inverter. During testing, the manual switches are set to the open position and the current path is selected under computer control through one of the reed relays.

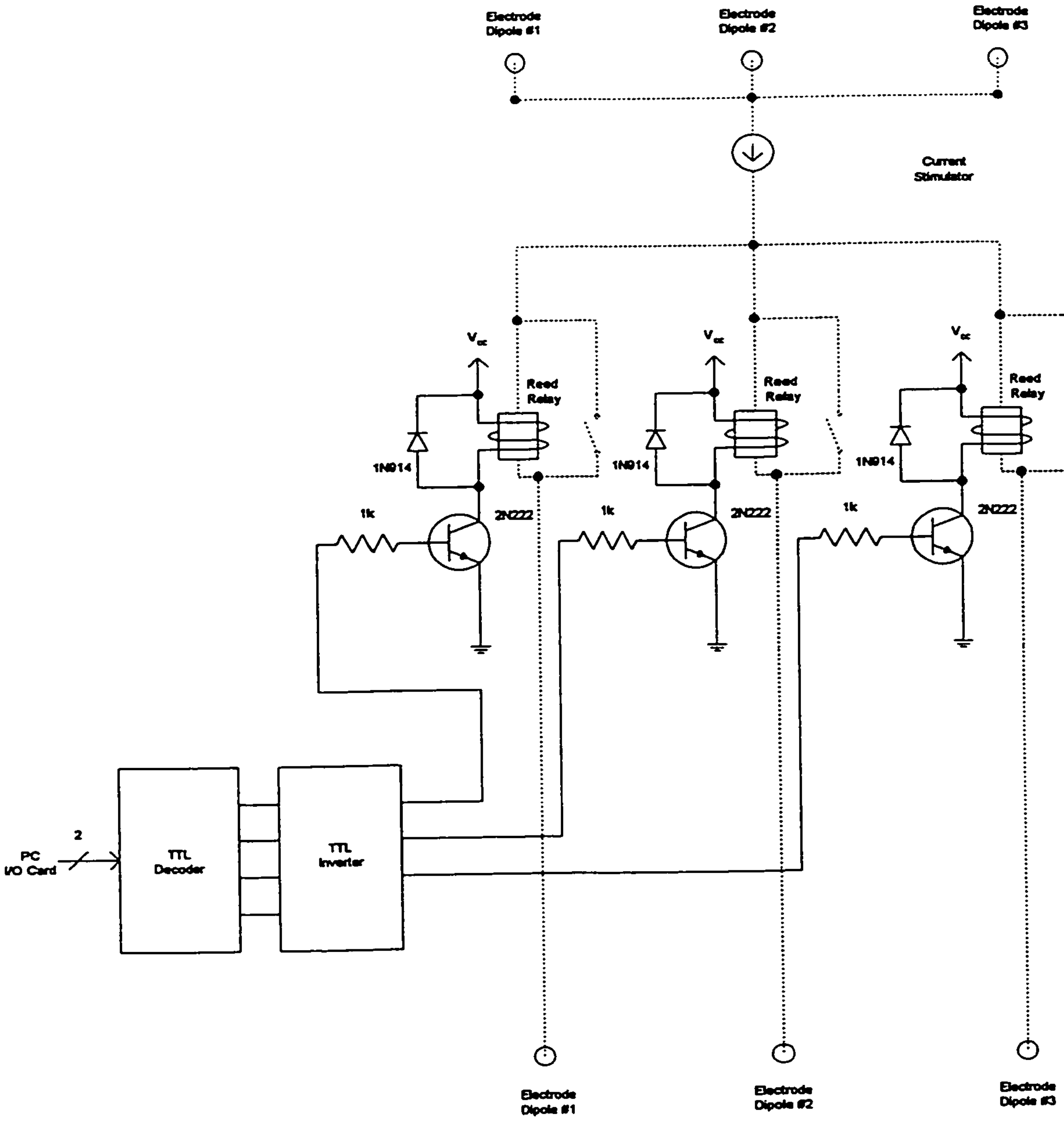

Figure B.3 Electronic diagram of the switching module. The diagram illustrates the transistor relay modules that comprise the current routing mechanism. Interface to the PC I/O board is shown.

After the optimal stimulus electrode dipole orientation is determined, the electronic device can be disengaged and the optimal path selected manually with the appropriate switch located at the front of the switching module instrumentation panel. As was mentioned earlier, the number of different stimulus electrode orientations can be extended by increasing the number of transistor-reed relay modules.

B.3.2 I/O Interface Circuit

The heart of the I/O interface consists of the 8255 parallel programmable peripheral interface integrated circuit. This device includes three eight bit I/O ports that can be configured for input or output. The device is interfaced to the PC AT industry standard architecture (ISA) bus by decoding the address placed on the bus during a I/O port write statement using two TTL 74688 magnitude comparator integrated circuits. When an address is placed on the ISA bus, two magnitude comparator chips compare the high byte and the low byte of the address to a user selected address chosen for the board and manually set using dip switches. If both the high and low byte address are identical to the user selected address the 8255 chip is activated and a data read, write or device command can be issued to the 8255 from the ISA data bus. The exact operation is specified by the two most least significant bits of the address which are routed directly to the device and not to the magnitude comparators as are the other address bits. The output of the two magnitude comparators must be passed through a TTL OR gate in order to generate the single line signal for the 8255 chip select. Two additional lines from the PC

ISA bus must be interfaced with the read and write lines on the 8255 chip so that the device can perform a read or write operation as requested by the software running on the personal computer. All the devices on this board can be powered from the +5 volts supply and ground located on the PC ISA bus.

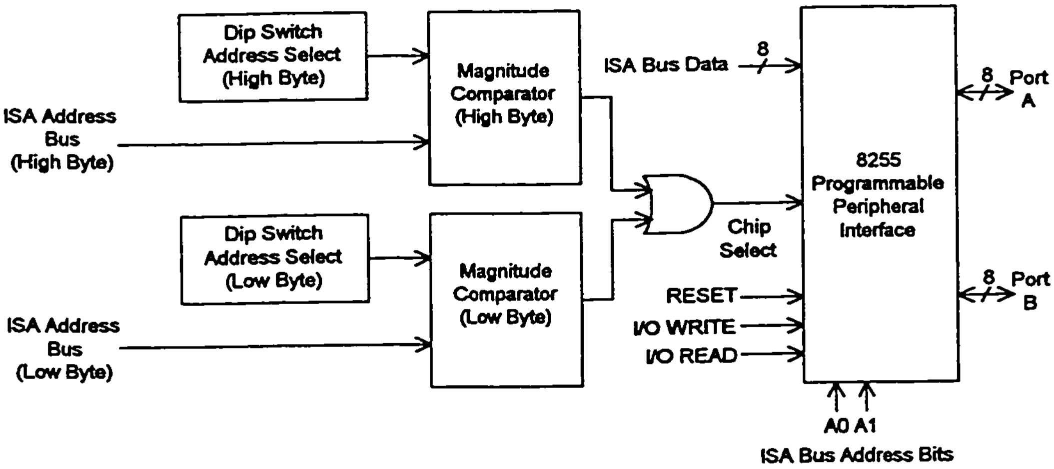

Figure B.4 Diagram of the I/O board electronics. The diagram illustrates the input and control signals from the ISA data bus to the 8255 device and the logic required to decode the address.

The current prototype of the board only uses two of the three available I/O ports for parallel digital data transfer from the computer to an external device which in the case of the electrode orientation instrument is the switching module that was described above. These digital I/O lines are configured in the output mode to select a specific stimulus current path in the switch and to trigger the stimulus current generator to output a single current pulse. Figure B.4 illustrates the design of the I/O board.

B.3.3 A/D Converter Circuit

The analog to digital (A/D) converter was designed around the Analog Devices AD7824 8 bit A/D converter integrated circuit. Normally in electromyography applications, a twelve bit A/D is used to be able to sample the signals with a relatively high degree of accuracy. An eight bit A/D device was chosen for the prototype because the instrument is only required to differentiate between relatively large changes in M-Wave amplitude. Reproduction of the fine details of the M-Wave signal required for clinical work are not necessary in this application. The AD7824 is a versatile four channel analog to digital sampling chip with a 100 kHz maximum sampling rate. The device is powered from a single positive +5 volt supply and requires signal conditioning on the analog input for bipolar signals. This is accomplished with an operational amplifier circuit that maps the bipolar signal range into a positive range compatible with the device input.

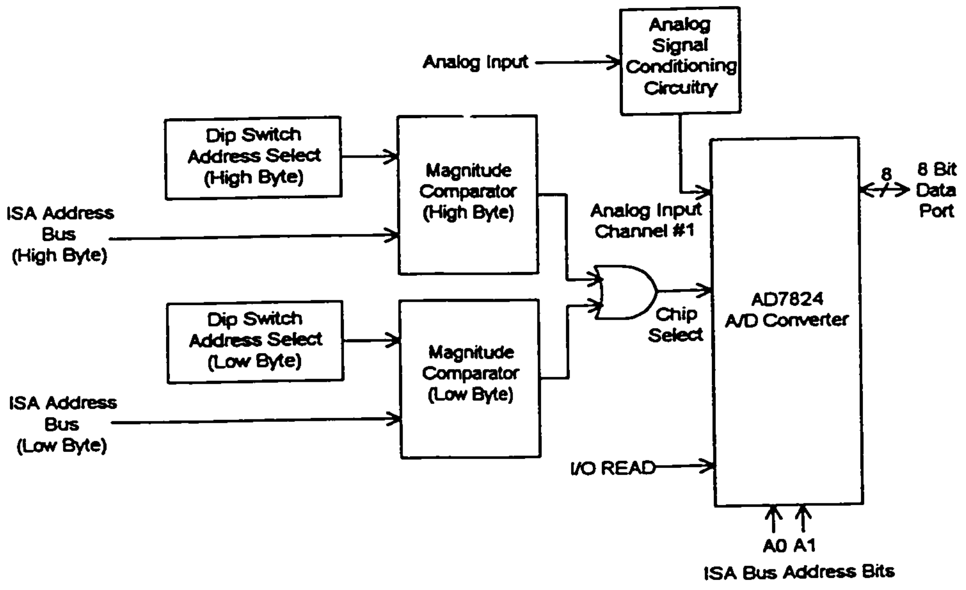

Figure B.5 Diagram of the A/D board electronics. The diagram illustrates the input and control signals from the ISA data bus to the AD7824 device and the logic required to decode the address.

From the perspective of microprocessor bus interfacing, the AD7824 requires the data bus address to be decoded in an identical fashion to the procedure described for the 8255 parallel programmable peripheral interface device. The diagram of the A/D board circuitry is therefore virtually identical to the I/O board circuitry with respect to the decoder. The two lowest bits of the address bus are wired directly to the address lines on the A/D device. This connection allows the driver software to select which of the four analog input channels is to be sampled.

As was mentioned previously, the input to the A/D chip is conditioned by way of a signal conditioning circuit. When the I/O port address matches the preset address of the decoder dip switches and is accompanied by an I/O read strobe, the analog input signal is sampled and converted to an 8 bit byte that is placed on the ISA data bus. The custom software written for the A/D board must then map the eight bit data sample to the corresponding voltage.

B.4 Calibration and Testing Issues

Since the I/O port read statements were generated from within the driver software, maximization of the sampling rate was highly dependent upon optimal coding strategies. A constant sampling rate of 98 kHz was achieved on an 80386 machine. It should be noted that the sampling rate for this proposed instrument design will be dependent on the speed of the computer. Testing of the sampling rate was carried out with a standard square wave signal generator and an oscilloscope trace that was compared to the spacing of the digitized sample points. The information from this comparison was used to generate an estimate of the sampling interval.

Figure B.6 is a plot of an M-Wave sampled using the instrument described in this appendix. The recording was taken from the thenar muscle.

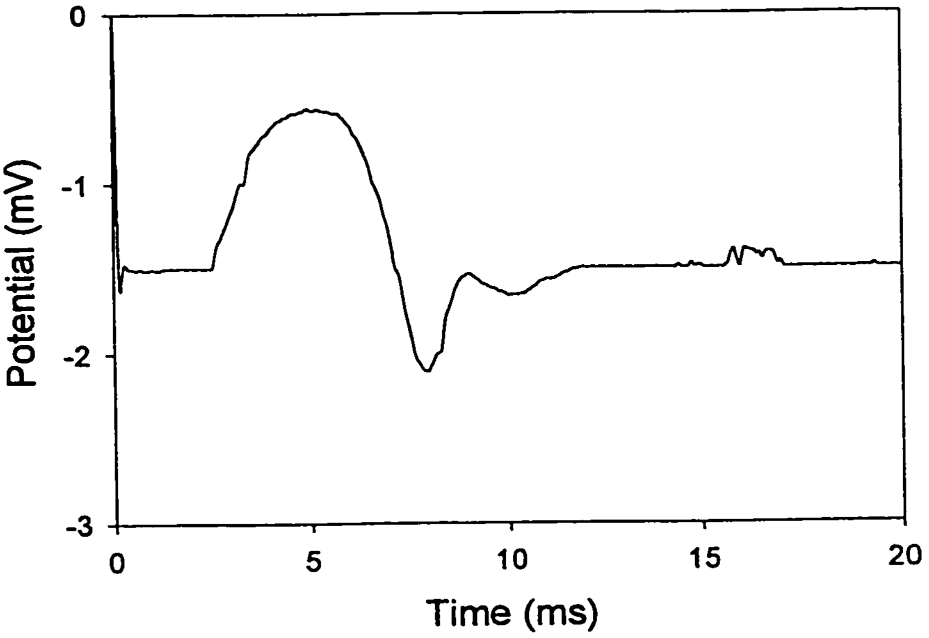

Figure B.6 Digitally sampled M-Wave plot. The M-Wave recording taken from the thenar muscle was elicited and sampled using the instrument described in this appendix. A stimulus pulse width of 200 μs and an amplitude of 20 mA was used.

B.5 Suggestions for Improvement and Future Modifications

One important aspect of the design that can be improved is the front end driver software. The DOS based driver software that was developed for this instrument is not suited to multitasking operating systems. Because the multitasking operating system must allocate system resources to several different applications that are running at the same time, a uniform sampling rate is not possible. The obvious solution to this problem is to redesign the A/D sampling hardware such that the hardware controls the sampling rate by way of an on board oscillator. This approach necessitates that the digitally converted sampled data be stored in on board memory. When the data sampling operation is completed, a front end software program can download the data through the PC parallel or serial port.

Appendix C: Least Squares Decomposition

To corroborate the estimates obtained for the average recruited nerve fiber diameter, a non-negative least squares algorithm was applied to digitally sampled M-wave responses elicited with the same stimulus current amplitude but different pulse widths.

The least squares decomposition technique was applied by first recording a representative motor unit action potential elicited by applying low level current pulses of approximately 20 mA and 100 μs to the median nerve by an electrode dipole placed on the medial side of the non dominant upper arm, proximal to the elbow. Recording an individual motor unit action potential was necessary to obtain a template that would be used in the subsequent least squares decomposition. The second step was to obtain a compound M-wave recording using stimulus current pulses within the range of 100 μs to 500 μs while maintaining a constant stimulus current pulse amplitude. A non-negative least squares algorithm implemented in MATLAB was used to obtain a decomposition of the recorded compound M-waves according to (C.1) where y_M is a vector consisting of the sampled compound M-wave points, $\boldsymbol{\Phi}$ is a matrix containing the scaled and time shifted motor unit action potential template data and $\boldsymbol{a}_{LS}$ is the coefficient vector. The columns of the $\boldsymbol{\Phi}$ matrix consists of the time shifted and scaled templates and the coefficient vector a_{LS} yields the number of each of these templates that must be superimposed to obtain an estimate of the motor unit action potential. The latency of each of these templates is related to the diameter of the associated motor nerve fiber as per equation (5.1). The coefficient vector a_{LS} yields the distribution or put simply, the number of each size of motor nerve fiber from which the responses must be superposed to reconstruct the compound M-Wave of y_M. An estimate of the average recruited nerve fiber diameter can be computed from the coefficient vector.

This decomposition technique was applied by Schoonhoven and colleagues to compound action potentials of peripheral nerves for the purpose of determining the number of active fibers contributing to the compound action potential and the distribution of their conduction velocities [81].

$$y_M = \Phi \cdot a_{LS} \tag{C.1}$$

To apply the least squares technique, the system of equations in (C.1) should be over determined. The non-negative least squares technique solves the over determined system of equations yielding a coefficient vector a_{LS}. As implied in the name of the algorithm, there is a constraint placed on the solutions that none of the components of the vector a_{LS} may be negative. The non-negative constraint arises from the fact that there is no physical interpretation for a negative quantity of fibers of a specific diameter contributing to the overall compound M-Wave.

A distribution of motor nerve fiber diameters was calculated for each recorded M-Wave at the different current pulse widths. From the distribution, estimates of the average recruited nerve fiber diameter were obtained and normalized as was done in the variable pulse width motor unit estimation study. The results for the single subject tested also exhibit the same marginal downward trend as has been consistently observed in the other variable pulse width experimental and simulation results.

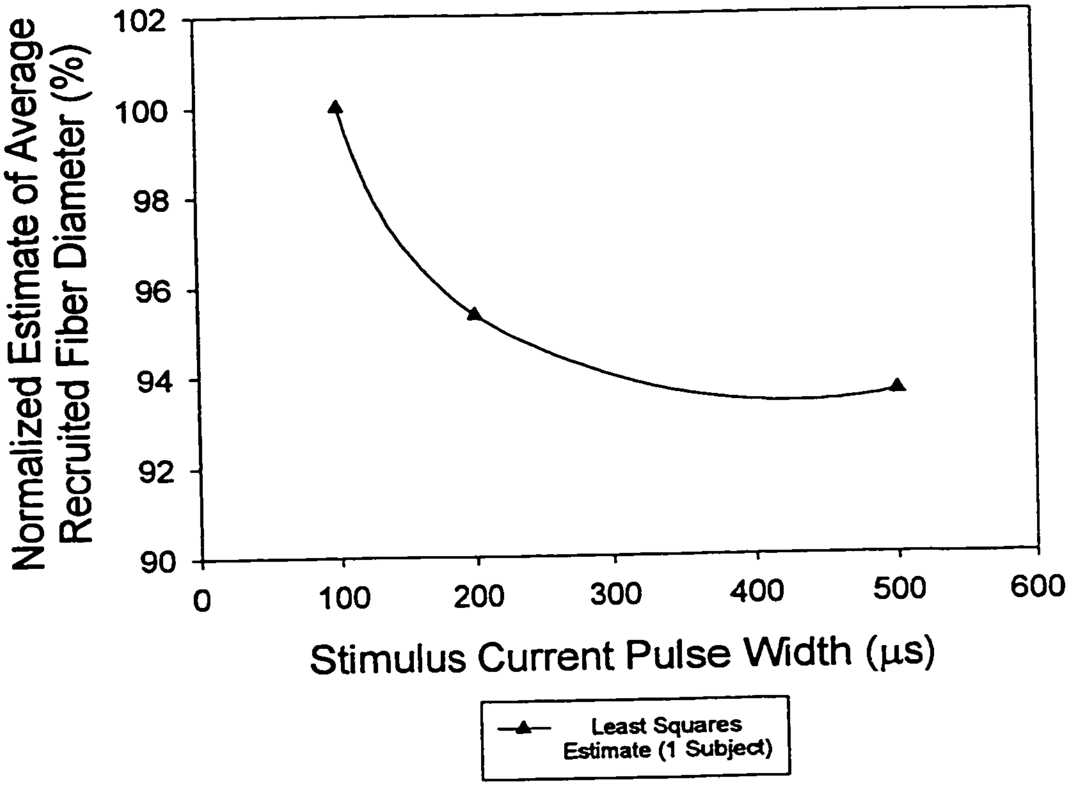

Figure C.1 Plot of the estimate of the average recruited nerve fiber diameter as a function of stimulus current pulse width based on the results of the non-negative least squares decomposition method applied to data taken from one subject.

References

[1] F.C. Want and P.J. Delwaide, Number and relative size of thenar motor units estimated by an adapted multiple point stimulation method *Muscle & Nerve*, vol. 18, pp. 969-979, 1995.

[2] W.M. Grill and J.T. Mortimer, Stimulus waveforms for selective neural stimulation *IEEE Engineering in Medicine and Biology*, vol. 14, Aug, 1995.

[3] F. Rattay. *Electrical Nerve Stimulation*, New York: Springer-Verlag Wien, 1990.

[4] A.L. Hodgkin and A.F. Huxley, A quantitative description of membrane current and its application to conduction and excitation in nerve *Journal of Physiology*, vol. 117, pp. 500-544, 1952.

[5] A.L. Hodgkin and A.F. Huxley, Currents carried by sodium and potassium ions through the membrane of the giant axon of loligo *Journal of Physiology*, vol. 116, pp. 449-472, 1952.

[6] A.L. Hodgkin and A.F. Huxley, The components of membrane conductance in the giant axon of loligo *Journal of Physiology*, vol. 116, pp. 473-496, 1952.

[7] A.L. Hodgkin and A.F. Huxley, The dual effect of membrane potential on sodium conductance in the giant axon of loligo *Journal of Physiology*, vol. 116, pp. 497-506, 1952.

[8] A.L. Hodgkin, A.F. Huxley, and B. Katz, Measurement of current-voltage relations in the membrane of the giant axon of loligo *Journal of Physiology*, vol. 116, pp. 424-448, 1952.

[9] L.A. Geddes and L.E. Baker, The specific resistance of biological material. A compendium of data for the biomedical engineer and physiologist *Med. & biol. Engng.*, vol. 5, pp. 271-293, 1967.

[10] R.V. Luepker, J.R. Michael, and J.R. Warbasse, Transthoracic electrical impedance: quantitative evaluation of a non-invasive measure of thoracic fluid volume *American Heart Journal*, vol. 85, pp. 83-93, Jan, 1973.

[11] A.F. Pacela, Impedance pneumography-a survey of instrumentation techniques *Med. & biol. Engng.*, vol. 4, pp. 1-15, 1966.

[12] M. Pomerantz, F. Delgado, and B. Eiseman, Clinical evaluation of transthoracic electrical impedance as a guide to intrathoracic fluid volumes *Annals of Surgery*, vol. 171, pp. 686-694, May, 1970.

[13] I.R. Berman, W.L. Scheetz, E.B. Jenkins, and H.V. Hufnagel, Transthoracic electrical impedance as a guide to intravascular overload *Archives of Surgery*, vol. 102, pp. 61-64, Jan, 1971.

[14] L.A. Geddes, H.E. Hoff, D.M. Hickman, M. Hinds, and L. Baker, Recording respiration and the electrocardiogram with common electrodes *Aerospace Medicine*, pp. 791-793, Jul, 1962.

[15] L.A. Geddes, H.E. Hoff, D.M. Hickman, and A.G. Moore, The impedance pneumograph *Aerospace Medicine*, pp. 28-33, Jan, 1962.

[16] J.H. Campbell, N.D. Harris, F. Zhang, B.H. Brown, and A.H. Morice, Clinical applications of electrical impedance tomography in the monitoring of changes in intrathoracic fluid volumes *Physiological Measurement*, vol. 15, pp. A217-A222, 1994.

[17] J.H. Campbell, N.D. Harris, F. Zhang, A.H. Morice, and B.H. Brown, Detection of changes in intrathoracic fluid in man using electrical impedance tomography *Clinical Science*, vol. 87, pp. 97-101, 1994.

[18] R. Guardo, C. Boulay, B. Murray, and M. Bertrand, An experimental study in electrical impedance tomography using backprojection reconstruction *IEEE Transactions on Biomedical Engineering*, vol. 38, pp. 617-627, Jul, 1991.

[19] L.A.W. Smulders and A.V. Van Oosterom, Application of electrical impedance tomography to the determination of lung volume *Clin. Phys. Physiol. Meas.*, vol. 13, pp. 167-170, 1992.

[20] J.C. Newell, D.G. Gisser, and D. Isaacson, An electric current tomograph *IEEE Transactions on Biomedical Engineering*, vol. 35, pp. 828-833, Oct, 1988.

[21] Q. Zhu, W.R.B. Lionheart, F.J. Lidgey, C.N. McLeod, K.S. Paulson, and M.K. Pidcock, An adaptive current tomograph using voltage sources *IEEE Transactions on Biomedical Engineering*, vol. 40, pp. 163-168, Feb, 1993.

[22] F.L.H. Gielen, W. Wallinga-de Jonge, and K.L. Boon, Electrical conductivity of skeletal muscle tissue: experimental results from different muscles in vivo *Medical and Biological Engineering and Computing*, vol. 22, pp. 569-577, 1984.

[23] R.B. Szlavik and H. de Bruin, Pulsed transient tissue conductivity measurement, 18th Annual Conference IEEE Engineering in Medicine and Biology Society, 1996.

[24] T. Janjic, S. Thomsen, and J.A. Pearce, Anisotropic electrical conductivity of tissue at RF frequencies, 18th Annual Conference IEEE Engineering in Medicine and Biology Society, 1996.

[25] P.W. Nicholson, The specific impedance of cerebral white matter *Experimental Neurology*, vol. 13, pp. 386-401, 1965.

[26] F.L.H. Gielen, H.E.P. Cruts, B.A. Albers, K.L. Boon, W. Wallinga-de Jonge, and H.B.K. Boom, Model of electrical conductivity of skeletal muscle based on tissue structure *Medical and Biological Engineering and Computing*, vol. 24, pp. 34-40, 1986.

[27] R.B. Szlavik and H. de Bruin, SPICE compatible equivalent circuit models of skeletal muscle tissue, 18th Annual Conference IEEE Engineering in Medicine and Biology Society, 1996.

[28] B. Coburn, Neural modeling in electrical stimulation *Critical Reviews in Biomedical Engineering*, vol. 17, pp. 133-178, 1989.

[29] C. Abzug, M. Maeda, B.W. Peterson and V.J. Wilson (Appendix by C.P. Bean), Cervical branching of lumbar vestibulospinal axons, *Journal of Physiology*, vol. 243, pp. 499-522, 1974.

[30] F. Rattay, Analysis of models for extracellular fiber stimulation *IEEE Transactions on Biomedical Engineering*, vol. 36, pp. 676-682, Jul, 1989.

[31] F. Rattay, Analysis of models for external stimulation of axons *IEEE Transactions on Biomedical Engineering* , vol. BME-33, pp. 974-977, Oct, 1986.

[32] F. Rattay, Modeling the excitation of fibers under surface electrodes *IEEE Transactions on Biomedical Engineering*, vol. 35, pp. 199-202, Mar, 1988.

[33] D.R. McNeal, Analysis of a model for excitation of myelinated nerve *IEEE Transactions on Biomedical Engineering*, vol. BME-23, pp. 329-337, Jul, 1976.

[34] B.J. Roth and K.W. Altman, Steady-state point-source stimulation of a nerve containing axons with an arbitrary distribution of diameters *Medical and Biological Engineering and Computing*, vol. 30, pp. 103-108, 1992.

[35] W.M. Grill and J.T. Mortimer, The effect of stimulus pulse duration on selectivity of neural stimulation *IEEE Transactions on Biomedical Engineering*, vol. 43, pp. 161-166, Feb, 1996.

[36] R. Schoonhoven and D.F. Stegeman, Models and analysis of compound nerve action potentials *Critical Reviews in Biomedical Engineering*, vol. 19, pp. 47-111, 1991.

[37] R.B. Szlavik and H. de Bruin, Simulating the distribution of axon size in nerves, 23rd Canadian Medical and Biological Engineering Society Conference, pp. 168-169, 1997.

[38] T.F. Weiss. *Cellular Biophysics Electrical Properties*, Cambridge: MIT Press, 1996.

[39] W.K. Purves, G.H. Orians, and H.C. Heller. *Life the Science of Biology*, Sunderland: Sinauer Associates Inc., 1995.

[40] E.R. Kandel and J.H. Schwartz. *Principles of Neural Science*, New York: Elsevier Science Publishing Co., 1985.

[41] E.N. Warman, W.M. Grill, and D. Durand, Modeling the effects of electric fields on nerve fibers: determination of excitation thresholds *IEEE Transactions on Biomedical Engineering*, vol. 39, pp. 1244-1254, Dec, 1992.

[42] G.G. Matthews. *Cellular Physiology of Nerve and Muscle*, Boston: Blackwell Scientific Publications, 1991.

[43] B. Katz. *Nerve, Muscle, and Synapse*, Toronto: McGraw-Hill, 1966.

[44] A.C. Guyton. *Textbook of Medical Physiology*, Toronto: W.B. Saunders Company, 1991.

[45] K.L. Moore. *Clinically Oriented Anatomy*, Baltimore: Williams & Wilkins Company, 1992.

[46] J.V. Basmajian. *Muscles Alive*, Baltimore: Williams & Wilkins Company, 1978.

[47] J.D. Sweeney, D.A. Ksienski, and J.T. Mortimer, A nerve cuff technique for selective excitation of peripheral nerve trunk regions *IEEE Transactions on Biomedical Engineering*, vol. 37, pp. 706-715, Jul, 1990.

[48] D.A. Teicher and D.R. McNeal, Comparison of a dynamic and steady-state model for determining nerve fiber threshold *IEEE Transactions on Biomedical Engineering*, vol. BME-25, pp. 105-107, Jan, 1978.

[49] P.H. Gorman and J.T. Mortimer, The effect of stimulus parameters on the recruitment characteristics of direct nerve stimulation *IEEE Transactions on Biomedical Engineering*, vol. BME-30, pp. 407-414, Jul, 1983.

[50] T.J. Doherty and W.F. Brown, The estimated numbers and relative sizes of thenar motor units as selected by multiple point stimulation in young and older adults *Muscle & Nerve*, vol. 16, pp. 355-366, Apr, 1993.

[51] P.H. Veltink, J.A. van Alste, and H.B.K. Boom, Influences of stimulation conditions on recruitment of myelinated nerve fibers: a model study *IEEE Transactions on Biomedical Engineering*, vol. 35, pp. 917-924, Nov, 1988.

[52] I.A. Boyd and M.R. Davey. *Composition of Peripheral Nerves*, Edinburgh: E & S Livingstone Ltd., 1968.

[53] M.C. Jeruchim, P. Balaban, and K.S. Shanmugan. *Simulation of Communication Systems*, New York: Plenum Press, 1994.

[54] J.D. Kraus. *Electromagnetics* , Toronto: McGraw-Hill, 1984.

[55] A. Heringa, D.F. Stegeman, G.J.H. Uijen, and J.P.C. Weerd, Solution methods of electrical field problems in physiology *IEEE Transactions on Biomedical Engineering*, vol. BME-29, pp. 34-42, Jan, 1982.

[56] W.F. Ames. *Numerical Methods for Partial Differential Equations*, Toronto: Academic Press Inc., 1992.

[57] P.H. Veltink, B.K. Van Veen, J.J. Struijk, J. Holsheimer, and H.B.K. Boom, A modeling study of nerve fascicle stimulation *IEEE Transactions on Biomedical Engineering*, vol. 36, pp. 683-692, Jul, 1989.

[58] V. Galea, H. de Bruin, R. Cavasin, and A.J. McComas, The numbers and relative sizes of motor units estimated by computer *Muscle & Nerve*, vol. 14, pp. 1123-1130, 1991.

[59] R.B. Stein and J.F. Yang, Methods for estimating the number of motor units in human muscle *Annals of Neurology*, vol. 28, pp. 487-495, 1990.

[60] P.N. Robillard and D. Poussart, Spatial resolution of four electrode array *IEEE Transactions on Biomedical Engineering*, vol. BME-26, pp. 465-470, Aug, 1979.

[61] P.W. Nicholson, Experimental models for current conduction in an anisotropic medium *IEEE Transactions on Biomedical Engineering*, vol. BME-14, pp. 55-56, Jan, 1967.

[62] S. Rush, J.A. Abildskov, and R. McFee, Resistivity of body tissues at low frequencies *Circulation Research*, vol. 12, pp. 40-50, Jan, 1963.

[63] S. Rush, Methods of measuring the resistivities of anisotropic conducting media in situ *Journal of Research of the National Bureau of Standards - C, Engineering and Instrumentation*, vol. 66C, pp. 217-222, Jul, 1962.

[64] R. Plonsey, The active fiber in a volume conductor *IEEE Transactions on Biomedical Engineering*, vol. BME-21, pp. 371-381, Sep, 1974.

[65] K.W. Altman and R. Plonsey, Point source nerve bundle stimulation: effects of fiber diameter and depth on simulated excitation *IEEE Transactions on Biomedical Engineering*, vol. 37, pp. 688-698, Jul, 1990.

[66] P.H. Veltink, J.A. van Alste, and H.B.K. Boom, Simulation of intrafascicular and extraneural nerve stimulation *IEEE Transactions on Biomedical Engineering*, vol. 35, pp. 69-75, Jan, 1988.

[67] J.J. Struijk, J. Holsheimer, and H.B.K. Boom, Excitation of dorsal root fibers in spinal cord stimulation: a theoretical study *IEEE Transactions on Biomedical Engineering*, vol. 40, pp. 632-639, Jul, 1993.

[68] A.S. Sedra and K.C. Smith. *Microelectronic Circuits*, Toronto: Holt, Rinehart and Winston, 1987.

[69] J.K. Fidler and C. Nightingale. *Computer Aided Circuit Design*, Don Mills: Nelson, 1978.

[70] K.W. Altman and R. Plonsey, Analysis of excitable cell activation: relative effects of external electrical stimuli *Medical and Biological Engineering and Computing*, vol. 28, pp. 574-580, 1990.

[71] J.W. Clark and R. Plonsey, Fiber interaction in a nerve trunk *Biophys. J.*, vol. 11, pp. 281-294, 1971.

[72] B.J. Roth, Mechanisms for electrical stimulation of excitable tissue *Critical Reviews in Biomedical Engineering*, vol. 22(3/4), pp. 253-305, 1994.

[73] R.B. Szlavik and H. de Bruin, The effect of stimulus current pulse width on nerve fiber size recruitment patterns, Accepted for publication in the *Medical Engineering and Physics Journal*.

[74] D.F. Stegeman, J.P.C. de Weerd, and E.G.J. Eijkman, A volume conductor study of compound action potentials of nerves in situ: The forward problem *Biological Cybernetics*, vol. 33, pp. 97-111, 1979.

[75] C.J. Stok and P.M. Wognum, A noniterative approximate solution method for volume conductor problems based on the finite difference method *IEEE Transactions on Biomedical Engineering*, vol. 35, pp. 31-35, Jan, 1988.

[76] H.I. Saleheen and K.T. Ng, A new three-dimensional finite-difference bidomain formulation for inhomogeneous anisotropic cardiac tissues *IEEE Transactions on Biomedical Engineering*, vol. 45, pp. 15-25, Jan, 1998.

[77] A.J. Surowiec, S.S. Stuchly, J.R. Barr, and A. Swarup, Dielectric properties of breast carcinoma and the surrounding tissues *IEEE Transactions on Biomedical Engineering*, vol. 35, pp. 257-263, Apr, 1988.

[78] G.N. Reddy and S. Saha, Electrical and dielectric properties of wet bone as a function of frequency *IEEE Transactions on Biomedical Engineering*, vol. BME-31, pp. 296-303, Mar, 1984.

[79] R. Plonsey. *Bioelectric Phenomena*, Toronto: McGraw-Hill, 1969.

[80] T. Teorell, Application of square wave analysis to bioelectric studies *Acta Physiol. Scand.*, vol. 12, pp. 235-254, 1947.

[81] R. Schoonhoven, D.F. Stegeman, A. Van Oosterom, and G.F.M. Dautzenberg, The inverse problem in electroneurography-I: conceptual basis and mathematical formulation *IEEE Transactions on Biomedical Engineering*, vol. 35, pp. 769-777, Oct, 1988.